Department of Physics and Astronomy
University of Heidelberg

2018

Bachelor Thesis in Physics
submitted by

ALISSA FINK

born in MONACO (Monaco)

Mass difference between matter and anti-matter

This Bachelor Thesis has been carried out by ALISSA FINK at the
Physics Institute in Heidelberg
and GSI Darmstadt
under the supervision of
Prof. Dr. Silvia Masciocchi and Dr. Alberto Caliva

Abstract

The CPT theorem states that every physical process is symmetric under the simultaneous transformation of Charge, Parity and Time. It is one of nature's most fundamental symmetries and implies that a particle and its antiparticle must have equal mass. Thus, a difference between the mass of matter and anti-matter is a direct proof of CPT symmetry violation, which has never been observed. This thesis represents a test on the CPT theorem in the case of complex particles and anti-particles systems bound by the strong force inside a nucleus. It is performed with the ALICE detector at the LHC with (anti-)nuclei samples produced in Pb–Pb collisions at center-of-mass energy per nucleon pair $\sqrt{s_{NN}} = 5.02\,\text{TeV}$ and evaluates the mass-to-charge ratio difference between the deuteron and anti-deuteron, ^{3}He and $^3\overline{\text{He}}$ nuclei. The (anti-)nuclei candidates are selected with the ALICE Time Projection Chamber and their mass-to-charge ratio is determined via extraction with the Time Of Flight detector signal. The final results $\Delta(m/|z|)_{\text{d}\,\overline{\text{d}}} = -2.2 \times 10^{-4} \pm 1.1 \times 10^{-4}$ GeV/c^2 and $\Delta(m/|z|)_{^3\text{He}\,^3\overline{\text{He}}} = -2.0 \times 10^{-3} \pm 1.5 \times 10^{-3}$ GeV/c^2 are presented for the first time for this data set and are part of the most precise measurements of mass differences in the sector of nuclei physics.

Zusammenfassung

Das CPT Theorem besagt, dass jeder physikalische Prozess unter gleichzeitiger Transformation von Ladung (Charge), Parität (Parity) und Zeit (Time) symmetrisch ist. Dies ist eine der fundamentalistischsten Symmetrien der Natur und impliziert, dass ein Teilchen und sein entsprechendes Anti-Teilchen die gleiche Masse haben müssen. Somit ist eine Differenz zwischen der Masse von Materie und Anti-Materie ein direkter Beweis für die Verletzung von CPT Symmetrie, die bisher noch nicht beobachtet wurde. Diese Arbeit prüft das CPT Theorem im Fall von komplexen Teilchen- und Anti-Teilchen-Systemen, die mit der starken Kraft innerhalb des Nucleus gebunden sind. Sie wird mit dem ALICE Detektor am LHC mit (Anti-)Kerne-Proben, die in Pb–Pb Kollisionen mit einer Schwerpunktsenergie pro Nucleon-Paar von $\sqrt{s_{NN}} = 5.02\,\text{TeV}$ produziert werden, durchgeführt und evaluiert die Differenz im Verhältnis Masse-zu-Ladung zwischen Deuteron und Anti-Deuteron, ^{3}He and $^3\overline{\text{He}}$ Kerne. Die Endergebnisse von $\Delta(m/|z|)_{\text{d}\,\overline{\text{d}}} = -2.2 \times 10^{-4} \pm 1.1 \times 10^{-4}$ GeV/c^2 und $\Delta(m/|z|)_{^3\text{He}\,^3\overline{\text{He}}} = -2.0 \times 10^{-3} \pm 1.5 \times 10^{-4}$ GeV/c^2 werden zum ersten Mal für diesen Datensatz präsentiert und sind Teil der genauesten Messungen von Massendifferenzen im Bereich der Kernphysik.

Contents

1 Introduction **6**
- 1.1 Matter and anti-matter . . . 6
- 1.2 The CPT theorem . . . 6
- 1.3 The strong interaction . . . 7
- 1.4 Physics of the quark-gluon plasma . . . 9
  - 1.4.1 Heavy ion collisions . . . 9
  - 1.4.2 Space and time evolution of a heavy-ion collision . . . 10
  - 1.4.3 Production of light nuclei in high-energy hadronic collisions . . . 11
- 1.5 From heavy-ion collisions to the early universe . . . 12

2 Experimental apparatus and analysis framework **13**
- 2.1 CERN and the LHC . . . 13
- 2.2 The ALICE detector . . . 14
  - 2.2.1 The Inner Tracking System . . . 15
  - 2.2.2 The Time Projection Chamber . . . 15
  - 2.2.3 The Time Of Flight detector . . . 17
- 2.3 The analysis software . . . 18

3 Data analysis **19**
- 3.1 Event and track selection . . . 19
- 3.2 Particle identification . . . 20
- 3.3 Rejection of secondary nuclei . . . 21
- 3.4 Calculation of m^2/z^2 with the time of flight . . . 23
- 3.5 Extraction of m^2/z^2 with the TOF signal . . . 24
  - 3.5.1 (Anti-)Deuteron TOF signal analysis . . . 25
  - 3.5.2 (Anti-)Helium-3 TOF signal analysis . . . 26
  - 3.5.3 Width of the TOF signal for nuclei and anti-nuclei . . . 28

4 Results **30**
- 4.1 Mass difference between matter and anti-matter . . . 30
  - 4.1.1 d–$\overline{\text{d}}$ mass difference . . . 30
  - 4.1.2 ^{3}He–$^3\overline{\text{He}}$ mass difference . . . 35
- 4.2 Anti-nuclei to nuclei yield ratios . . . 37
  - 4.2.1 $\overline{\text{d}}$–d yield ratio . . . 37
  - 4.2.2 $^3\overline{\text{He}}$–^{3}He yield ratio . . . 39
- 4.3 Comparison with previous measurements . . . 41

5 Conclusion **44**

A (Anti-)Deuteron plots **47**
A.1 Deuteron fits 47
A.2 Anti-Deuteron fits 57

B (Anti-)Helium-3 plots **67**
B.1 Helium-3 fits 67
B.2 Anti-Helium-3 fits 69

Chapter 1

Introduction

1.1 Matter and anti-matter

The Universe, as complex as it may seem, is composed of only a handful of elementary particles interacting with each other, illustrated on Fig 1.1. They are described, alongside their interactions, by a theory called the Standard Model (SM), which successfully explains a lot of physical phenomena. These elementary particles are either *matter particles* or *field mediators*, called gauge bosons, responsible for the interactions between them. There are three types of relevant fundamental interactions in particle physics: the electromagnetic interaction, the weak and the strong interaction. They are described by relativistic quantum field theories which are implemented in the Standard Model. Matter particles are ordered in two groups: quarks and leptons, both are divided in three subgroups of two and have corresponding anti-particles, which constitute *anti-matter*.

After the Big Bang, in the early stages of the Universe, it is considered that quarks and gluons, which constitute strongly interacting (anti-)matter, were able to move freely in what is called the *Quark-Gluon Plasma* (QGP), and that matter and anti-matter were created in a perfectly equal amount after being in this particular state. There is, however, a larger amount of matter around us; this implies that at some point, anti-matter must have suddenly "disappeared". This strange phenomenon made it possible for the Universe to even exist, instead of vanishing into energy because of matter anti-matter annihilation. Studying the physics of the QGP allows one to investigate why and how this could have occurred and to understand the most fundamental process of the Universe: the creation of matter.

1.2 The CPT theorem

The CPT theorem states that every physical process is symmetric under the simultaneous transformation of Charge, Parity and Time. In other words, a universe in which time is reversed, space is mirrored and each particle is replaced by its anti-particle would still obey to the same physics because of this symmetry. P [2], CP [3] and T [4] symmetry violation have already been experimentally observed, but never has CPT symmetry violation.

Equality of mass, absolute value of the charge, lifetime and magnetic moment between a particle and its antiparticle is a prediction of CPT invariance [5]. Thus, there is a tight link between

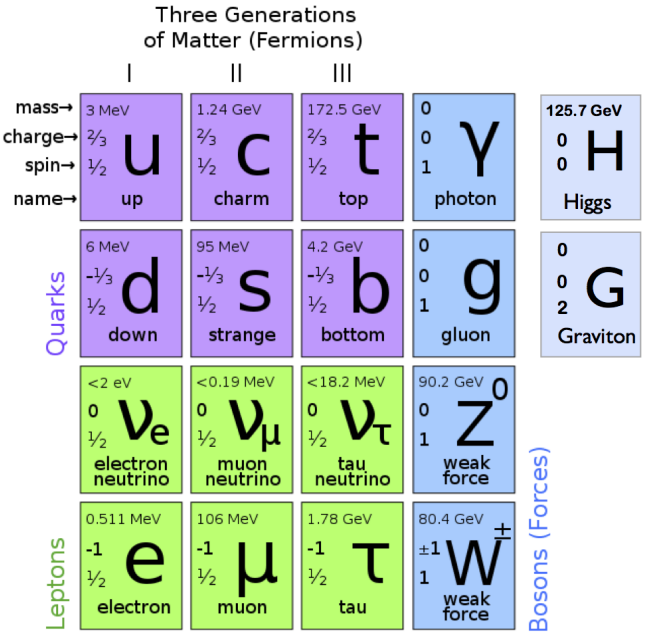

Figure 1.1: The elementary particles of the Standard Model of particle physics [1] ordered into quarks, leptons and bosons.

this theorem and the creation of (anti-)matter, and one can probe CPT symmetry by looking at the mass of a particle and its corresponding anti-particle. The purpose of this thesis is to measure the mass difference between matter and antimatter to test the validity of the CPT invariance in the case of composite particles bound by the strong force inside a nucleus: the deuteron (d) and anti-deuteron ($\overline{\mathrm{d}}$), and the ^{3}He and $^3\overline{\mathrm{He}}$.

This chapter contains a short summary of the theory of strong interaction, a description of heavy-ion collisions, an overview of the space and time evolution of the QGP as well as a discussion about particle production in the QGP. Ch. 2 introduces the analysis framework with a depiction of the experimental apparatus, its detectors and the analysis software used for this thesis. Ch. 3 describes in detail the analysis strategy and the results are presented in Ch. 4. Ch. 5 contains a summary of the results and an outlook on the future.

1.3 The strong interaction

A nucleus is composed of protons and neutrons, also called nucleons. They are made of quarks, bound together by the strong force, which is described by *Quantum ChromoDynamics* (QCD). QCD has two main properties. The first one is that intermediate bosons of the strong interaction, gluons, have an additional quantum number: color. All particles bound by the strong force must be in a color neutral state. The second property of the strong interaction is that its coupling constant α_s is dependent on the momentum transfer (see Fig. 1.2) in the interaction between two quarks and is given by [6]:

$$\alpha_s(|q^2|) = \frac{12\pi}{(11n_c - 2f)(\ln|q^2|\lambda_{\mathrm{QCD}})}\,, \tag{1.1}$$

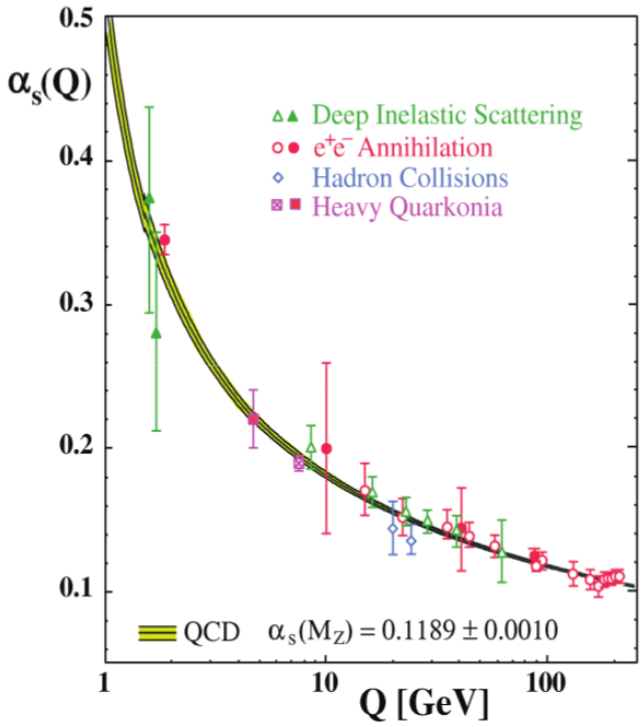

Figure 1.2: Strong coupling constant as a function of the momentum transfer [7].

where n_c is the number of quark colors, f the number of quark flavors and λ_{QCD} is the scale parameter of the theory with an approximative value of 200 MeV. Since $11n_c$ is larger than $2f$, α_s is small for high momentum transfer and large for low momentum transfer. One deduces from it that quarks move more freely at large momentum transfers, this is defined as *asymptotic freedom*.

The interaction between two quarks is expressed by the effective potential [6]:

$$V(r) = -\frac{\alpha_s}{r} + k \cdot r \,. \tag{1.2}$$

Thus, at short distances ($r \ll 1\,\text{fm}$), this potential is similar to the Coulomb potential. At larger distances, the second term of the equation becomes dominant and increases linearly with the scaling factor $k \approx 1\,\text{GeV/fm}$.

Due to this peculiar potential, one needs about 1 GeV to "pull" two quarks 1 fm apart from each other. As a result, free quarks cannot be observed directly, they are *confined* inside the hadron and one can only measure them in a bound state. When pulling apart a quark away from its partner, their potential increases until the energy is sufficient for a quark–antiquark pair to be produced. It leads to the creation of a hadron, a particle made of quarks. This mechanism is called *fragmentation* and pictured on Fig. 1.3 below.

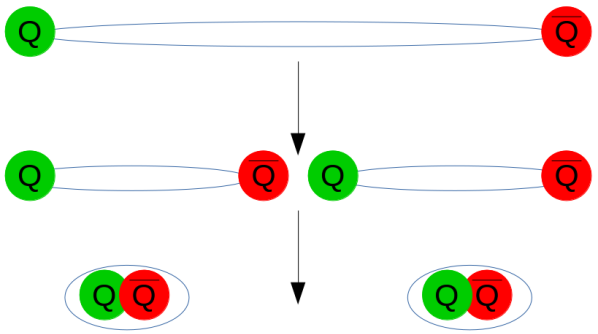

Figure 1.3: Illustration of hadron formation by fragmentation. The picture must be read from top to bottom.

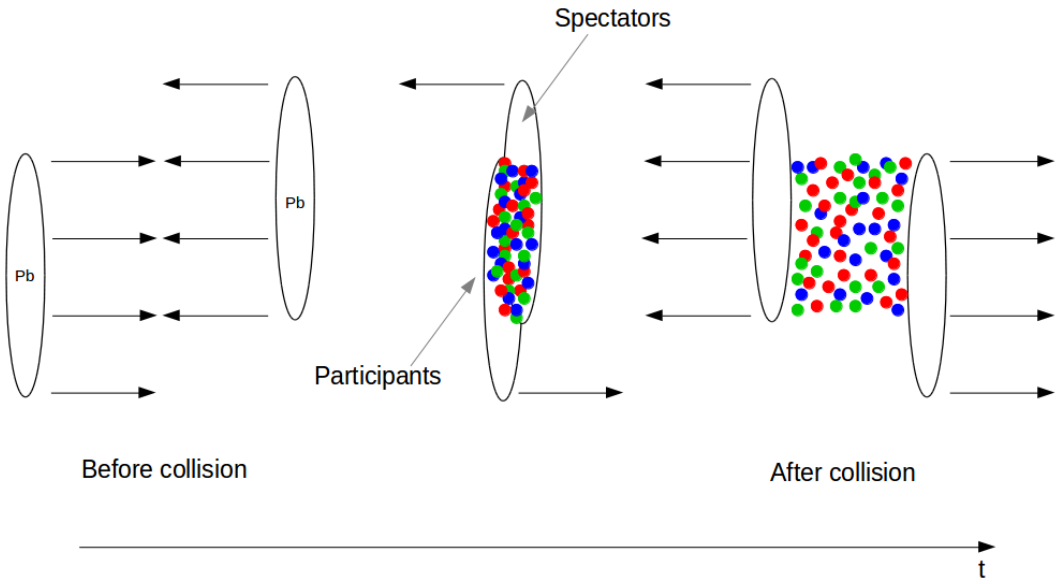

Figure 1.4: A single collision between two lead ions. One can see the participants and spectators of the event, the participants interact with each other in a very hot and dense environment.

1.4 Physics of the quark-gluon plasma

1.4.1 Heavy ion collisions

Lavish sources of matter and anti-matter are heavy-ion collisions at extreme energies. At the CERN Large Hadron Collider (LHC), Pb–Pb collisions happen at a center-of-mass energy per nucleon pair $\sqrt{s_{NN}}$ of 5.02 TeV. At this energy scale, Lorentz contracted heavy ions "traverse" each other, resulting in a very hot and dense environment. Unlike proton–proton collision experiments, the interaction zone is not point-like. In fact, not all nucleons interact with each other, some are participants of the collision, others are just spectators. The collective expansion of the system depends on the collision's amount of participants, it is spherically symmetric in case of total overlay. In case of partial overlay, an asymmetric flow also directs the collective expansion. The overall geometry of the overlap region depends on a a variable called impact parameter b, which represents the distance between the two centers of the colliding nuclei. If $b = 0$ the collision is called central, otherwise it is called semi-central (or peripheral). An illustration of a Pb–Pb collision can be found on Fig. 1.4.

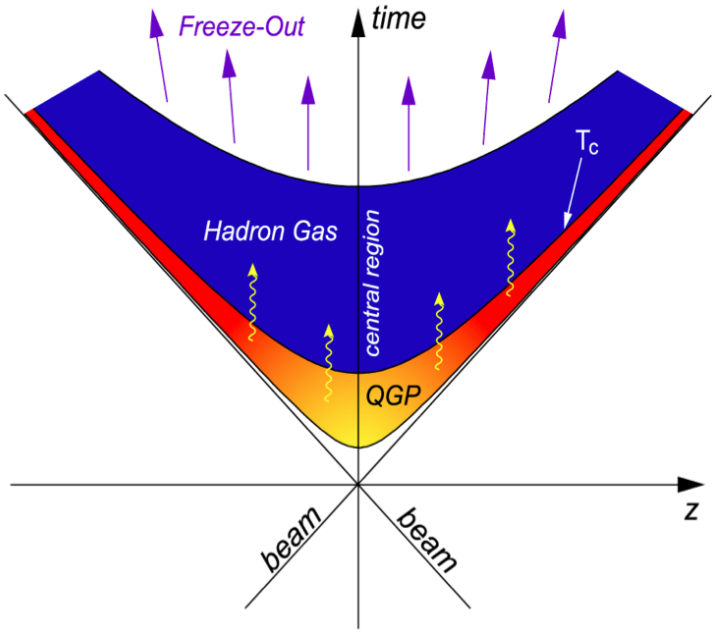

Figure 1.5: Space time diagram of the evolution of matter in a heavy-ion collision [8].

1.4.2 Space and time evolution of a heavy-ion collision

The object produced in a heavy-ion collision is a fireball which expands and goes through different stages (see Fig. 1.5), described below [7].

1. Pre-equilibrium stage: the fireball is in a highly excited state, the frequent collisions of the constituent of the system lead to thermalisation, an establishment of a local equilibrium.

2. Expansion stage: the fireball expands and cools down according to hydrodynamical laws.

3. Hadronization: below a critical energy density of $\epsilon_{\mathrm{cr}} \approx 1\,\mathrm{GeV/fm^3}$ or critical temperature of $T_{\mathrm{cr}} \approx 200\,\mathrm{MeV}$, the quarks and gluons hadronize gradually, leading to a mixed phase of QGP and hadronic gas. The hadrons collide and maintain a local thermal equilibrium.

4. Freeze-out: inelastic collisions, responsible for the creation of hadrons, cease and particle species are therefore fixed. This is chemical freeze-out. At some point, the gas has expanded so much that the distance between the constituents is too large for them to interact elastically. This is kinetic freeze-out, the particles cannot "see" each other, they therefore don't interact anymore and move in the direction of the detectors.

The phase diagram of hadronic matter is depicted on Fig. 1.6 and described with two variables: the temperature T and baryochemical potential μ_b, linked to the baryon density of the system. One can see that a QGP state is achieved by either having a very dense or a very hot environment. In the case of heavy-ion collisions, a very hot environment is created. Many studies have been conducted in order to define precisely the temperature at which hadronic matter transitions, it has been found that it is $156(4)\,\mathrm{MeV}$ [9].

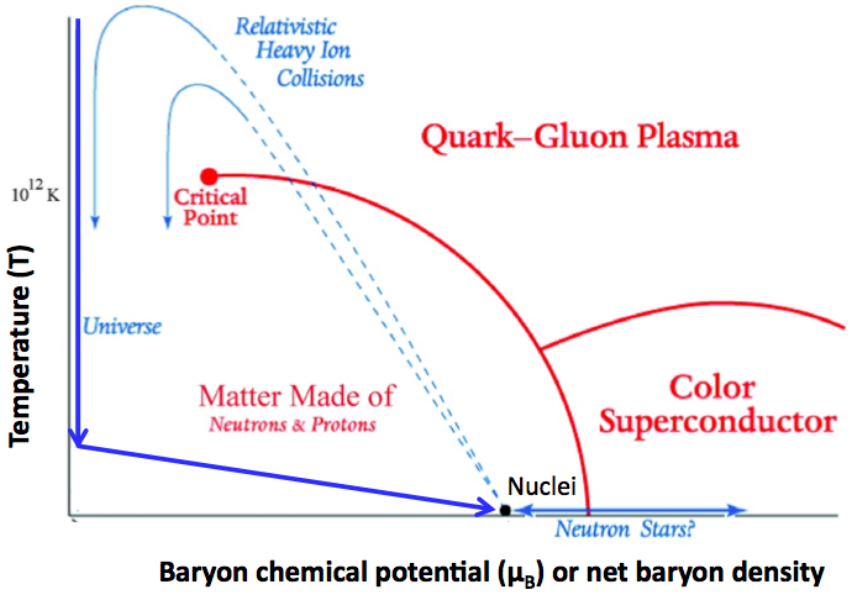

Figure 1.6: QCD phase diagram of strongly interacting matter [8].

1.4.3 Production of light nuclei in high-energy hadronic collisions

For scattering processes with large momentum transfer (way above 1 GeV), perturbative QCD is applicable since α_s is small enough to make a series expansion. This is not the case anymore for processes in which hadronization is involved, at the scale of 1 GeV or below, since the increase in contributions from higher order Feynman diagrams cannot be neglected. For this reason, hadronization is not describable by QCD first principles and one has to rely on phenomenological models.

One of them is the statistical hadronization model, which describes effectively multiplicities of many particle species, including the $(\overline{\mathrm{d}})\mathrm{d}$ and $(^3\overline{\mathrm{He}})^3\mathrm{He}$, in high energy collisions [10,11]. It postulates that hadrons are formed instantaneously and that particle abundances are fixed at chemical freeze-out at a certain temperature that has been estimated to be around 160 MeV. Nonetheless, the statistical hadronization model has not yet explained some problematic implications: a particle with a biding energy of a few MeV should not be able to survive at freeze-out temperatures of ~ 160 MeV.

Another model describing hadron production is the coalescence model. It presupposes that protons and neutrons are produced individually in the QGP and that they bind into clusters after freeze-out. The cluster formation probability is characterized with the help of the invariant coalescence factor B_A, defined through a relation between the cluster momentum spectra and the spectrum of the coalescing protons (p) and neutrons (n) [12]:

$$E_A = \frac{\mathrm{d}N_A}{\mathrm{d}^3P_A} B_A \left(E_p \frac{\mathrm{d}N_p}{\mathrm{d}^3P_p} \right)^Z \left(E_n \frac{\mathrm{d}N_n}{\mathrm{d}^3P_n} \right)^N . \tag{1.3}$$

The coalescence model, however,raises the question of energy conservation. Some processes, like the formation of a deuteron after the coalescing of a proton and a neutron, are forbidden in regards of energy conservation. An explanation for that would be that particles in the QGP are produced off shell.

1.5 From heavy-ion collisions to the early universe

There are some strong assumptions that the Universe must have been in a QGP state in its early history and transitioned at some point to hadronic matter. This transition from quarks and gluons to hadrons, and more importantly here to nuclei –as explained in Sec. 1.4.3, still has some intriguing aspects. Studying heavy-ion collisions is a way to investigate them and to go back in time to explore the early stages of the Universe and understand how (anti-)matter was initially formed. But also test if fundamental laws of physics, like the CPT theorem discussed in Sec. 1.2, are still conclusive in such an extreme environment. To shed light on this, this thesis probes the CPT theorem on the lightest nuclei and anti-nuclei produced in heavy-ion collisions.

Chapter 2

Experimental apparatus and analysis framework

2.1 CERN and the LHC

At the European Organization for Nuclear Research, or CERN, physicists investigate the fundamental processes and particles of the Universe by studying collisions of protons or Pb ions accelerated by the Large Hadron Collider (LHC).

The LHC (Fig. 2.1) is the world's largest particle accelerator and is capable of accelerating particles at velocities approaching the speed of light. It is a ring with a circumference of 27 km, in which high energy particle beams, curved by a strong magnetic field created by superconducting magnets, travel in opposite directions. The electromagnets are operated at a temperature of a few Kelvin in order to maintain the superconducting state of the magnets [13].

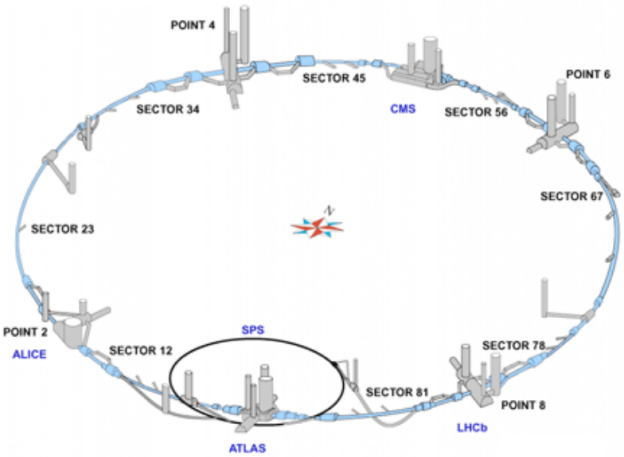

Figure 2.1: The LHC ring with the four main experiments of CERN: ALICE, ATLAS, CMS and LHCb located at the four points of collision [13].

2.2 The ALICE detector

The data used for this analysis was taken in 2015 by the ALICE (A Large Ion Collider Experiment) detector [14], one of the four main detectors of the LHC. ALICE is composed of 18 detector systems –all shown on Fig. 2.2– and designed to register heavy ion collision events, its overall dimensions are $16 \times 16 \times 16$ m^3 and its weight is of $\sim 10\,000$ t. It is optimized for the study of strongly interacting matter: it is able to cope with high particle densities and can register particles with very low momentum, produced numerously in heavy ion collisions. The data used for this analysis was taken with three different detectors: the ITS (Inner Tracking System), the TPC (Time Projection Chamber) and the TOF (Time Of Flight) detector, all described thoroughly in Sec. 2.2.1, 2.2.2 and 2.2.2.

The ITS, TPC and TOF are located in the central barrel and embedded in a solenoid with a magnetic field up to 0.5 T. Like the other detectors from the central barrel –the Transition Radiation Detector (TRD), the Photon Spectrometer (PHOS), the Electromagnetic Calorimeter (EMCal) and the High Momentum Particle Identification Detector (HMPID)– they are designed for particle tracking and identification. The Photon Multiplicity Detector (PMD) and the Forward Multiplicity Detector (FMD) are used for the identification of photons and the measurement of charged particles in the pseudorapidity region of $|\eta| \sim 3$. The plastic scintillator T0 measures the time and longitudinal position of the collision. The V0 detctor estimates the centrality of an event as well as the Zero Degree Calorimeter (ZDC). The ZDC is split in two calorimeters that count the number of spectator nucleons of the collision, they are placed symmetrically on both sides of the interaction point. Finally, for the measurement of muons, there is the dedicated MUON spectrometer located in the outer part of the apparatus [15]. The complete description of the ALICE detectors can be found in [14].

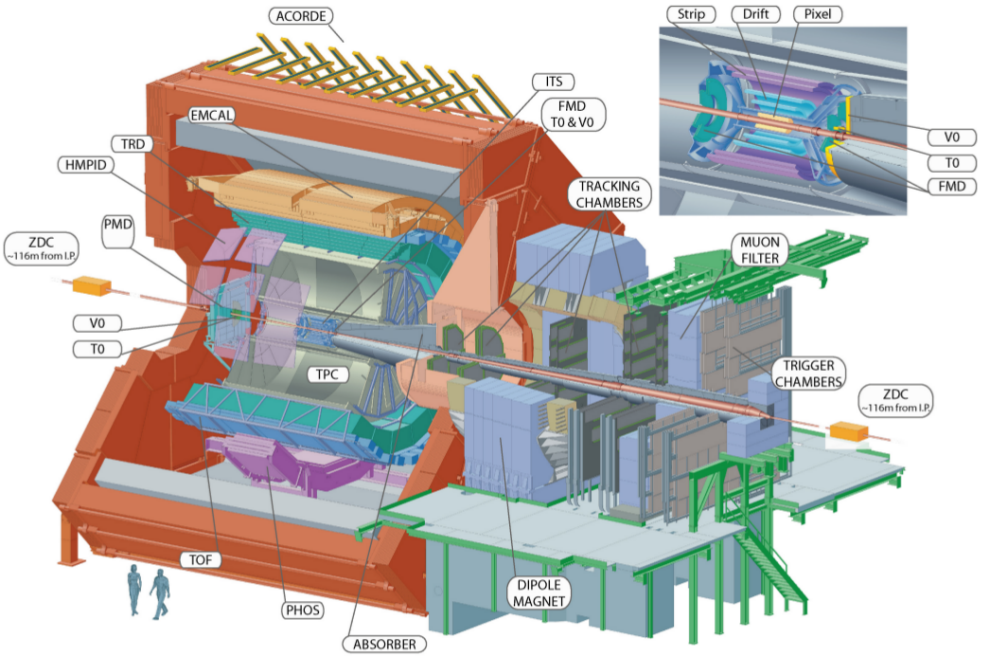

Figure 2.2: The ALICE apparatus [14].

2.2.1 The Inner Tracking System

The ITS is a six layer detector located in the most central area of the ALICE detector at radii between 4 and 43 cm. It consists of two Silicon Pixel Detectors (the SPD), two Silicon Drift Detectors (SDD) and two Silicon Strip Detectors (SSD). The SPD is used for triggering, tracking and vertex reconstruction. The SDD and SSD are used for tracking and provide a measurement of the ionization energy loss of particles, usable for Particle IDentification (PID). It is capable of localizing the primary vertex with a resolution better than 100 µm and is also used as a standalone tracker to reconstruct tracks from particles that do not have a momentum sufficiently large to reach the TPC. The detector elements are optimized in order to achieve a radiation length of 1.1% X_0 per layer. The current read-out rate capability of the ITS is, independently of the detector's occupancy, of 1 kHz [14].

2.2.2 The Time Projection Chamber

The TPC is the main tracking detector of ALICE. It is a cylindrical gas detector filled with 90 m^3 of $ArCO_2$ and divided into two parts by a central cathode, kept at −100 kV. Its azimuthal acceptance covers a 2π angle and its pseudo-rapidity interval is of $|\eta| < 0.9$. The TPC copes with tremendous particle multiplicities ideal for the reconstruction of Pb–Pb collision events.

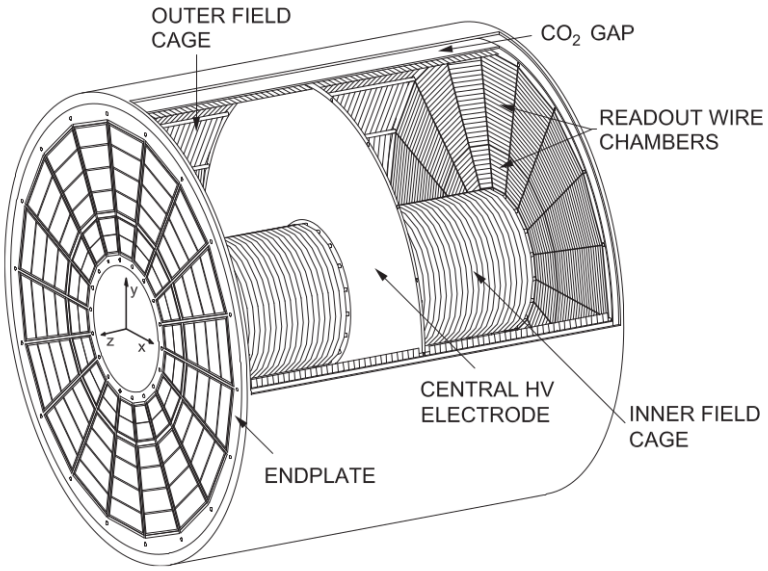

Figure 2.3: 3D plot of the ALICE TPC. The endplates are each composed of 18 sectors and 36 readout chambers [16].

When a collision occurs, the charged particles originating from the interaction point traverse the detector and ionize the gas of the TPC along their trajectory. The ionization electrons drift (maximal drift time ∼ 90 µs), under the influence of the electric field, to the endplates of the cylinder where they are read out. These end plates are equipped with multiwire proportional chambers (MWPC) with a cathode pad readout. The z-coordinate of a particle's position in the detector at a fixed time is given by its drift time, the x-coordinate by charge sharing among cathode pads and the y-coordinate by the wire and pad row number. By "linking" all the points

of the particle's track together, one obtains its full track in the TPC. This principle is depicted on Fig. 2.4

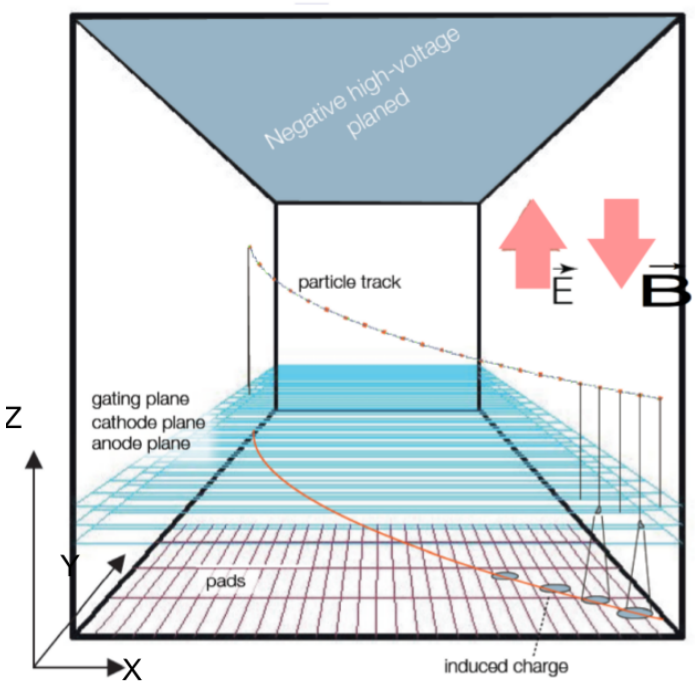

Figure 2.4: Illustration of the principle of the TPC, the z axis indicates the beam direction. The gating plane hinders the back-flow of ions created in the amplification region into the detector [17].

The TPC is capable of effectuating particle identification over a very wide momentum range and is performed by simultaneously measuring the ionization energy loss $\mathrm{d}E/\,\mathrm{d}x$ and momentum of each particle traversing the gas via its curvature radius in the magnetic field. In fact, when a particle traverses a magnetic field B, it undergoes the Lorentz force F_L given by: $F_L = q(E+v\times B)$, where $q :=$ charge, $E :=$ electric field, $v :=$ velocity. This force is responsible for the helix form of the particle's track in the detector. If we consider the case of the ALICE experiment with $E = 0$, $B = (0, 0, B_z)$. This yields:

$$F_T = qB_z v_T \tag{2.1}$$

$$\Rightarrow \frac{p_T}{q} = \frac{1}{k} B_z \text{ with } R = \frac{1}{k},\ k := \text{curvature}\,. \tag{2.2}$$

Thus, one can deduce the *transverse rigidity* p_T/z (transverse momentum divided by charge) of a particle with the curvature of the particle's trajectory.

The mean energy loss of a charged particle traversing matter follows the Bethe-Bloch formula, described with the following equation [6]:

$$\left\langle -\frac{\mathrm{d}E}{\mathrm{d}x} \right\rangle = Kz^2 \frac{Z}{A} \frac{1}{\beta^2} \left[\frac{1}{2} \ln \frac{2m_e c^2 \beta^2 \gamma^2 W_{\max}}{I^2} - \beta^2 - \frac{\delta(\beta\gamma)}{2} \right] . \tag{2.3}$$

With $K = 4\pi N_A r_e^2 m_e c^2$ (N_A is Avogadro's number, r_e is the electron radius and m_e its mass), $z :=$ charge number of incident particle, $Z :=$ atomic number of absorber, $A :=$ atomic mass of absorber, $W :=$ energy transfer to an electron in a single collision and $I :=$ mean excitation

energy. β is the particle's velocity over the speed of light with $\beta = \frac{v}{c}$ and $\delta(\beta\gamma)$ is a density effect correction to the ionization energy loss.

The Bethe-Bloch formula can be parametrized by [15]:

$$f(\beta\gamma) = \frac{P_1}{\beta^{P_4}} \left[P_2 - \beta^{P_4} - ln\left(P_3 + \frac{1}{(\beta\gamma)^{P_5}} \right) \right] . \tag{2.4}$$

Where P_{1-5} are fit parameters.

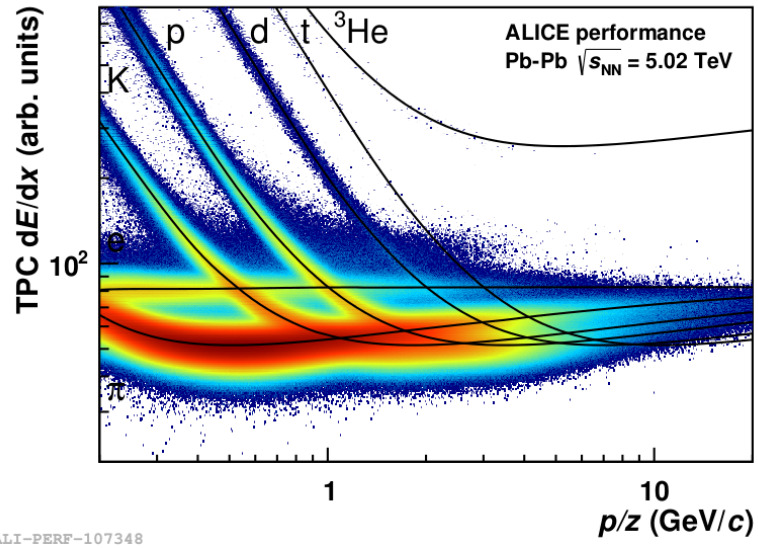

Figure 2.5: Specific energy loss ($\mathrm{d}E/\mathrm{d}x$) in the TPC as a function of the rigidity (p/z) in Pb–Pb collisions at $\sqrt{s_{NN}} = 5.02\,\mathrm{TeV}$, the black lines represent the parametrization of the Bethe-Bloch formula [18].

With the combined information about a particle's rigidity and $\mathrm{d}E/\mathrm{d}x$ in the TPC one can identify it with the help of the parametrized Bethe-Bloch formula.

2.2.3 The Time Of Flight detector

The TOF detector is a gaseous detector that measures the arrival time of particles with a precision of about 80 ps. It has a cylindrical shape, covers the full azimuthal range and is composed of nearly 2000 Multigap Resistive Plate Chambers (MRPC) strips, a stack of resistive glass plates, placed inside gas-tight modules and positioned in the transverse plane.

When a charged particle traverses the detector, it ionizes the gas and the high electric field amplifies this ionization by an electron avalanche. The resistive plates stop the avalanche development in each gap. The signal is the sum of the signals from all gaps. The precise start time of the collision, necessary for a proper measurement of the arrival time of a particle, is given to the TOF detector by the TO detector. Coupled with the ITS and TPC, it provides identification of large samples of charged particles but it is also capable of doing PID on its own (see Fig. 2.6).

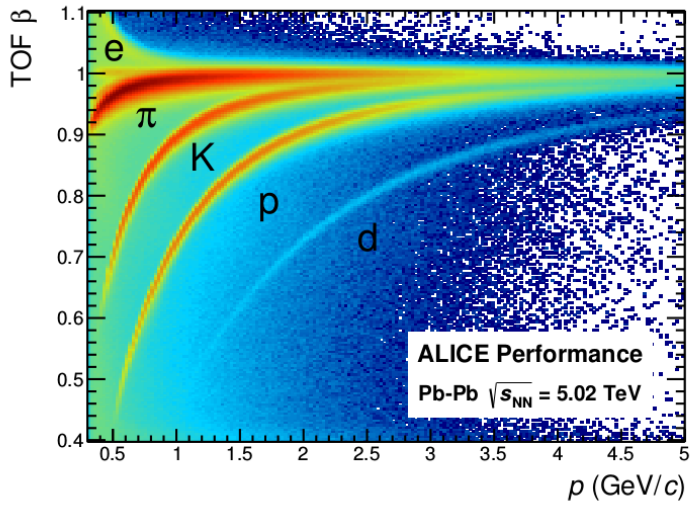

Figure 2.6: Distribution of the velocity β measured by the TOF detector as a function of the momentum [18].

2.3 The analysis software

The software used for this analysis is an Object-oriented ROOT based framework written in C++. It is divided in two parts, AliROOT and AliPhysics. AliROOT contains the basic ROOT and the ALICE specific libraries, useful for data reconstruction, simulation and analysis. AliPhysics contains characteristic analysis tasks and structured packages for each of the analysis groups.

The ALICE data necessary for analyzers is available on the GRID infrastructure via ALIEN (ALICE ENvironment). The GRID is a network of thousands of computers on which parts of the analysis are run in parallel, each of the output files are then merged by the analysis manager. This method of splitting the data allows one to run it in a much faster and efficient way.

Simulations are done using particle generators, which produce particles by recreating elementary processes or by following phenomenological models. GEANT 3 is responsible for the propagation of simulated particles through the detector. The signal produced is treated the same way as real raw signal and the output of the simulation contains the same information as the one of the "real" analysis.

Chapter 3

Data analysis

This analysis uses Pb–Pb data collected in 2015 at a center of mass energy per nucleon pair of $\sqrt{s_{NN}} = 5.02\,\text{TeV}$. This represents about 110 million events.

3.1 Event and track selection

This analysis is a measurement on a mass difference, for this reason, the event selection applied only requires that the considered (anti-)particles come from the primary vertex since the time of flight used for the calculation of the (anti-)particles' masses are measured using the precise start time of the collision (see Eq. 3.4, Sec. 3.4). Thus, no selection is done on the event's centrality and the z-coordinate of the vertex is required to be within 10 cm from the geometrical center of the ALICE experiment.

The tracks selected satisfy the following quality criteria. The pseudorapidity, described as

$$\eta = -\ln\left[\tan(\theta_0/2)\right] , \tag{3.1}$$

is defined in a range $|\eta| < 0.8$, which corresponds to the ALICE acceptance.

The transverse momentum must be high enough for the selected particles to cross the TOF detector so: $p_T > 500\,\text{MeV/c}$.

When a charged particle traverses the TPC, it induces a signal on a given pad-row. If the charge exceeds a certain threshold, it is called a cluster. The maximum number of clusters per track is equal to the number of pad rows in the TPC, which is of 159. For this analysis, the number of clusters registered in the TPC must be at least 70, and the number of clusters used for the determination of the energy loss of a selected particle must be above 50, which is the number of clusters needed to obtain the highest resolution of the TPC.

Findable clusters are geometrically possible clusters, located in dead zones of the detector, which can be assigned to a track. In this case, the ratio of the number of crossed rows and findable clusters in the TPC must be above 0.6, so $N_{\text{crossed rows}}/N_{\text{findable clusters}} > 0.6$.

A selection is also done on the number clusters registered in the ITS, there must be at least 2 with one of them in the SPD.

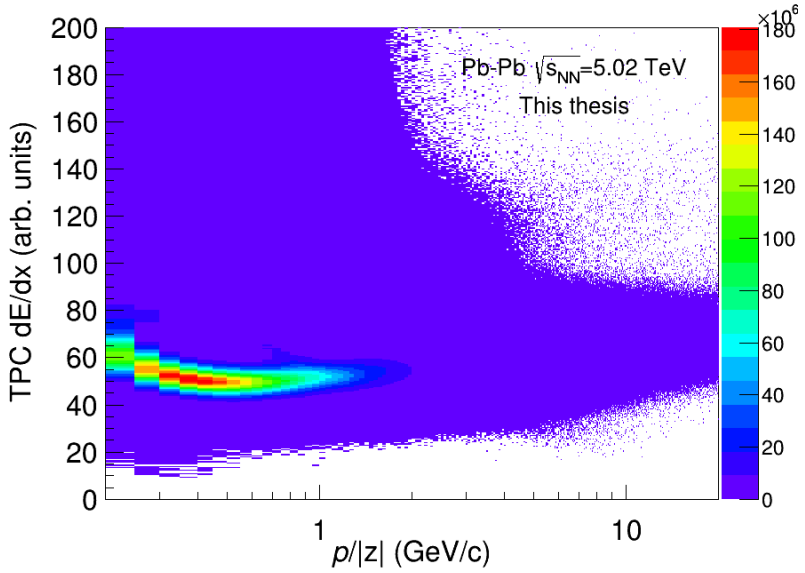

Figure 3.1: Specific energy loss ($\mathrm{d}E/\mathrm{d}x$) in the TPC as a function of the rigidity ($p/|z|$) in Pb–Pb collisions at $\sqrt{s_{NN}} = 5.02\,\mathrm{TeV}$.

In order to reject all the possible secondaries created in the interaction with the detector, a selection on the longitudinal and transverse Distance of Closest Approach (DCA) to the primary vertex is done. More specifically: $|\mathrm{DCA}_z| < 1\,\mathrm{cm}$ and $|\mathrm{DCA}_{xy}| < 0.1\,\mathrm{cm}$. DCA_{xy} is calculated as the quadratic sum of DCA_x and DCA_y. The convention is to set the transverse DCA as negative if the vertex is outside the curvature of track, and positive if it is inside. A more rigorous discussion on the rejection of secondaries can be found in Sec. 3.3.

The procedure for track reconstruction in the detector is done by "linking" iteratively registered clusters together. It is realized in three parts. The first one consists in propagating the track in the inward direction in the TPC and then in the ITS. The same thing is then done in the outward direction, starting with the ITS. The track is then refitted in inward direction again to obtain track parameters at the vertex. This refit is also one of the defined criteria on the quality of the track [19].

Also particles that come from decays with a kink topology, also called *kink daughters*, are not selected for this analysis.

3.2 Particle identification

The selection of the $(\overline{\mathrm{d}})\mathrm{d}$ and $(^3\overline{\mathrm{He}})^3\mathrm{He}$ candidates is done with the TPC and their mass is measured by extracting it with the TOF signal (see Sec. 3.4 and Sec. 3.5). As explained in Sec. 2.2.2, the TPC is able to identify (anti-)particles by simultaneously measuring the rigidity and $\mathrm{d}E/\mathrm{d}x$ signal. In this analysis, this identification is done by applying a "3σ cut" on the measurement of the energy loss by ionization $\mathrm{d}E/\mathrm{d}x$ with respect to the expected value (calculated with the Bethe-Bloch

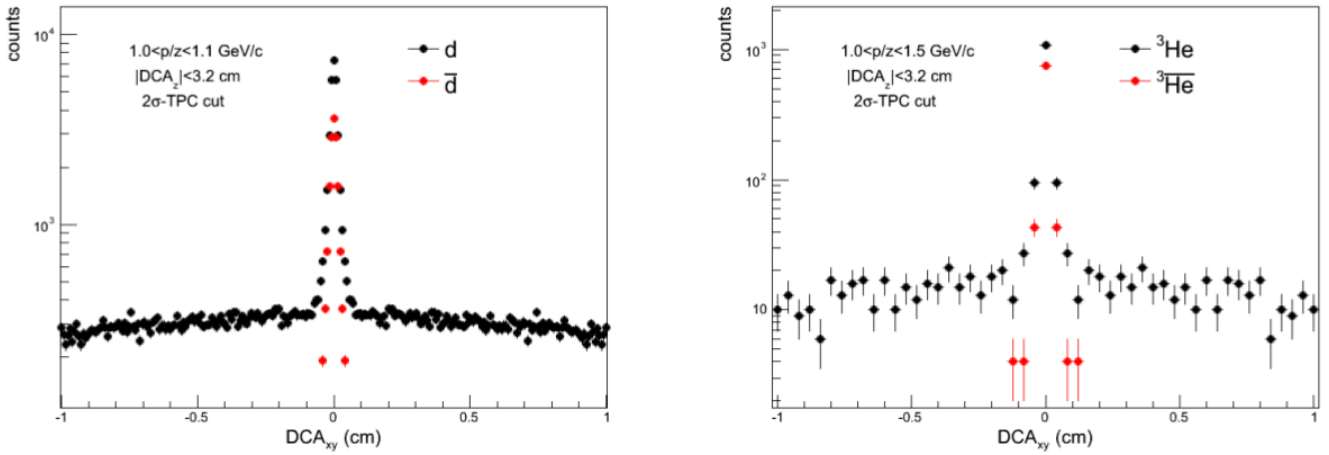

Figure 3.2: DCA_{xy} distribution of $(\overline{\mathrm{d}})\mathrm{d}$ (left) and $(^3\overline{\mathrm{He}})^3\mathrm{He}$ (right) in a rigidity bin $p/|z| = 1.1\,\mathrm{GeV/c}$ and $p/|z| = 1.5\,\mathrm{GeV/c}$, respectively [20].

formula) for a given specie:

$$\left|\frac{\mathrm{d}E/\,\mathrm{d}x_{\mathrm{expected}} - \mathrm{d}E/\,\mathrm{d}x_{\mathrm{measured}}}{\sigma}\right| < 3 \tag{3.2}$$

$$|\Leftrightarrow \mathrm{d}E/\,\mathrm{d}x_{\mathrm{expected}} - \mathrm{d}E/\,\mathrm{d}x_{\mathrm{measured}}| < 3 \cdot \sigma\,. \tag{3.3}$$

σ is the resolution on the measurement of the energy loss by ionization.

On Fig. 2.5 from Sec. 2.2.2, one can find the parametrization of the $\mathrm{d}E/\,\mathrm{d}x$ signal of the $(\overline{\mathrm{d}})\mathrm{d}$ and $(^3\overline{\mathrm{He}})^3\mathrm{He}$. Using this cut rejects all particles that have a signal more than 3σ away of it. This cut is applied for the selection of both $(\overline{\mathrm{d}})\mathrm{d}$ and $(^3\overline{\mathrm{He}})^3\mathrm{He}$ candidates.

3.3 Rejection of secondary nuclei

A cut on the DCA_{xy} at the primary vertex is applied (see Sec. 3.1) to reduce secondary nuclei which are produced in spallation reactions induced in the detector material by the impact of primary particles. Both d and $^3\mathrm{He}$ DCA_{xy} distributions are composed of a central gaussian peak due to the primary nuclei and a flat distribution due the secondary nuclei. The $\overline{\mathrm{d}}$ and $^3\overline{\mathrm{He}}$ distributions are only composed of a central peak since only matter can be created in the interaction with the detector material. A DCA_{xy} distribution from a previous analysis carried out with data taken at $\sqrt{s_{NN}} = 2.76\,\mathrm{TeV}$ [20] is shown on Fig. 3.2 for both (anti-)nuclei, in a low rigidity bin, at which most secondaries are produced.

A cut of $|\mathrm{DCA}_{xy}| < 0.1\,\mathrm{cm}$ is applied in this analysis. It removes, according to the previous analysis, the majority of the secondary deuterons and selects almost all anti-deuterons (99%). The fraction of deuterons that remains after this cut is estimated to be about 30% for $p/|z| \sim 1\,\mathrm{GeV/c}$, and less than 3% for $p/|z| > 1.5\,\mathrm{GeV/c}$. These numbers are presented on Fig. 3.3.

DCA_{xy} distributions from this analysis are shown on Fig. 3.4 for the $(\overline{\mathrm{d}})\mathrm{d}$ and Fig. 3.5 for the $(^3\overline{\mathrm{He}})^3\mathrm{He}$ in two different transverse rigidity bins: $p_T/|z| = [1, 1.5]$ GeV/c and $p_T/|z| =$

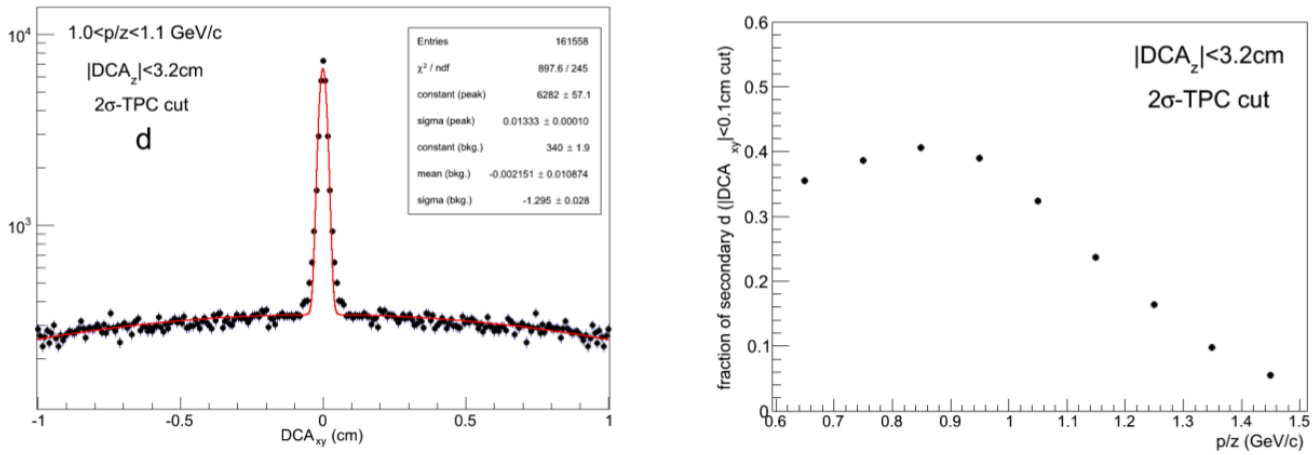

Figure 3.3: Left: fit of the DCA_{xy} distribution of deuterons with a sum of two gaussian distributions. Right: extraction of the fraction of secondary deuterons within the DCA_{xy} cut.

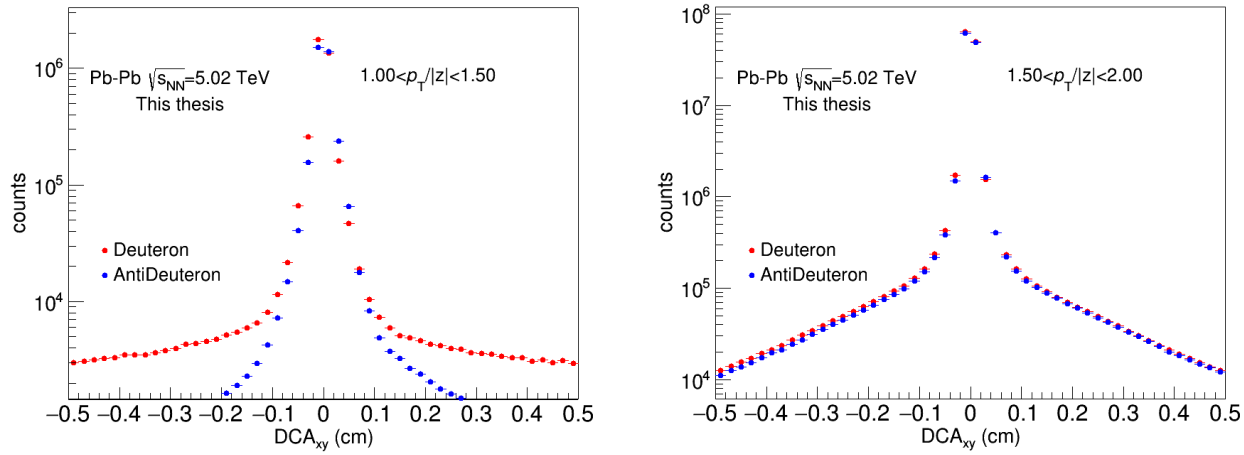

Figure 3.4: DCA_{xy} distribution of the ($\overline{\mathrm{d}}$)d nuclei in transverse rigidity bins $p_T/|z| = [1, 1.5]$ GeV/c (left) and $p_T/|z| = [1.5, 2]$ GeV/c (right) after a cut on the longitudinal DCA of 1 cm.

$[1.5, 2]$ GeV/c. Similarly to the previous analysis, the d and ^{3}He distributions are composed of a central peak and a nearly flat background, and the $\overline{\mathrm{d}}$ and $^3\overline{\mathrm{He}}$ distributions are composed of a central peak only. For both nuclei, the contribution of secondaries is indeed negligible at higher $p_T/|z|$.

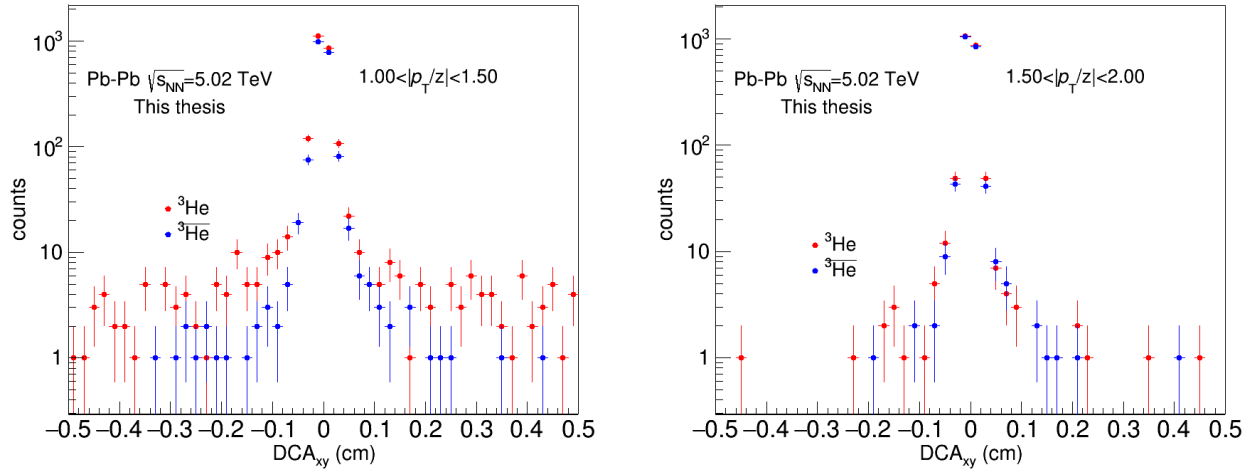

Figure 3.5: DCA$_{xy}$ distribution of the ($^3\overline{\text{He}}$)^{3}He nuclei in transverse rigidity bins $p_T/|z| = [1, 1.5]$ GeV/c (left) and $p_T/|z| = [1.5, 2]$ GeV/c (right) after a cut on the longitudinal DCA of 1 cm.

3.4 Calculation of m^2/z^2 with the time of flight

The squared mass-to-charge ratio m^2/z^2 of the ($\overline{\text{d}}$)d and ($^3\overline{\text{He}}$)^{3}He candidates selected with the TPC were measured with the TOF detector using the following calculation:

$$
\begin{aligned}
p &= \gamma m v \\
\Leftrightarrow m &= \frac{1}{\gamma v} p \\
\gamma &= 1/\sqrt{1 - v^2/c^2} \\
\Rightarrow m &= \frac{\sqrt{1 - v^2/c^2}}{v} p \\
\Leftrightarrow m^2 &= \frac{1 - v^2/c^2}{v^2} p^2 \\
\Leftrightarrow m^2 &= \left(1/v^2 - 1/c^2\right) p^2 \\
v &= L/t_{\text{TOF}} \\
\Rightarrow m^2 &= \left(t_{\text{TOF}}^2/L^2 - 1/c^2\right) p^2 \,.
\end{aligned}
$$

t_{TOF} and L is the particle's measured time of flight and track length. Since the mean rigidity $p/|z|$ –and not the momentum– of the particle is estimated by the detector, one obtains the final Eq. 3.4 for the calculation of the square mass-to-charge ratio:

$$
m^2/z^2 = (p/|z|)^2 \left[(t_{\text{TOF}}/L)^2 - 1/c^2 \right] . \tag{3.4}
$$

The mean of $p/|z|$ is calculated using the measurement of the rigidity at the vertex.

Since the calculation of the squared mass-over-charge ratio directly depends on the reconstructed momentum, a Monte Carlo simulation was done to investigate how well the detector reconstructs the momentum of both (anti-)nuclei species. Fig. 3.6 and Fig. 3.7 show the difference between the true and the reconstructed momentum as a function of the reconstructed momentum

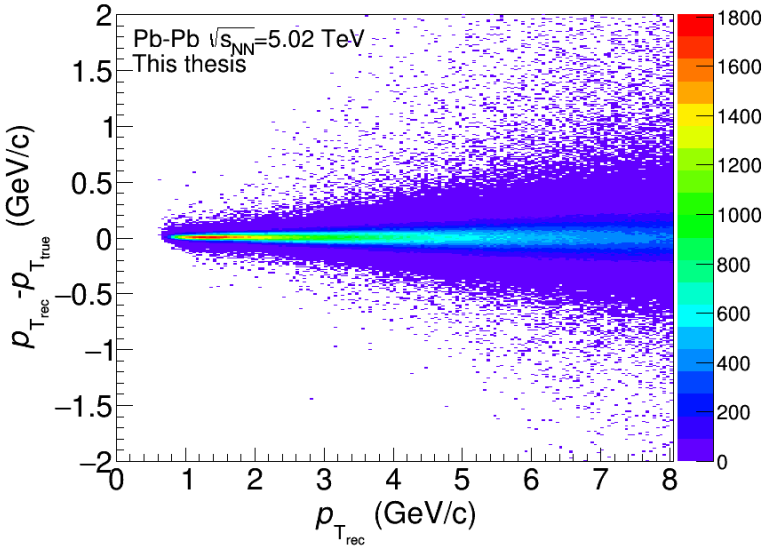

Figure 3.6: Difference between the transverse momentum of reconstructed and true (anti-)deuteron tracks as a function of the reconstructed transverse momentum.

of the $(\overline{\mathrm{d}})\mathrm{d}$ and $(^3\overline{\mathrm{He}})^3\mathrm{He}$, respectively. The outcome is that for the $(\overline{\mathrm{d}})\mathrm{d}$, there is no sign of systematic effect. For the $(^3\overline{\mathrm{He}})^3\mathrm{He}$, however, there is a shift in the low transverse momentum region ($p_T < 1\,\mathrm{GeV/c}$). Because of this effect, the p_T/z range in which the $(^3\overline{\mathrm{He}})^3\mathrm{He}$ mass is measured starts at $1\,\mathrm{GeV/c}$.

3.5 Extraction of m^2/z^2 with the TOF signal

The final TOF signal is the squared mass-to-charge ratio distribution of all the candidates that have passed the track quality cuts from Sec. 3.1 and the TPC selection. m^2/z^2 defined in Eq. 3.4 is then measured by fitting this signal. For both nuclei a gaussian function with an exponential tail that represents the time signal distribution of the TOF detector is used to fit this signal, it is given by the following formula [21]:

$$s(x) = \begin{cases} \frac{C}{N\sqrt{2\pi}\sigma} \exp\left(\frac{-(x-x_0)^2}{2\sigma^2}\right) & \text{if } x < x_0 + d\sigma \\ \frac{C}{N\sqrt{2\pi}\sigma} \exp\left(a_s(x_0 + d\sigma - x) - 0.5d^2\right) & \text{if } x \geq x_0 + d\sigma \end{cases} \tag{3.5}$$

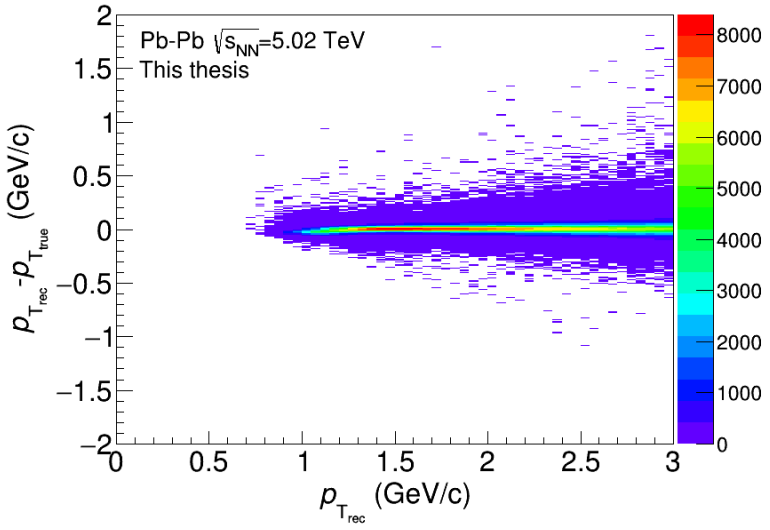

Figure 3.7: Difference between the transverse momentum of reconstructed and true (anti-)deuteron tracks as a function of the reconstructed transverse momentum.

With

$$x = m^2/z^2\,,$$
$$N = 0.5(1 + \mathrm{Erf}\big(d/\sqrt{2}\big)) + \exp(-0.5d^2)\frac{1}{\sqrt{2\pi}\sigma a_s}\,.$$
$$a_s = \frac{d}{\sigma}\,,$$
$$C := \text{ constant}\,,$$
$$x_0 := \text{ mean of the gaussian part of the signal function}\,,$$
$$\sigma := \text{ standard deviation of the gaussian part of the signal function}\,,$$
$$d := \text{ start of the exponential part of the function in units of the standard deviation}\,.$$

The transition from the gaussian to the exponential is a free parameter of the fit and the requirement on the slope is that the first derivative of the function must be continuous, this is the reason why $a_s = \frac{d}{\sigma}$.

3.5.1 (Anti-)Deuteron TOF signal analysis

The background of the ($\overline{\mathrm{d}}$)d distribution originates from various components: wrong associations of a track with a TOF hit, non-Gaussian tail of lower mass particles and contamination of other hadrons in the $\mathrm{d}E/\,\mathrm{d}x$ in the region $p_T/|z| > 1.5\,\mathrm{GeV}$. For this reason, only a simple exponential is needed to fit it for $p_T/|z| < 1.3$. For $p_T \geq 1.3$ a double exponential is necessary to describe the change of slope in background. The extraction of m^2/z^2 is done in a $p_T/|z|$ range from 1 to 2 GeV/c in steps of 100 MeV, from 2 to 3 GeV/c in steps of 250 MeV and from 3 to 4 GeV/c in steps of 500 MeV. Examples of the fitted squared mass-to-charge ratio distributions are shown

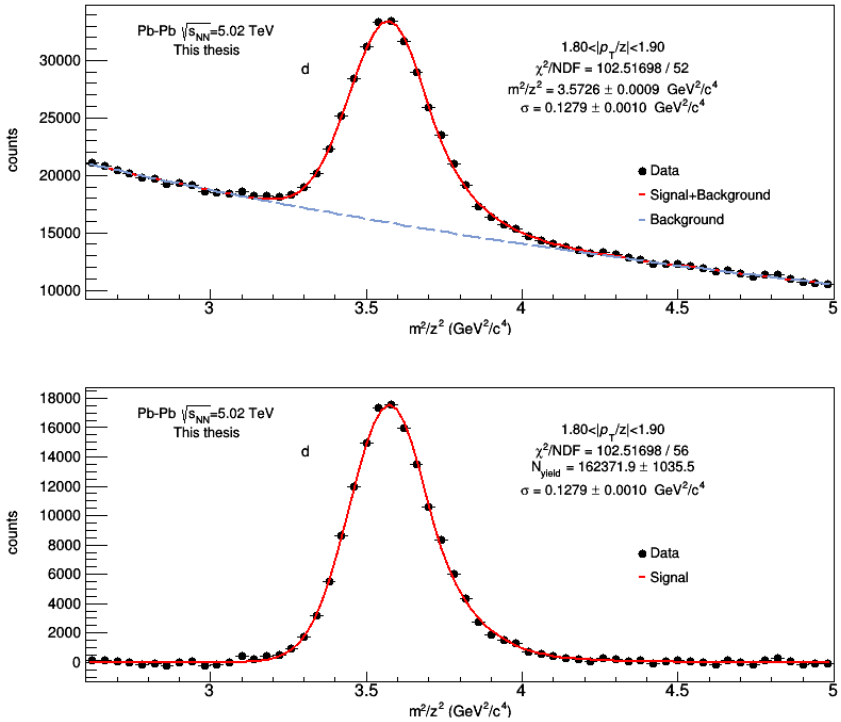

Figure 3.8: TOF squared mass-to-charge ratio distribution of the d in transverse momentum range $p_T/|z| = [1.80, 1.90]$. On top is the whole distribution with signal+background fit, on the bottom is the distribution with subtracted background and a signal fit.

below on Fig. 3.8 and Fig. 3.9. One can also find all the fits used for the extraction of m^2/z^2 in the appendix A.

As previously explained in Sec. 3.5, the squared mass-to-charge ratio is extracted from a fit parameter of the fit function: the mean of its gaussian part. The yield is also calculated by integrating the distribution with subtracted background.

3.5.2 (Anti-)Helium-3 TOF signal analysis

The energy loss by ionization described by Eq. 2.3 is dependent on the mass and the squared charge of the (anti-)particle. Since $(^3\overline{\text{He}})^3$He has a heavy mass and a squared charge number of 4, its distance from the neighboring hadrons differs from a factor 4. The TOF signal of the $(^3\overline{\text{He}})^3$He has therefore negligible contamination from other hadrons and no background fitting and subtraction is needed. The extraction of m^2/z^2 is done in a $p_T/|z|$ range from 1 to 3 GeV/c in steps of 500 MeV. Examples of the fitted squared mass-to-charge ratio distributions are shown below on Fig. 3.10 and Fig. 3.11. One can also find all the fits used for the extraction of m^2/z^2 of the $(^3\overline{\text{He}})^3$He in the appendix B.

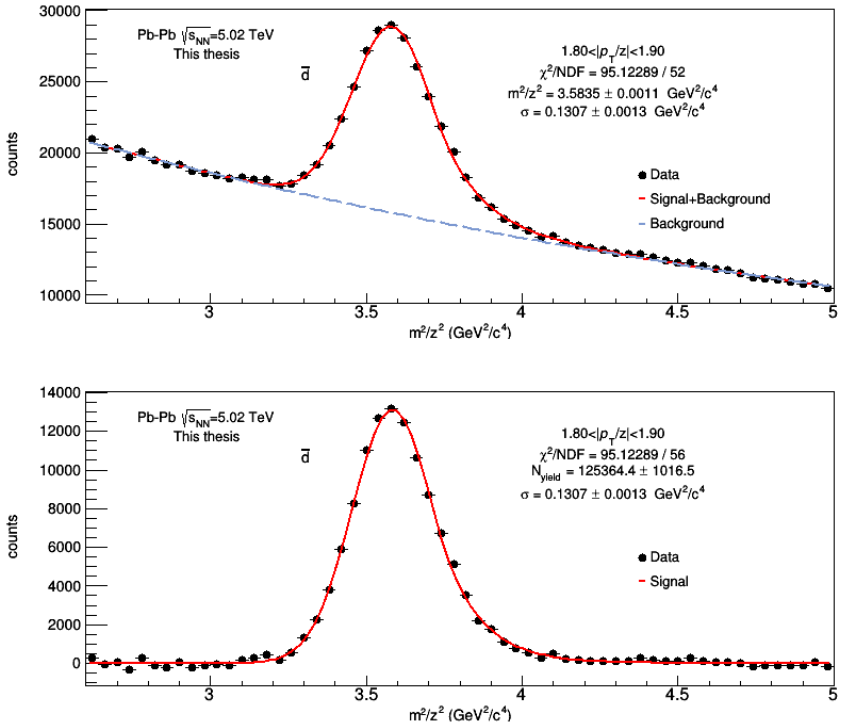

Figure 3.9: TOF squared mass-to-charge ratio distribution of the $\bar{\mathrm{d}}$ in transverse momentum range $p_T/|z| = [1.80, 1.90]$.

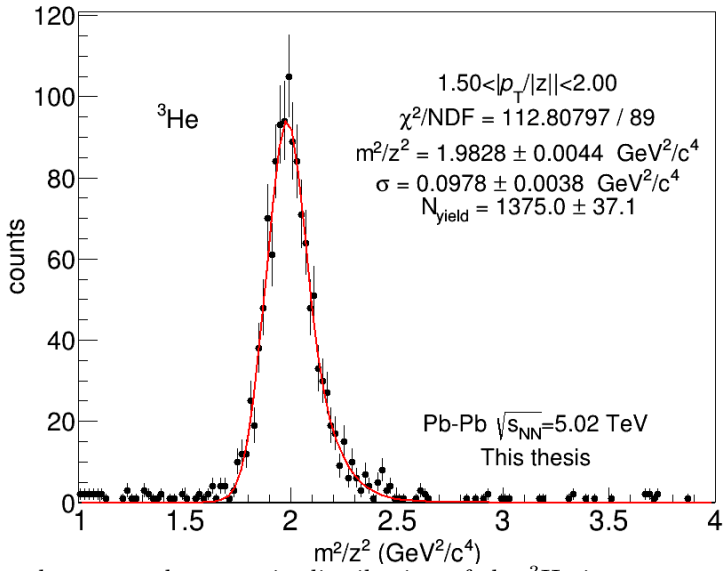

Figure 3.10: TOF squared mass-to-charge ratio distribution of the ^{3}He in transverse momentum range $p_T/|z| = [1.50, 2.00]$.

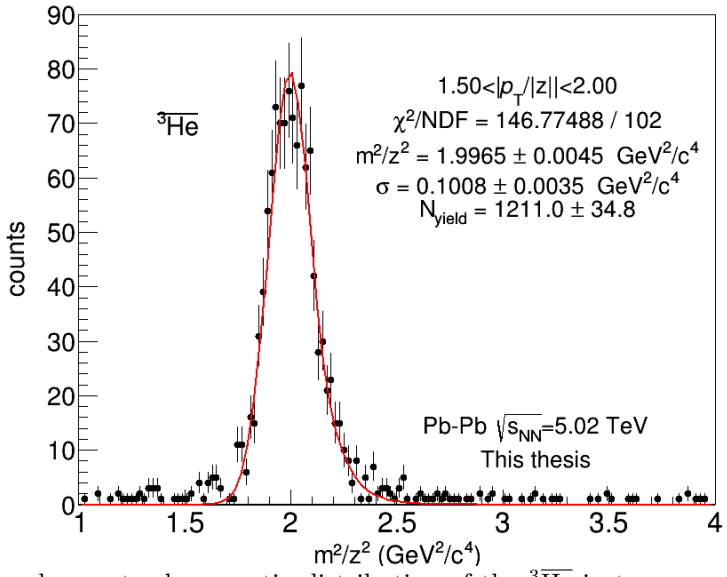

Figure 3.11: TOF squared mass-to-charge ratio distribution of the $^3\overline{\text{He}}$ in transverse momentum range $p_T/|z| = [1.50, 2.00]$.

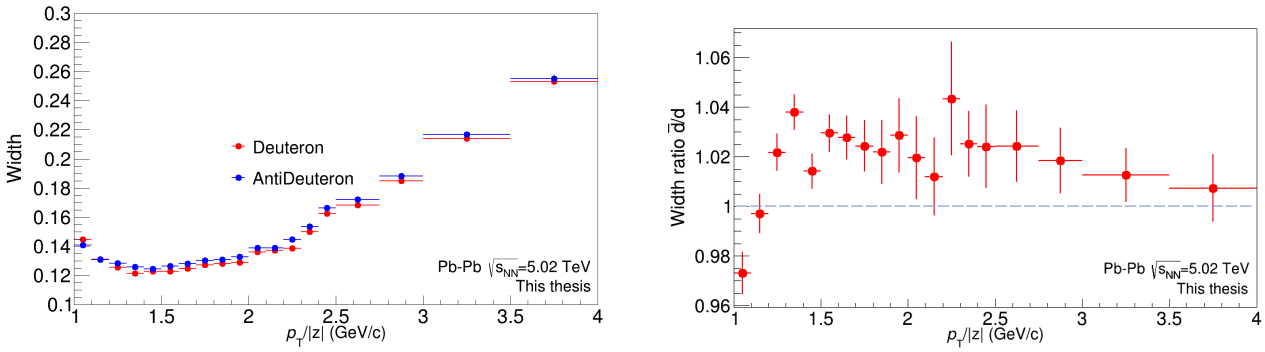

Figure 3.12: Left: Width of the $(\overline{\text{d}})$d m^2/z^2 distributions. Right: ratio of the $(\overline{\text{d}})$d m^2/z^2 distributions' width as a function of the transverse rigidity. The vertical bars represent the statistical uncertainties.

3.5.3 Width of the TOF signal for nuclei and anti-nuclei

In Fig. 3.12, the widths of the d and $\overline{\text{d}}$ squared mass-over-charge ratio distributions are presented. They get wider for increasing $p_T/|z|$, starting at 1.5 GeV/c. This is explained by the decline of the TPC resolution for increasing momentum [15]. Their ratios are also shown on Fig. 3.12, which are almost systematically above unity. The anti-deuteron squared mass-over-charge distributions are then slightly larger than the ones of the deuteron. This is an unexpected result as the detector should behave symmetrically for oppositely charged particles, this is a hint for a detector effect which is not fully understood yet. However this effect is assumed not to alter the measurement on the mass difference. The same study was done for the $(^3\overline{\text{He}})^3$He. The results are consistent with unity and displayed on Fig. 3.13.

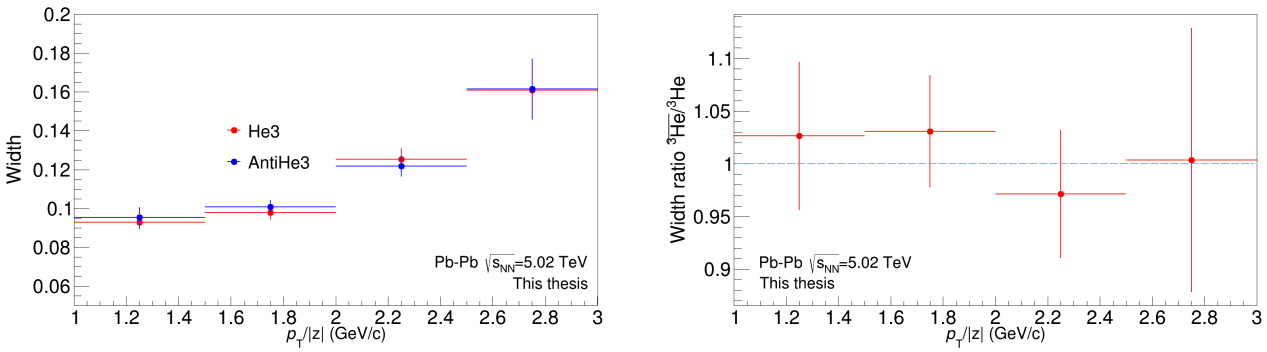

Figure 3.13: Left: Width of the $(^3\overline{\mathrm{He}})^3\mathrm{He}$ m^2/z^2 distributions as a function of the transverse rigidity. Right: Ratio of the $(^3\overline{\mathrm{He}})^3\mathrm{He}$ m^2/z^2 distributions' width as a function of the transverse rigidity. The vertical bars represent the statistical uncertainties.

Chapter 4

Results

4.1 Mass difference between matter and anti-matter

4.1.1 d–$\overline{\mathrm{d}}$ mass difference

The squared mass-over-charge ratios of the (anti-)deuteron measured in this analysis are shown on Fig. 4.1. For both d and $\overline{\mathrm{d}}$, m^2/z^2 approach a value around $3.57\,\mathrm{GeV}^2/\mathrm{c}^4$ asymptotically. This effect, independently of the (anti-)particle charge, comes from the energy loss in the detector. In fact, the calculation of the squared mass-over-charge ratio (see Eq. 3.4) is done with the time of flight of the (anti-)nuclei, which is a variable that does not take into account the energy lost by an (anti-)particle while traversing the detector, which is especially high for heavier masses. Because of this effect, low momenta (anti-)particles lose more energy than high momenta particles and have a longer time of flight, this results in a mass up to 2% heavier than the real mass for the (anti-)proton, 4% for the (anti-)deuteron (see Fig. 4.4) and 3% for the $(^3\overline{\mathrm{He}})^3\mathrm{He}$ (see Fig. 4.8). It is possible to correct this systematic effect with a Monte Carlo simulation. The procedure is to calculate m^2/z^2 for $(\overline{\mathrm{d}})\mathrm{d}$ particles generated with a Monte Carlo simulation and to then scale the measured squared mass-over-charge ratio obtained with the real data in each rigidity bin. The results of this correction are also presented on Fig. 4.1. This method indeed corrects the systematic effect of the squared mass-over-charge ratios of the deuteron and anti-deuteron, but not the one of the mass difference: the mass of the anti-deuteron is indeed systematically heavier than the one of the deuteron. This is due to the small difference between the reconstructed mass of the simulated deuteron and anti-deuteron, depicted on Fig. 4.2. One concludes that the simulation only takes one systematic effect into account and does not perfectly describe real data.

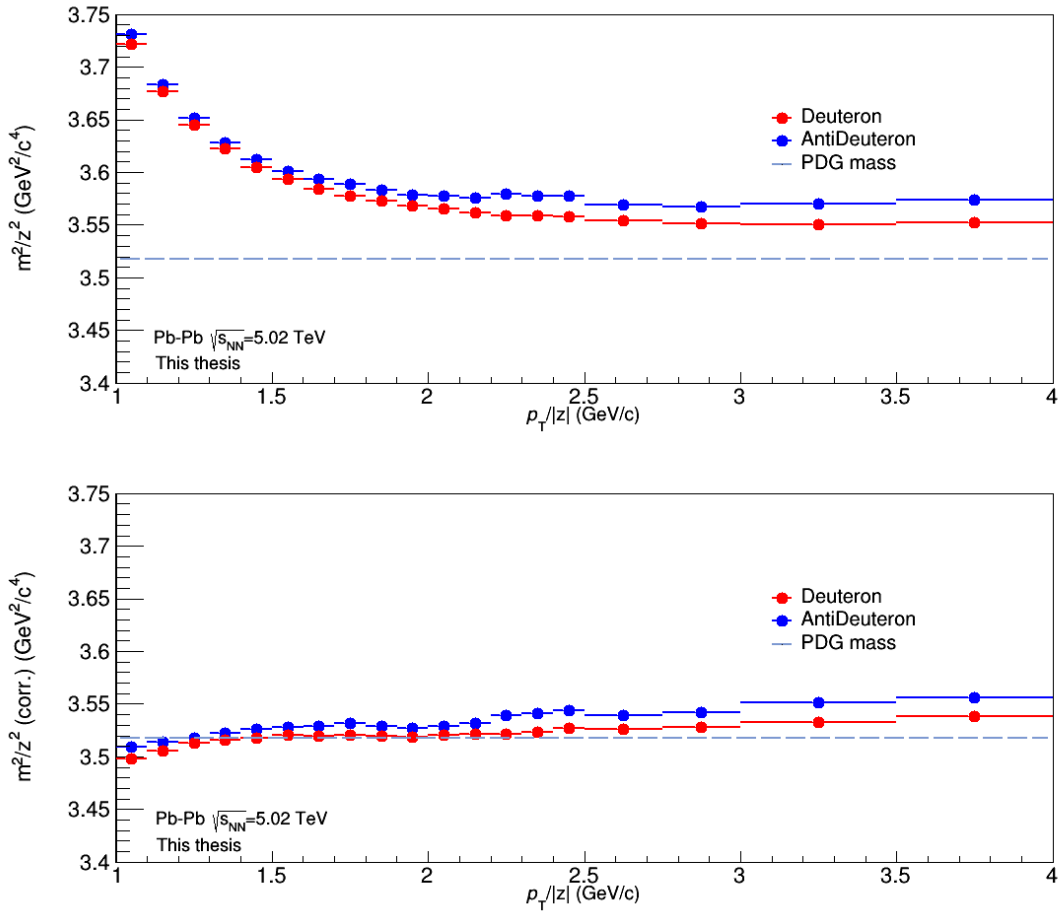

Figure 4.1: Top: d and $\overline{\text{d}}$ squared mass-over-charge ratio measurement as a function of the transverse rigidity. Bottom: d and $\overline{\text{d}}$ mass-over-charge ratio measurement corrected with the (anti-)deuteron mass obtained from the simulation, without the correction with the measured (anti-)proton mass.

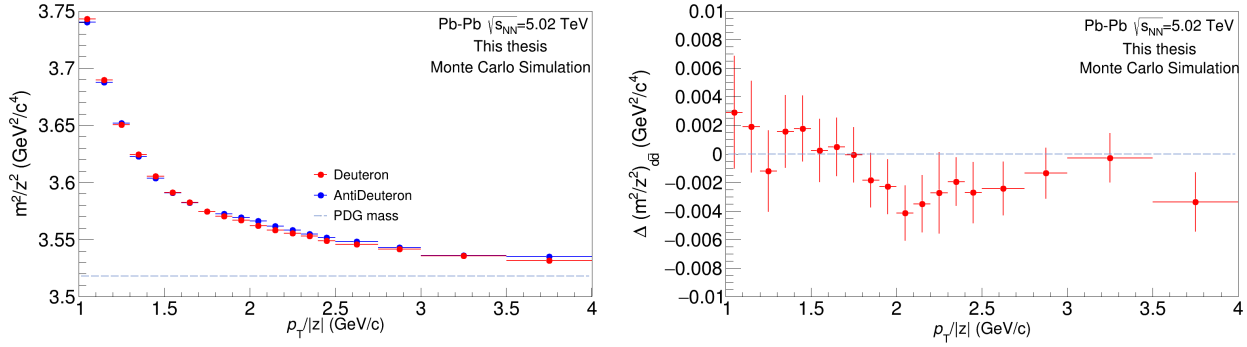

Figure 4.2: Left: Squared mass-over-charge ratio of the deuteron (in red) and anti-deuteron (in blue). Right: squared mass-over-charge ratio difference between the deuteron and anti-deuteron. The results are consistent with zero.

A data-driven method is therefore chosen to correct the (anti-)nuclei masses by scaling them with the ratio between the (anti-)proton masses recommended by the Particle Data Group (PDG) and the ones measured in the analysis with the same method (described in Sec. 3.5.1) as for the

(anti-)deuteron:

$$m^2/z^{2\,\mathrm{corr.}}_{(\bar{A})A} = \frac{m^2/z^{2\,\mathrm{PDG}}_{p\bar{p}}}{m^2/z^2_{p\bar{p}}} m^2/z^2_{(\bar{A})A}\,. \tag{4.1}$$

This correction has also been done in the previous analysis with Run 1 data at 2.76 TeV published in *Nature Physics* [22].

The squared mass-over-charge ratio of the proton and anti-proton is shown on Fig. 4.3. For both (anti-)particles it approaches a value around $0.895\,\mathrm{GeV}^2/\mathrm{c}^4$ asymptotically. The difference of the squared mass-over-charge ratio between the proton and anti-proton is also shown on Fig. 4.3, it becomes significantly bigger for increasing $p_T/|z|$, starting at $1.5\,\mathrm{GeV/c}$.

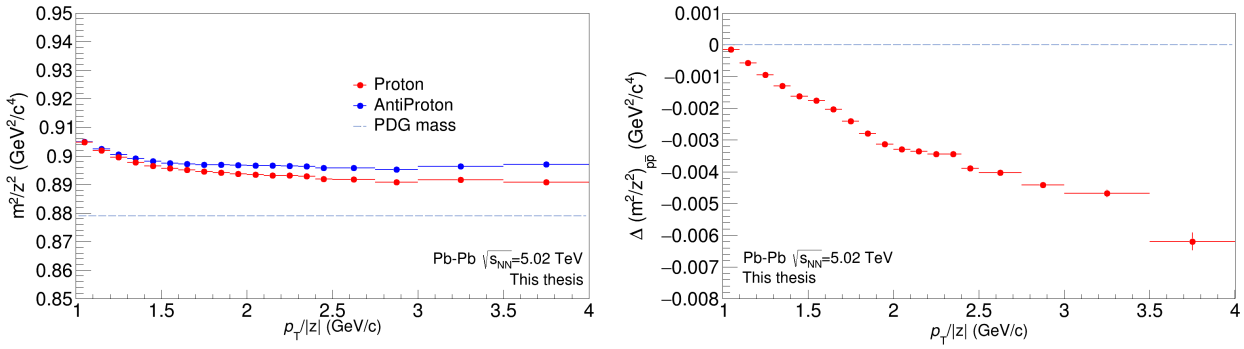

Figure 4.3: Left: Squared mass-over-charge ratio of the proton (in red) and anti-proton (in blue). Right: squared mass-over-charge ratio difference between the proton and anti-proton. Vertical bars show the combined statistical uncertainties, assuming they are uncorrelated.

The final squared mass-over-charge ratio of the (anti-)deuteron measured in this analysis and corrected with the (anti-)proton masses are shown on Fig. 4.4. After correction, the effect observed for the absolute value of the squared mass-over-charge ratio is partially corrected but still present since the mass of the (anti-)proton is also overestimated because of the measurement of the squared mass-over-charge ratio without energy loss correction, as explained previously. For the squared mass-over-charge ratio difference, however, the results are impressive: the observed systematic effect is completely absorbed after correction (see Fig. 4.5).

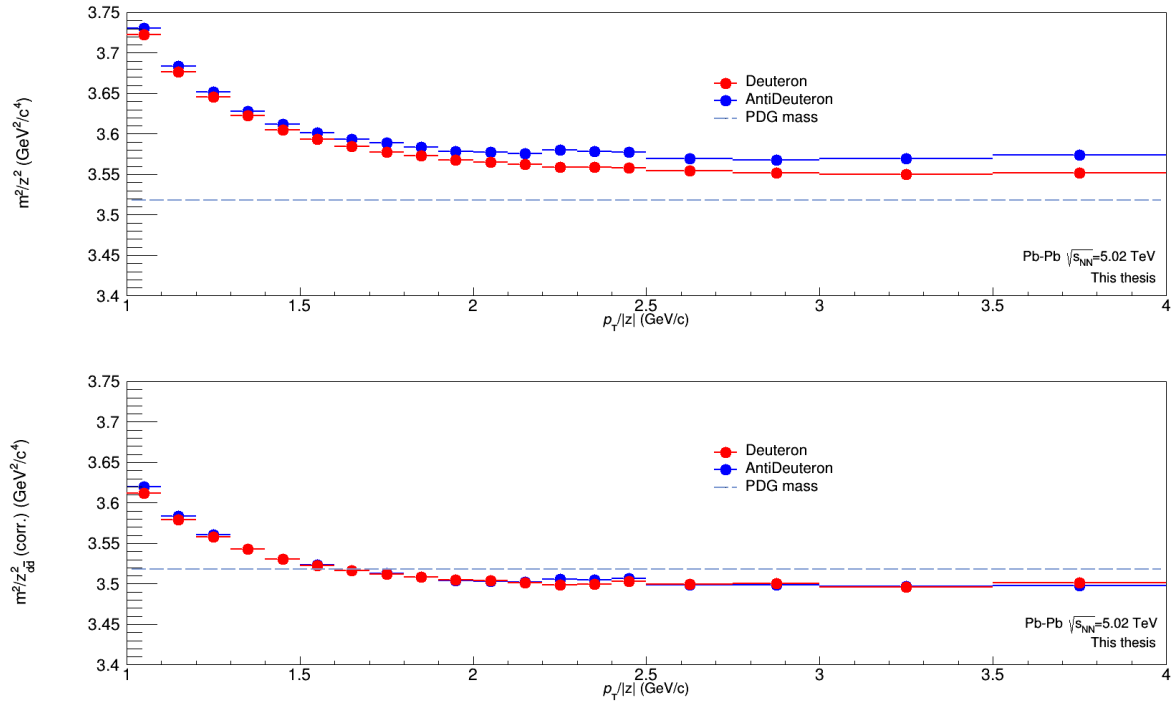

Figure 4.4: Top: d and $\overline{\text{d}}$ squared mass-over-charge ratio measurement. Bottom: d and $\overline{\text{d}}$ mass-over-charge ratio measurement corrected with the (anti-)proton mass. The first three points are a systematic deviation due to the small mass difference between the proton and anti-proton mass in the low $p_T/|z|$ region.

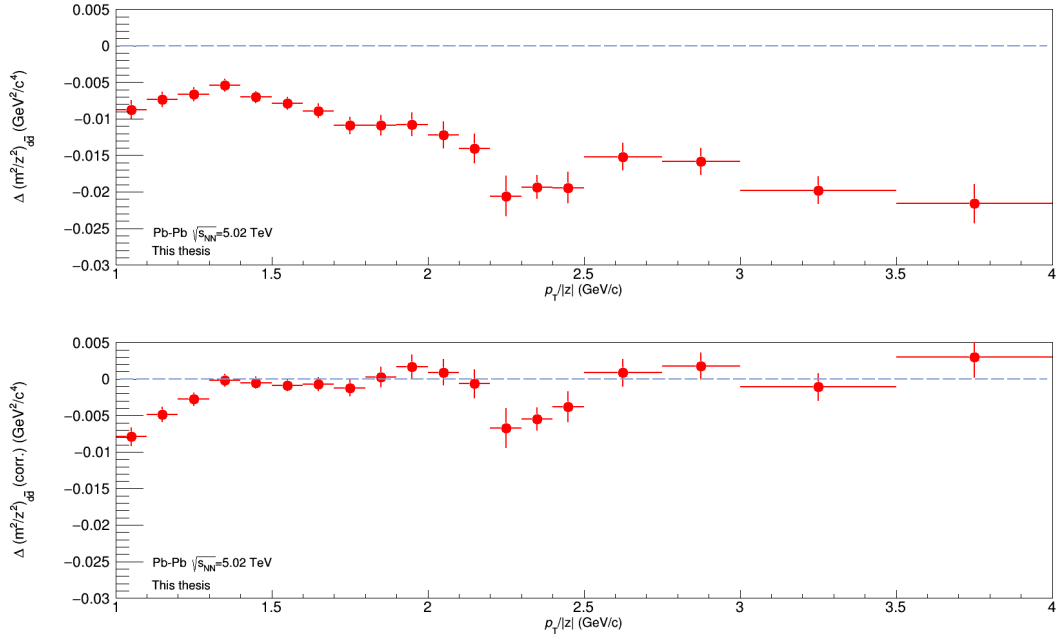

Figure 4.5: d–$\overline{\text{d}}$ mass-over-charge ratio difference as a function of the transverse rigidity. Bottom: the same measurement corrected with the (anti-)proton mass. Vertical bars show the statistical uncertainties.

The discrepancy between the squared mass-over-charge ratio of the deuteron and anti-deuteron has also been reported by [20]. It showed that a systematic effect occurs, for the (anti-)deuteron as well as for the (anti-)proton, for the squared mass-to-charge ratio difference in each rigidity bin

and that it approaches 1% in the magnetic field configuration B(−−) and 2% in B(++) for all negative pseudorapidity bins and decreases from the positive central to large pseudorapidity bins. This pseudorapidity and magnetic field orientation dependence is depicted on Fig. 4.6. This study has been done with data taken in 2011 at a center-of-mass energy per nucleon pair of 2.76 TeV. It has never been done with the data used for this analysis. Thus, future measurements of the squared mass-to-charge ratio in various rigidity and pseudorapidity bins and magnetic field orientations must be carried out in order to fully confirm the assumption on the origin of the systematic effect observed on Fig. 4.5.

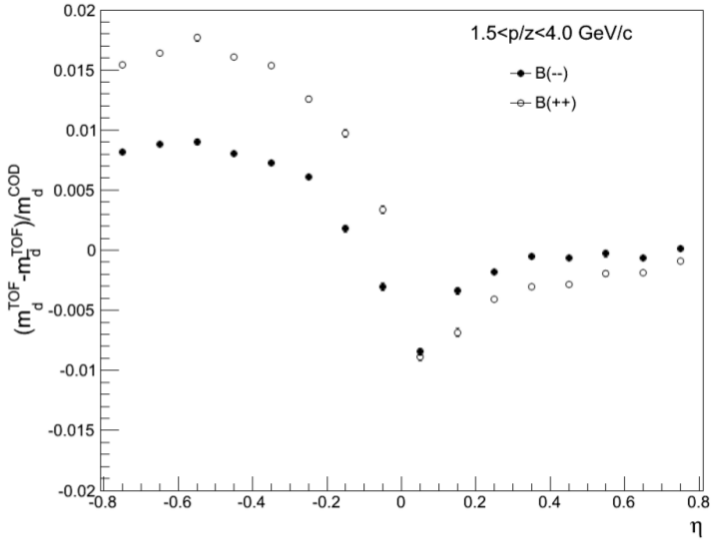

Figure 4.6: Measurement of the mass-to-charge ratio difference between d and $\overline{\mathrm{d}}$, normalized by the d mass-to-charge ratio recommended by CODATA, as a function of the pseudorapidity estimated as the weighted mean of the measurements obtained in the rigidity bins in the range $1.5 < p/|z| < 4.0\,\mathrm{GeV/c}$ [20].

4.1.2 ^{3}He–$^3\overline{\text{He}}$ mass difference

The squared mass-over-charge ratio of the $(^3\overline{\text{He}})^3$He is also corrected with the (anti-)proton mass and the mass distributions of the proton and anti-proton used for the scaling of the $(^3\overline{\text{He}})^3$He masses are shown on Fig. 4.7. The final squared mass-over-charge ratios of the $(^3\overline{\text{He}})^3$He and their difference are shown on Fig. 4.8 and Fig. 4.9, respectively. The large statistical uncertainties due to the small statistics and the large binning make the systematic effect observed for the mass difference between the deuteron and anti-deuteron less striking for the $(^3\overline{\text{He}})^3$He. They also "absorb" the correction with the (anti-)proton mass, resulting in uncorrected and corrected mass differences in agreement with each other within their uncertainties.

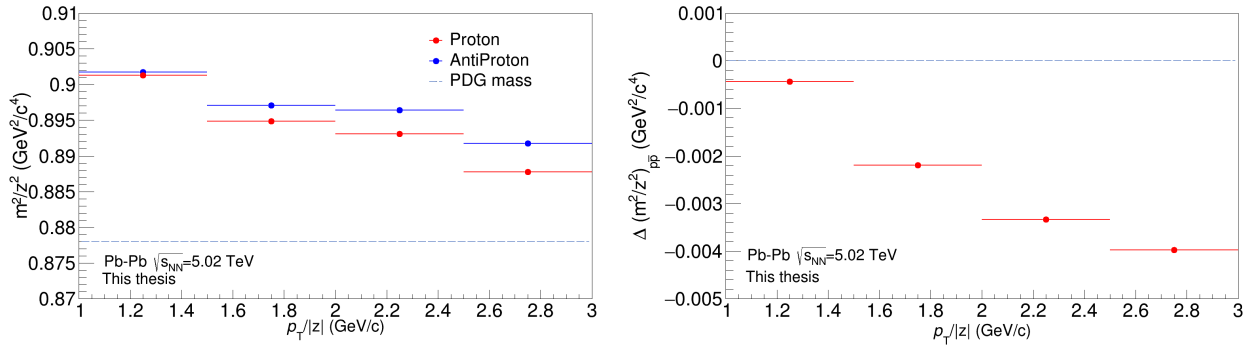

Figure 4.7: Left: Squared mass-over-charge ratio of the proton (in red) and anti-proton (in blue) in the same $p_T/|z|$ bins as the $(^3\overline{\text{He}})^3$He. Right: squared mass-over-charge ratio difference between the proton and anti-proton.

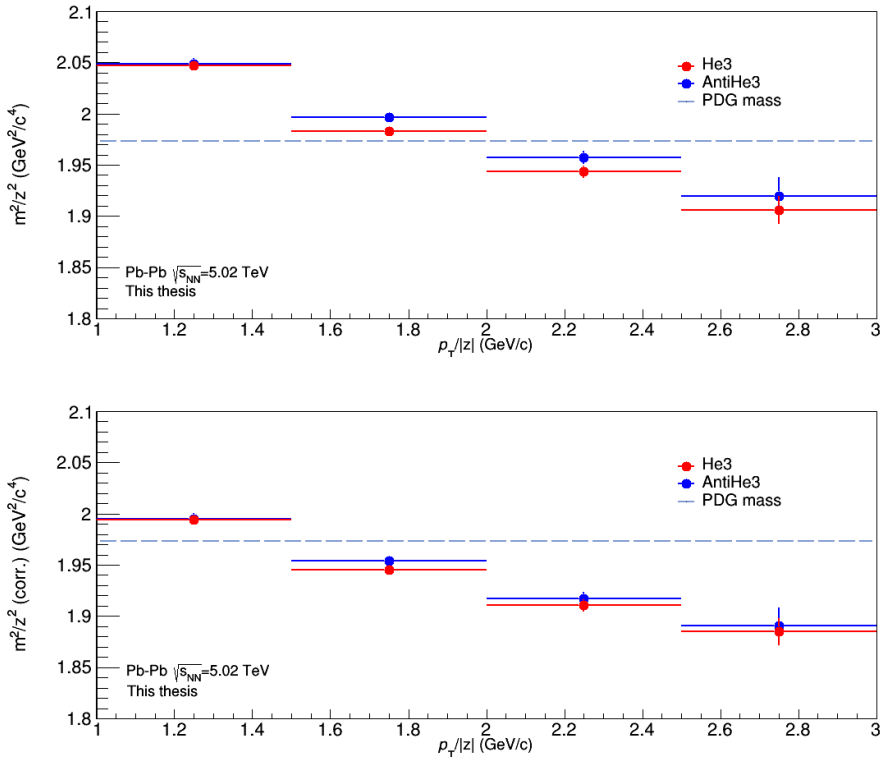

Figure 4.8: Top: uncorrected ^{3}He and $^3\overline{\text{He}}$ squared mass-over-charge ratio as a function of the transverse rigidity. Bottom: ($^3\overline{\text{He}}$)^{3}He squared mass-over-charge ratio corrected with the (anti-)proton mass.

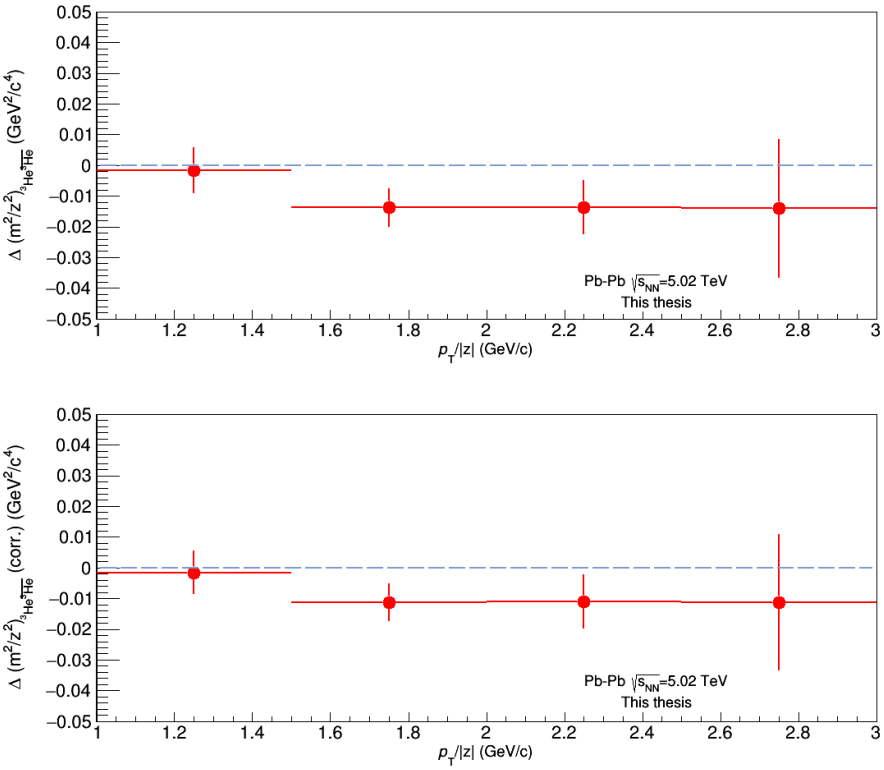

Figure 4.9: Uncorrected (top) and corrected (bottom) ^{3}He–$^3\overline{\text{He}}$ squared mass-over-charge ratio difference. Vertical bars show the combined statistical uncertainties, assuming they are uncorrelated.

4.2 Anti-nuclei to nuclei yield ratios

4.2.1 $\overline{\text{d}}$–d yield ratio

Fig. 4.10 shows the acceptance×efficiency of the reconstruction of the deuteron and anti-deuteron estimated using Monte Carlo simulations. The reconstructed particles satisfy the same selection used for the analysis with real data. It is calculated as the ratio of the number of particles detected by the detector to the number of generated particles. In both cases, the rise of the efficiency in the low $p_T/|z|$ region is determined by energy loss and multiple scattering processes of the incident particle with the detector material. For both (anti-)nuclei the efficiency reaches almost a saturation value, which is higher for matter than for anti-matter because of the absorption of anti-matter by the detector material.

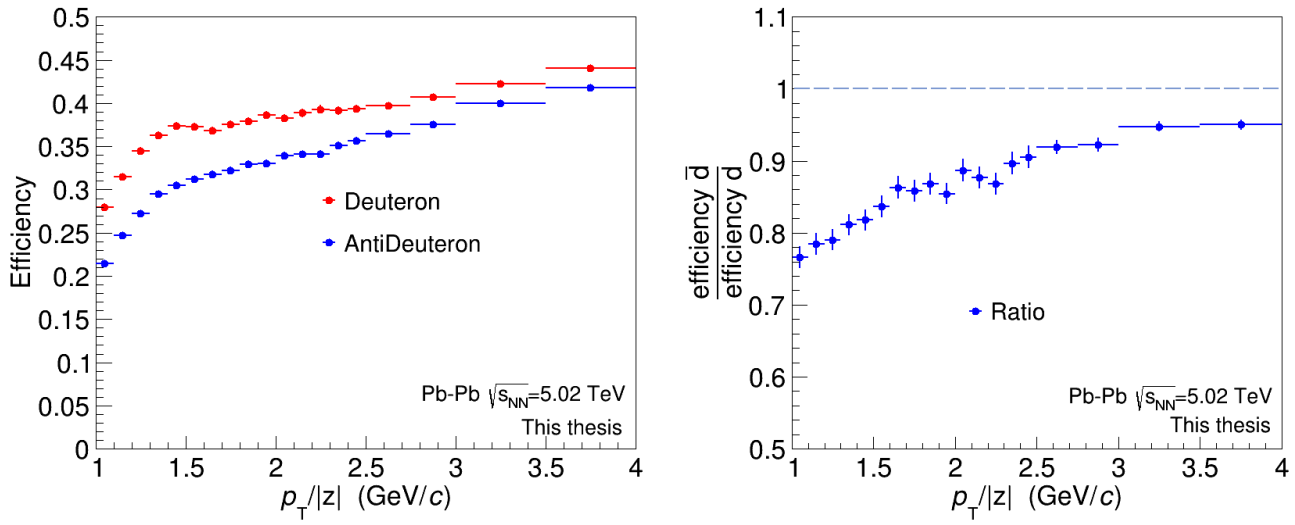

Figure 4.10: Left: number of reconstructed tracks over generated tracks ratio as a function of the transverse rigidity for d (in red) and $\overline{\text{d}}$ (in blue). Right: Efficiency ratio of $\overline{\text{d}}$ over d. The binning was adjusted to correspond to the one chosen for the squared mass-over-charge ratio and yield extraction.

The yields of the deuteron and anti-deuteron are presented on Fig. 4.11. It is calculated the same way for ($\overline{\text{d}}$)d and ($^3\overline{\text{He}}$)^{3}He: by integrating the squared mass-over-charge ratio distributions with subtracted background and scaling them with the width of the corresponding $p_T/|z|$ range. As expected, because of the difference in the reconstruction efficiency of matter compared to anti-matter, the yields of the anti-deuteron are systematically lower than the ones of the deuteron. The corrected yield ratio between $\overline{\text{d}}$ and d for each $p_T/|z|$ range is shown on Fig. 4.12. It approaches unity for increasing transverse rigidity. Yet, there is still a remaining difference between the d and $\overline{\text{d}}$ yields, even after correction. The reason why is that the simulation is ran with GEANT 3 which includes an imperfect description of the interaction of (anti-)nuclei with the detector because of the limited data available on collisions of light nuclei with heavier materials. A possible alternative is to also use GEANT 4, which has a different transport code. One then estimates the difference between GEANT 3 and GEANT 4 as a systematic uncertainty. For future measurements, however, a more precise measurement of nuclei absorption in the detector material is needed.

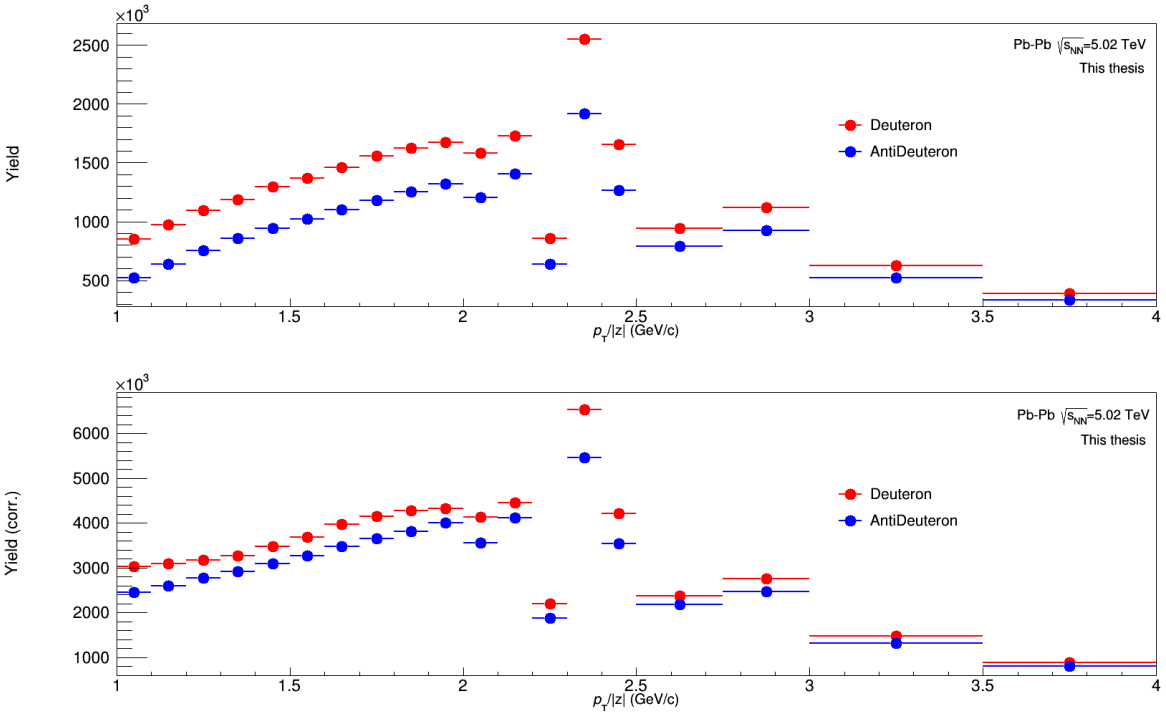

Figure 4.11: Uncorrected (top) and corrected (bottom) yield of d and $\overline{\mathrm{d}}$.

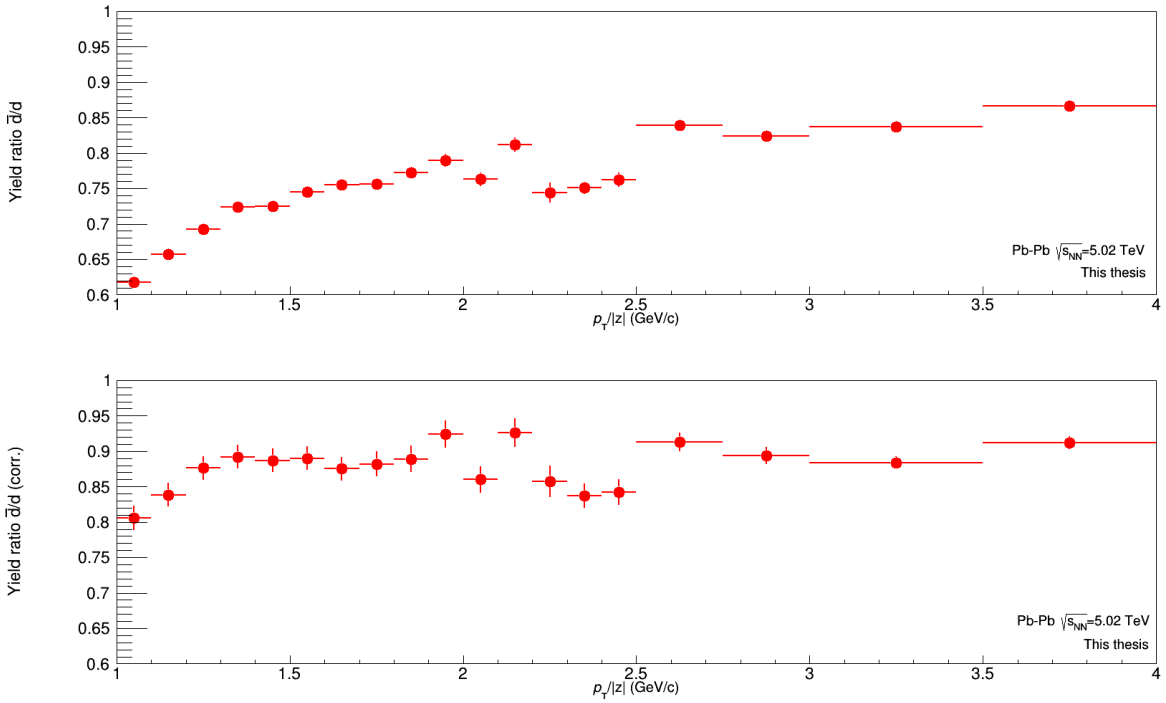

Figure 4.12: Left: Yield ratio of $\overline{\mathrm{d}}$ over d as a function of the transverse rigidity. Right: Yield ratio of $\overline{\mathrm{d}}$ over d as a function of the transverse rigidity, corrected for the efficiency. The vertical bars represent the combined statistical uncertainties, assuming they are uncorrelated.

4.2.2 $^3\overline{\text{He}}$–^{3}He yield ratio

On Fig. 4.13, the acceptance×efficiency of the reconstruction of ^{3}He and $^3\overline{\text{He}}$ is shown as well as the ratio. The result here is the same as for the (anti-)deuteron, the reconstruction efficiency is systematically smaller for $^3\overline{\text{He}}$ compared to ^{3}He, especially at low $p_T/|z|$, due to the absorption of anti-matter.

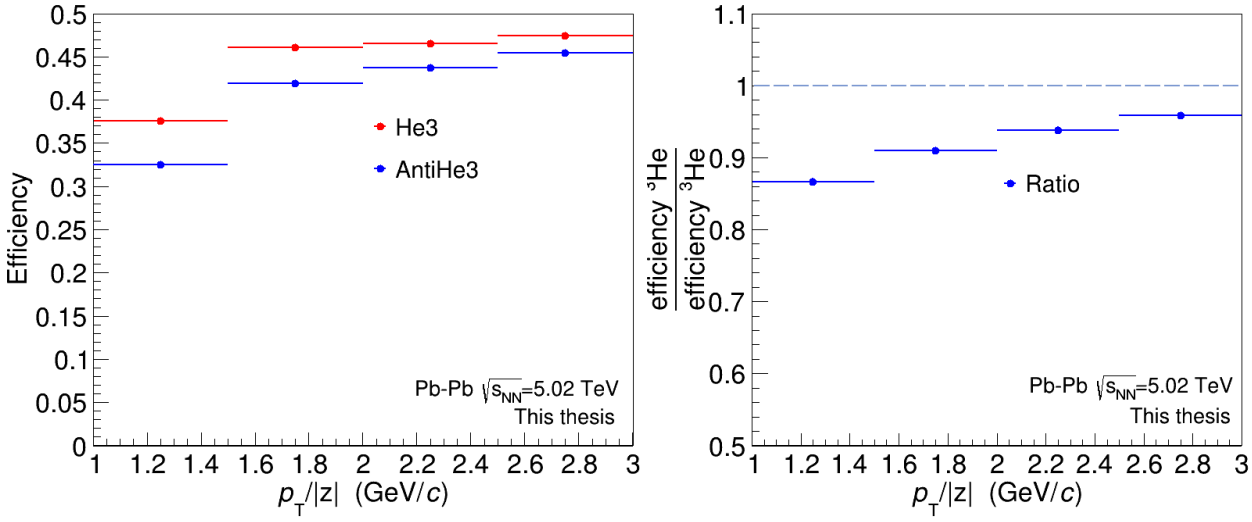

Figure 4.13: Left: number of reconstructed tracks over generated tracks ratio as a function of the transverse rigidity for ^{3}He (in red) and $^3\overline{\text{He}}$ (in blue). Right: Efficiency ratio of $^3\overline{\text{He}}$ over ^{3}He. The binning was adjusted to correspond to the one chosen for the squared mass-over-charge ratio and yield extraction.

The yields of ^{3}He and $^3\overline{\text{He}}$ are presented in Fig. 4.14. There is a clear decrease in the production of ($^3\overline{\text{He}}$)^{3}He at higher $p_T/|z|$. The yield ratio between $^3\overline{\text{He}}$ and ^{3}He for each $p_T/|z|$ range is shown on Fig. 4.15. The results are consistent with unity after correcting for the reconstruction efficiency.

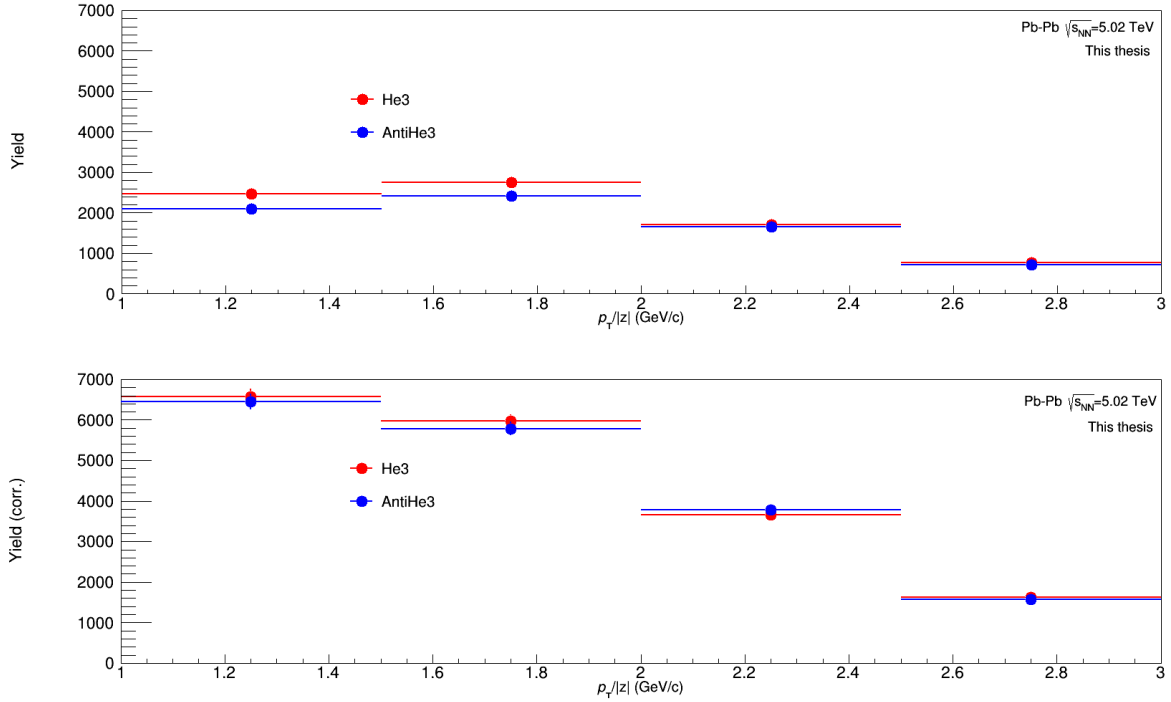

Figure 4.14: Uncorrected (top) and corrected (bottom) yield of ^{3}He and $^3\overline{\text{He}}$.

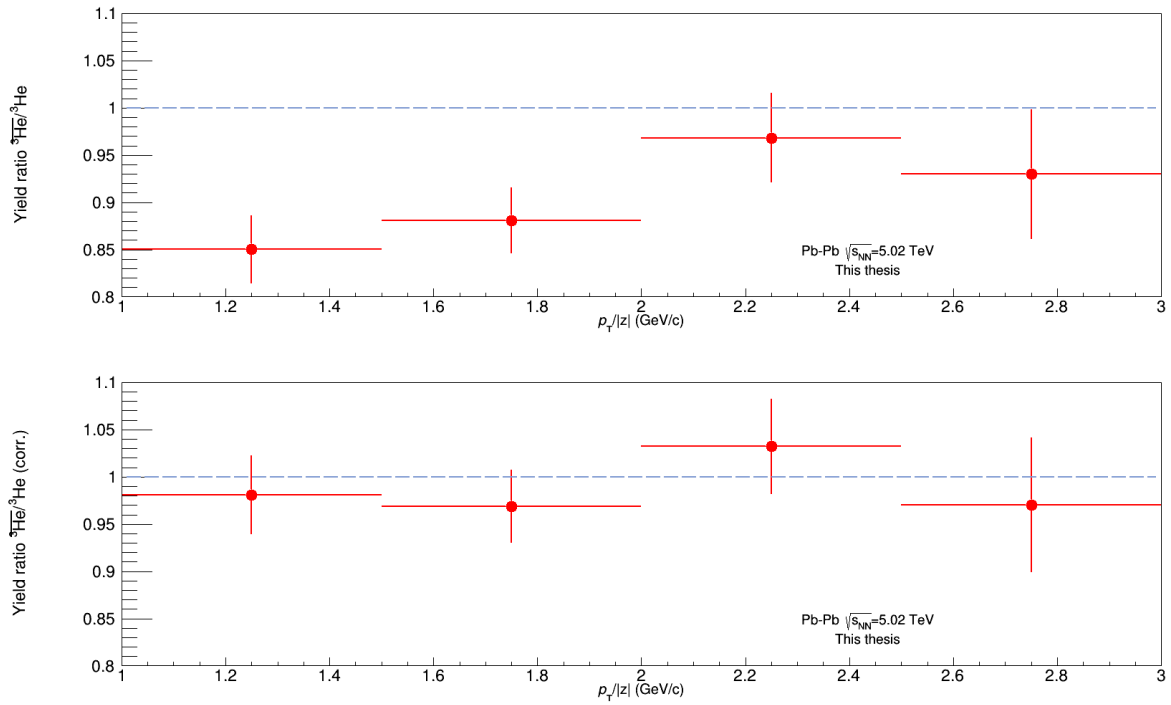

Figure 4.15: Uncorrected (top) and corrected (bottom) yield ratio of ^{3}He over $^3\overline{\text{He}}$ as a function of the transverse rigidity. The vertical bars represent the combined statistical uncertainties, assuming they are uncorrelated.

4.3 Comparison with previous measurements

The final results of this thesis are presented in this section. In order to compare them with the previous ones published in *Nature physics* in 2015 [22], the simple mass-over-charge ratio was calculated for each (anti-)nuclei as well as the difference which was fitted to extract the mean. The mass-over-charge ratio differences between the d and $\overline{\mathrm{d}}$ (Fig. 4.16), ^{3}He and $^3\overline{\mathrm{He}}$ (Fig. 4.17) nuclei as a function of the rigidity obtained in the previous analysis are presented on the top. The same measurements carried out here are presented on the bottom, but as a function of the transverse rigidity. One must take into account that the systematic errors are not included in this analysis which make the σ bands around the central value much wider in the case of the previous one, they are however assumed to be at the same order of magnitude because of the numerous similarities between between the studies. The final mass-over-charge ratio difference for each (anti-)nuclei specie is $\Delta(m/|z|)_{\mathrm{d}\,\overline{\mathrm{d}}} = -2.2 \times 10^{-4} \pm 1.1 \times 10^{-4}$ GeV/c^2 and $\Delta(m/|z|)_{^3\mathrm{He}\,^3\overline{\mathrm{He}}} = -2.0 \times 10^{-3} \pm 1.5 \times 10^{-4}$ GeV/c^2. Both results are compatible with zero within their uncertainties.

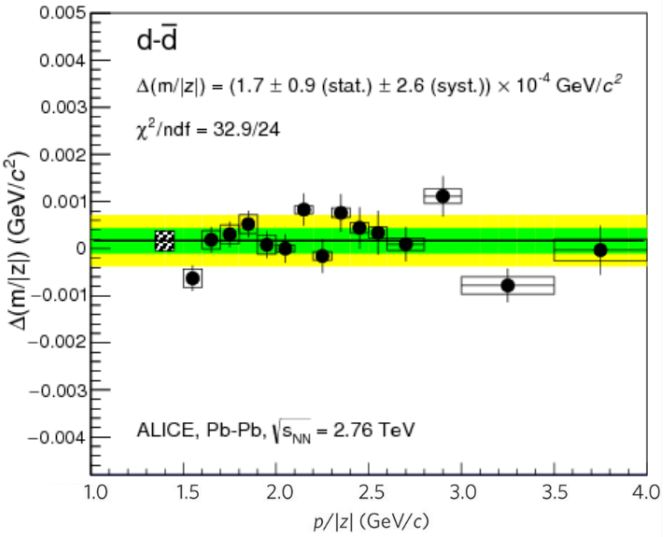

(a) Mass-over-charge ratio difference between the deuteron and anti-deuteron as a function of the particle rigidity, measured with Run 1 data at a center-of-mass energy per nucleon pair of 2.76 TeV*. Vertical bars and open boxes show the statistical and the uncorrelated systematic uncertainties respectively. The correlated systematic uncertainty is shown as a box with tilted lines. The* 1σ *and* 2σ *bands around the central value are also presented, where sigma is the sum in quadrature of the statistical and systematic uncertainties [22].*

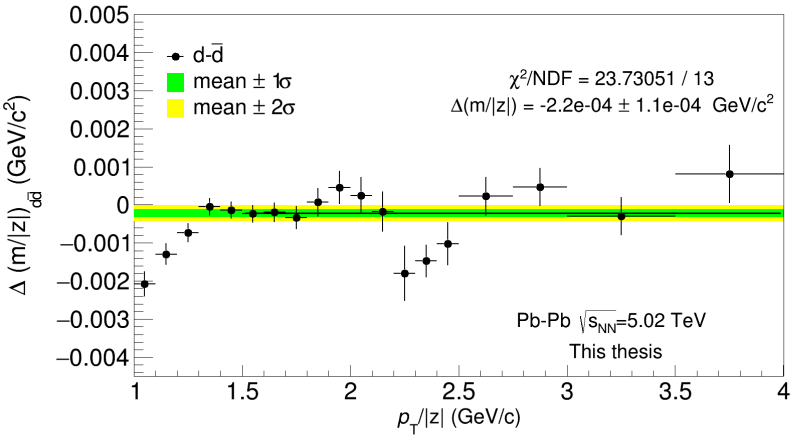

(b) Mass-over-charge ratio difference between the deuteron and anti-deuteron, measured in this analysis as a function of the particle transverse rigidity. Vertical bars show the statistical uncertainties. The 1σ *and* 2σ *bands around the central value are also presented, where sigma is the fit uncertainty. The first three data points are not included in the fit since they come from a systematic deviation.*

Figure 4.16: Comparison between the mass-over-charge ratio difference between the deuteron and anti-deuteron obtained with Run 1 data at 2.76 TeV and Run 2 data at 5.02 TeV.

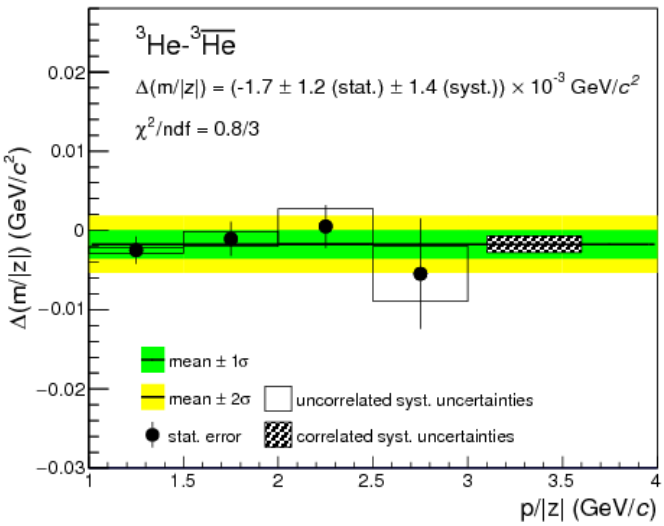

(a) Mass-over-charge ratio difference between the ^{3}He *and* $^3\overline{\text{He}}$ *as a function of the particle rigidity, measured with Run 1 data at a center-of-mass energy per nucleon pair of* 2.76 TeV*. Vertical bars and open boxes show the statistical and the uncorrelated systematic uncertainties respectively. The correlated systematic uncertainty is shown as a box with tilted lines. The* 1σ *and* 2σ *bands around the central value are also presented, where sigma is the sum in quadrature of the statistical and systematic uncertainties [22].*

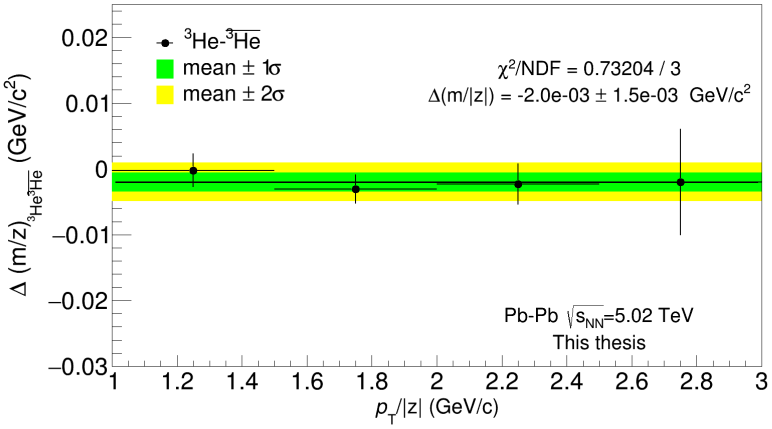

(b) Mass-over-charge ratio difference between ^{3}He *and* $^3\overline{\text{He}}$*, measured in this analysis as a function of the particle transverse rigidity. Vertical bars show the statistical uncertainties. The* 1σ *and* 2σ *bands around the central value are also presented, where sigma is the sum in quadrature of the statistical and systematic uncertainties.*

Figure 4.17: Comparison between the mass-over-charge ratio difference between the ^{3}He and $^3\overline{\text{He}}$ obtained with Run 1 data at 2.76 TeV and Run 2 data at 5.02 TeV.

Chapter 5

Conclusion

This thesis probes CPT invariance for particles bound by the strong force inside light nuclei by measuring the mass-over-charge ratio difference between the d and $\overline{\mathrm{d}}$, $^3\overline{\mathrm{He}}$ and ^{3}He nuclei. The results are in agreement with the previous published results [22] and are most certainly compatible with zero within their uncertainties if one includes the (yet to be estimated) systematic uncertainties.

It is the starting point of a full nuclei analysis and therefore highlights the implications and difficulties of Run 2 data such as the considerable background coming from TOF mismatches. In further nuclei studies this background could be reduced by incorporating TRD information during track reconstruction. A difference between the true and the reconstructed momentum of the ($^3\overline{\mathrm{He}}$)^{3}He for $p_T/|z| < 1\,\mathrm{GeV/c}$ is also observed. This thesis also makes clear that a there is systematic effect on the mass difference between matter and anti-matter –independently of the particles' mass– which is correctable by using the (anti-)proton mass. This effect is suspected to depend on the pseudorapidity and magnetic field orientation. Another effect observed in this study is the asymptotic behavior of the absolute measured mass of particles, explained by the energy lost during their propagation in the detector and corrected by using the mass of simulated particles. For future measurements, however, it is considered to use the energy loss information registered during the track reconstruction of the particles in order to obtain a corrected mass from the very beginning. This analysis also has to be completed with a study on the systematic uncertainties which is performed by varying the track quality cuts applied during the selection of (anti-)nuclei, by changing the magnetic field orientation and by using different fitting procedures.

Finally, the results reported here confirm CPT invariance in systems bound by nuclear forces and are part of the most precise measurements of mass differences in the sector of nuclei.

Bibliography

[1] Dmitry Kazakov. The Higgs Boson is found: what is next? *Phys. Usp.*, 57(9):930–942, 2014. [Usp. Fiz. Nauk184,no.9,1004(2014)].

[2] C. S. Wu, E. Ambler, R. W. Hayward, D. D. Hoppes, and R. P. Hudson. Experimental Test of Parity Conservation in Beta Decay. *Phys. Rev.*, 105:1413–1414, 1957.

[3] J. H. Christenson, J. W. Cronin, V. L. Fitch, and R. Turlay. Evidence for the 2π Decay of the K_2^0 Meson. *Phys. Rev. Lett.*, 13:138–140, 1964.

[4] J. P. Lees et al. Observation of Time Reversal Violation in the B^0 Meson System. *Phys. Rev. Lett.*, 109:211801, 2012.

[5] J. C. Yoon. CPT symmetry and the equality of mass and lifetime. 2005.

[6] K. A. Olive et al. Review of Particle Physics. *Chin. Phys.*, C38:090001, 2014.

[7] A. K. Chaudhuri. *A short course on Relativistic Heavy Ion Collisions*. IOPP, 2014.

[8] P. Rosnet. Quark-Gluon Plasma: from accelerator experiments to early Universe. In *11th Rencontres du Vietnam: Cosmology: 50 years after CMB discovery Quy Nhon, Vietnam, August 16-22, 2015*, 2015.

[9] Ramona Vogt. *Ultrarelativistic heavy-ion collisions*. Elsevier, Amsterdam, 2007.

[10] A. Andronic, P. Braun-Munzinger, J. Stachel, and H. Stocker. Production of light nuclei, hypernuclei and their antiparticles in relativistic nuclear collisions. *Phys. Lett.*, B697:203–207, 2011.

[11] J. Stachel, A. Andronic, P. Braun-Munzinger, and K. Redlich. Confronting LHC data with the statistical hadronization model. *J. Phys. Conf. Ser.*, 509:012019, 2014.

[12] Rudiger Scheibl and Ulrich W. Heinz. Coalescence and flow in ultrarelativistic heavy ion collisions. *Phys. Rev.*, C59:1585–1602, 1999.

[13] Cern webpage. `http://home.cern`.

[14] The ALICE Collaboration. The alice experiment at the cern lhc. *Journal of Instrumentation*, 3(08):S08002, 2008.

[15] Betty Bezverkhny Abelev et al. Performance of the ALICE Experiment at the CERN LHC. *Int. J. Mod. Phys.*, A29:1430044, 2014.

[16] J. Alme et al. The ALICE TPC, a large 3-dimensional tracking device with fast readout for ultra-high multiplicity events. *Nucl. Instrum. Meth.*, A622:316–367, 2010.

[17] The alice time projection chamber (tpc). `http://aliceinfo.cern.ch/Public/en/Chapter2/Chap2_TPC.html`.

[18] R. Schicker. Overview of ALICE results in pp, pA and AA collisions. *EPJ Web Conf.*, 138:01021, 2017.

[19] Alice offline. `https://alice-offline.web.cern.ch/Activities/Reconstruction/index.html#ReconstructionFramework`.

[20] M. Colocci. Precision measurement of deuteron and anti-deuteron and ^{3}He and $^3\overline{\mathrm{He}}$ mass-to-charge ratio difference with the ALICE experiment at the LHC. *ALICE Analysis Note*, ALICE-ANA-2012-1897.

[21] M. Floris B. Guerzoni A. Kalweit L. Milano R. Preghenella J. Anielski, M. Chojnacki. Spectra Analysis, pp at $\sqrt{7\,\mathrm{TeV}}$, Pb–Pb at $\sqrt{2.76\,\mathrm{TeV}}$. *ALICE Analysis Note*, ALICE-ANA-2012-570.

[22] Jaroslav Adam et al. Precision measurement of the mass difference between light nuclei and anti-nuclei. *Nature Phys.*, 11(10):811–814, 2015.

Appendix A

(Anti-)Deuteron plots

This section contains all the fits used for the extraction of the squared mass-to-charge ratio and the yields of the d and $\overline{\text{d}}$. This has been done in a transverse momentum range $p_T = [1\,\text{GeV}, 3\,\text{GeV}]$ in steps of 200 MeV and $p_T = [3\,\text{GeV}, 4\,\text{GeV}]$ in steps of 500 MeV.

A.1 Deuteron fits

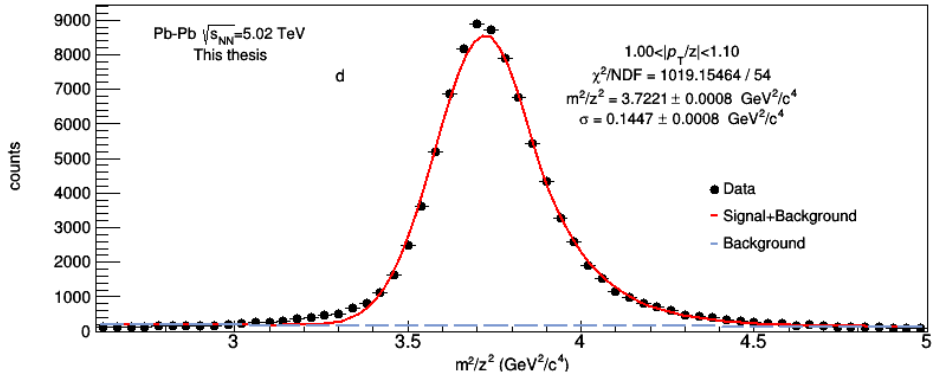

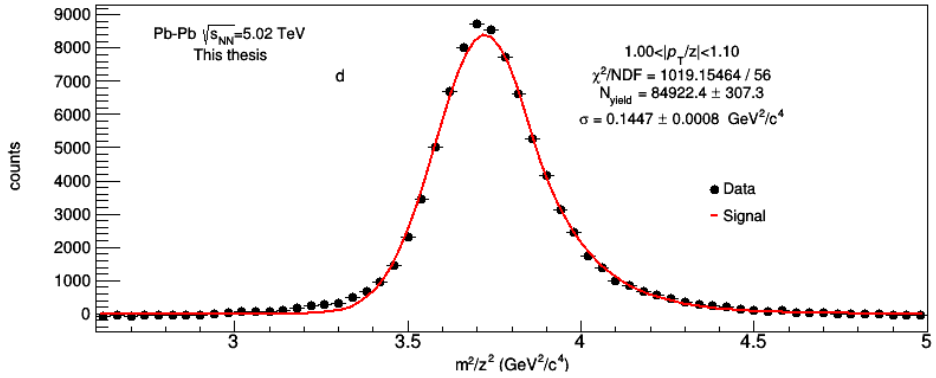

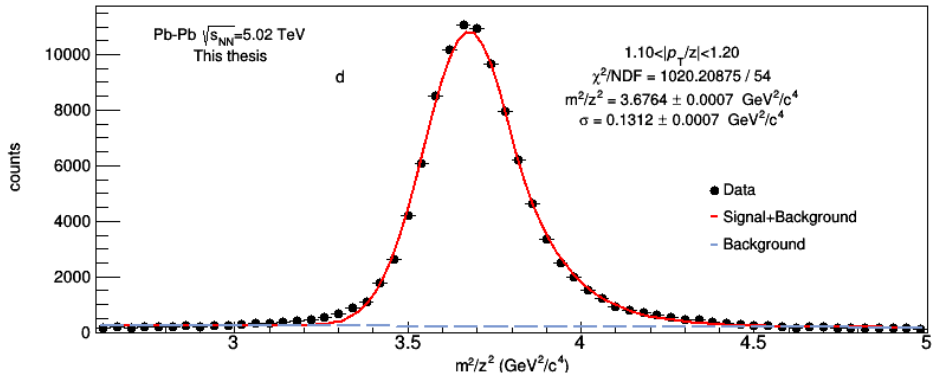
Pb-Pb $\sqrt{s_{NN}}$=5.02 TeV
This thesis
d
1.10<|p_T/z|<1.20
χ^2/NDF = 1020.20875 / 54
m^2/z^2 = 3.6764 ± 0.0007 GeV^2/c^4
σ = 0.1312 ± 0.0007 GeV^2/c^4
Data
Signal+Background
Background
counts
m^2/z^2 (GeV^2/c^4)

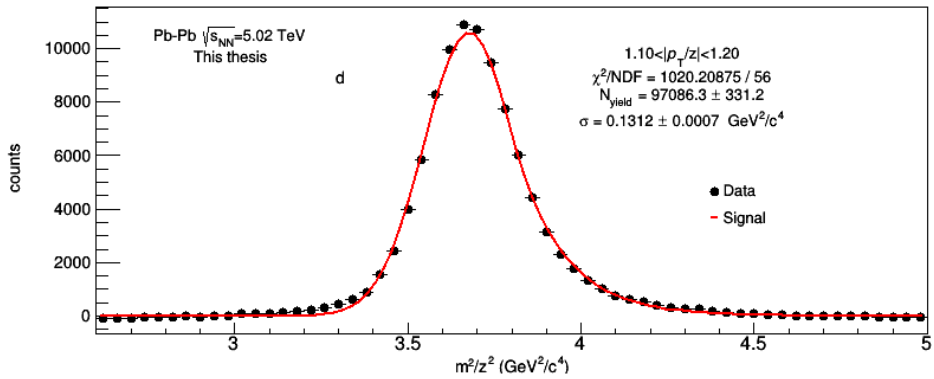
Pb-Pb $\sqrt{s_{NN}}$=5.02 TeV
This thesis
d
1.10<|p_T/z|<1.20
χ^2/NDF = 1020.20875 / 56
N_{yield} = 97086.3 ± 331.2
σ = 0.1312 ± 0.0007 GeV^2/c^4
Data
Signal
counts
m^2/z^2 (GeV^2/c^4)

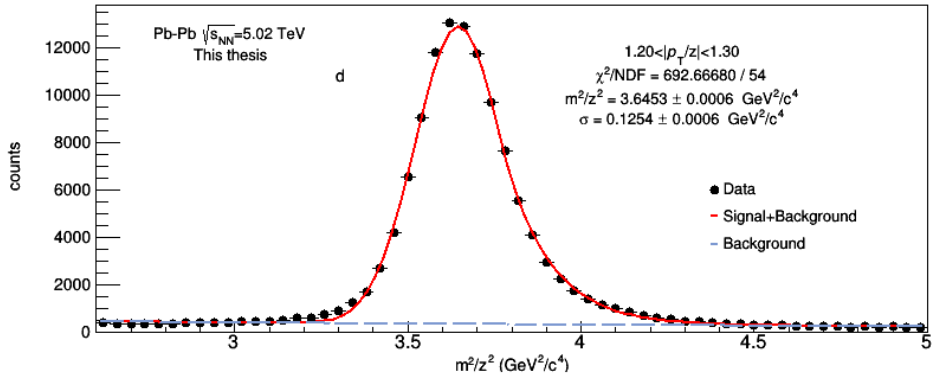
Pb-Pb $\sqrt{s_{NN}}$=5.02 TeV
This thesis
d
1.20<|p_T/z|<1.30
χ^2/NDF = 692.66680 / 54
m^2/z^2 = 3.6453 ± 0.0006 GeV^2/c^4
σ = 0.1254 ± 0.0006 GeV^2/c^4
Data
Signal+Background
Background
counts
m^2/z^2 (GeV^2/c^4)

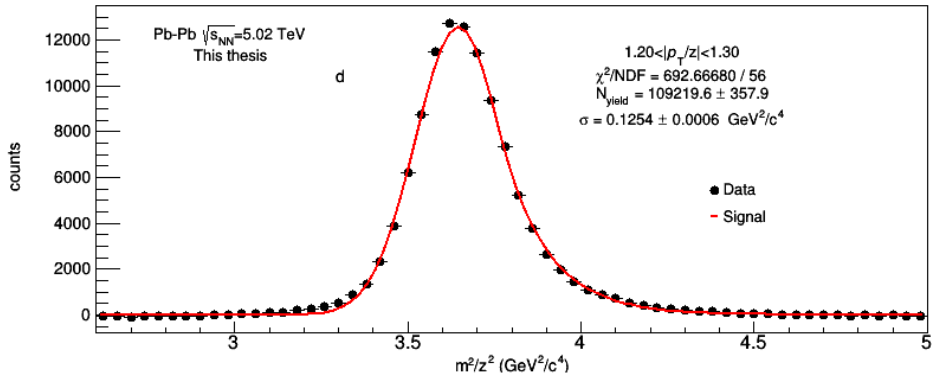
Pb-Pb $\sqrt{s_{NN}}$=5.02 TeV
This thesis
d
1.20<|p_T/z|<1.30
χ^2/NDF = 692.66680 / 56
N_{yield} = 109219.6 ± 357.9
σ = 0.1254 ± 0.0006 GeV^2/c^4
Data
Signal
counts
m^2/z^2 (GeV^2/c^4)

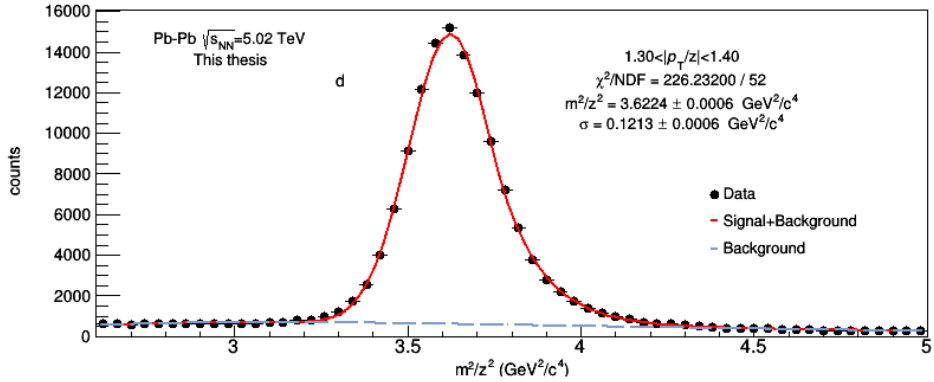
Pb-Pb $\sqrt{s_{NN}}$=5.02 TeV
This thesis
d
1.30<|p_T/z|<1.40
χ^2/NDF = 226.23200 / 52
m^2/z^2 = 3.6224 ± 0.0006 GeV^2/c^4
σ = 0.1213 ± 0.0006 GeV^2/c^4
Data
Signal+Background
Background
counts
m^2/z^2 (GeV^2/c^4)

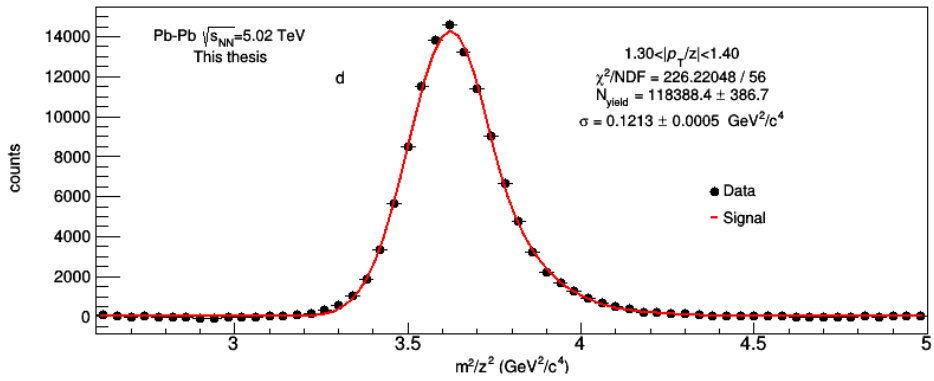
Pb-Pb $\sqrt{s_{NN}}$=5.02 TeV
This thesis
d
1.30<|p_T/z|<1.40
χ^2/NDF = 226.22048 / 56
N_{yield} = 118388.4 ± 386.7
σ = 0.1213 ± 0.0005 GeV^2/c^4
Data
Signal
counts
m^2/z^2 (GeV^2/c^4)

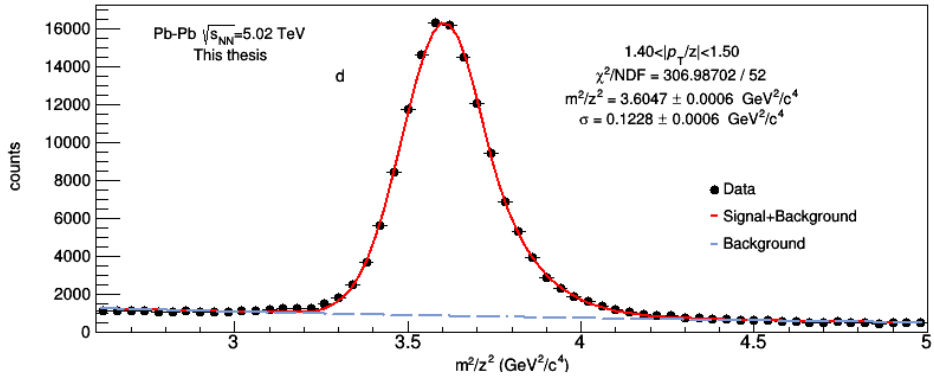
Pb-Pb $\sqrt{s_{NN}}$=5.02 TeV
This thesis
d
1.40<|p_T/z|<1.50
χ^2/NDF = 306.98702 / 52
m^2/z^2 = 3.6047 ± 0.0006 GeV^2/c^4
σ = 0.1228 ± 0.0006 GeV^2/c^4
Data
Signal+Background
Background
counts
m^2/z^2 (GeV^2/c^4)

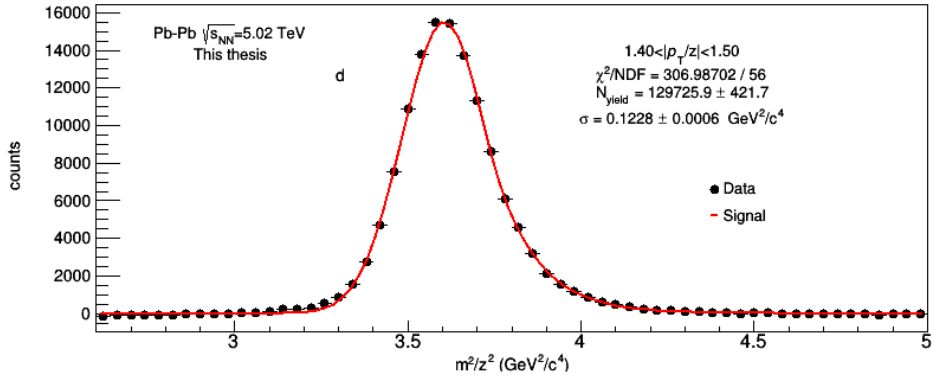
Pb-Pb $\sqrt{s_{NN}}$=5.02 TeV
This thesis
d
1.40<|p_T/z|<1.50
χ^2/NDF = 306.98702 / 56
N_{yield} = 129725.9 ± 421.7
σ = 0.1228 ± 0.0006 GeV^2/c^4
Data
Signal
counts
m^2/z^2 (GeV^2/c^4)

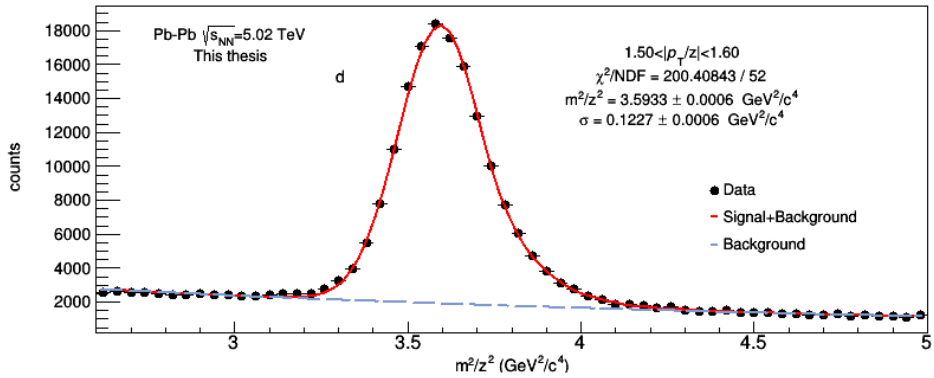
Pb-Pb $\sqrt{s_{NN}}$=5.02 TeV
This thesis
d
1.50<|p_T/z|<1.60
χ^2/NDF = 200.40843 / 52
m^2/z^2 = 3.5933 ± 0.0006 GeV^2/c^4
σ = 0.1227 ± 0.0006 GeV^2/c^4
Data
Signal+Background
Background
counts
m^2/z^2 (GeV^2/c^4)

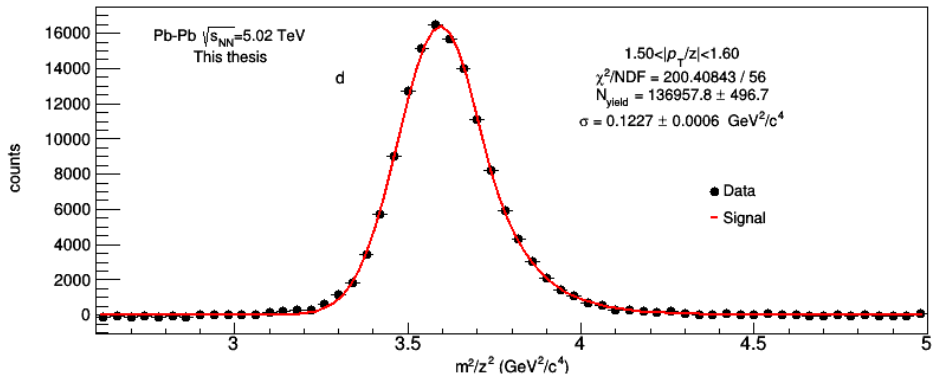
Pb-Pb $\sqrt{s_{NN}}$=5.02 TeV
This thesis
d
1.50<|p_T/z|<1.60
χ^2/NDF = 200.40843 / 56
N_{yield} = 136957.8 ± 496.7
σ = 0.1227 ± 0.0006 GeV^2/c^4
Data
Signal
counts
m^2/z^2 (GeV^2/c^4)

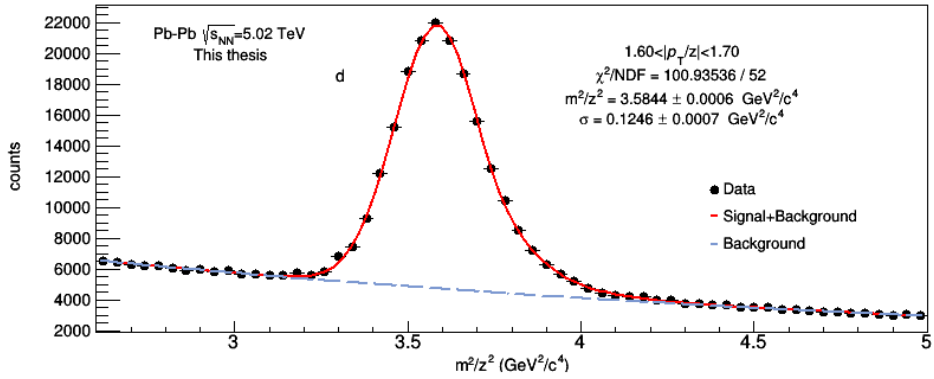
Pb-Pb $\sqrt{s_{NN}}$=5.02 TeV
This thesis
d
1.60<|p_T/z|<1.70
χ^2/NDF = 100.93536 / 52
m^2/z^2 = 3.5844 ± 0.0006 GeV^2/c^4
σ = 0.1246 ± 0.0007 GeV^2/c^4
Data
Signal+Background
Background
counts
m^2/z^2 (GeV^2/c^4)

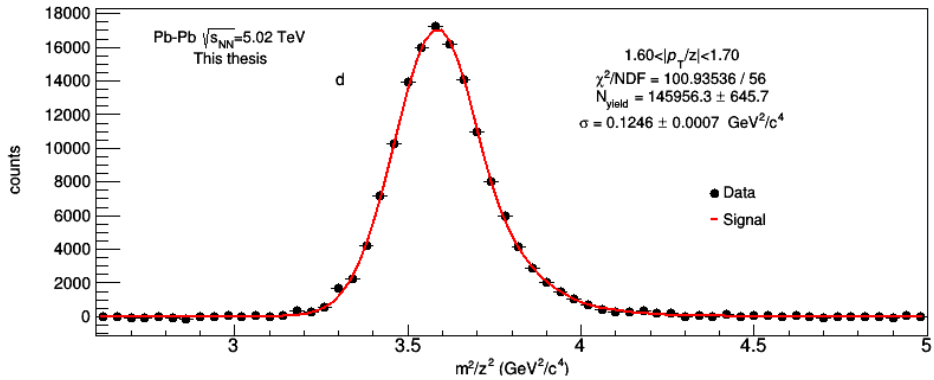
Pb-Pb $\sqrt{s_{NN}}$=5.02 TeV
This thesis
d
1.60<|p_T/z|<1.70
χ^2/NDF = 100.93536 / 56
N_{yield} = 145956.3 ± 645.7
σ = 0.1246 ± 0.0007 GeV^2/c^4
Data
Signal
counts
m^2/z^2 (GeV^2/c^4)

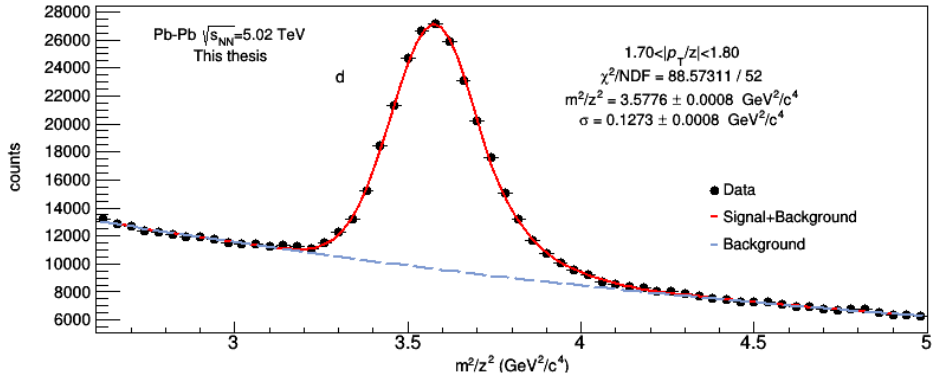
Pb-Pb $\sqrt{s_{NN}}$=5.02 TeV
This thesis
d
1.70<|p_T/z|<1.80
χ^2/NDF = 88.57311 / 52
m^2/z^2 = 3.5776 ± 0.0008 GeV^2/c^4
σ = 0.1273 ± 0.0008 GeV^2/c^4
Data
Signal+Background
Background
counts
m^2/z^2 (GeV^2/c^4)

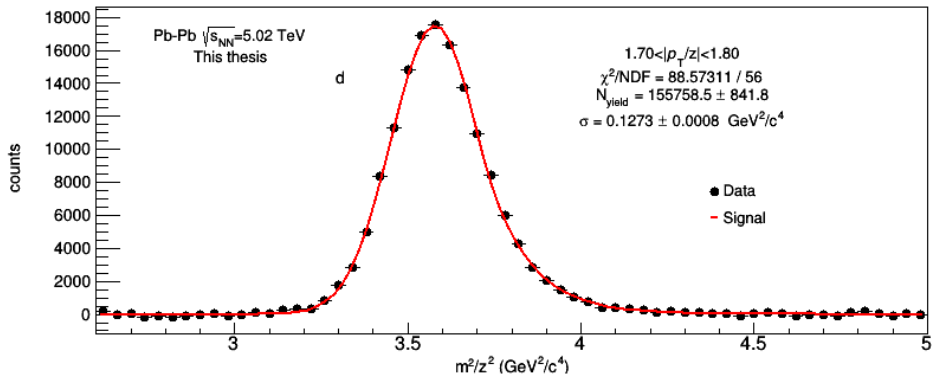
Pb-Pb $\sqrt{s_{NN}}$=5.02 TeV
This thesis
d
1.70<|p_T/z|<1.80
χ^2/NDF = 88.57311 / 56
N_{yield} = 155758.5 ± 841.8
σ = 0.1273 ± 0.0008 GeV^2/c^4
Data
Signal
counts
m^2/z^2 (GeV^2/c^4)

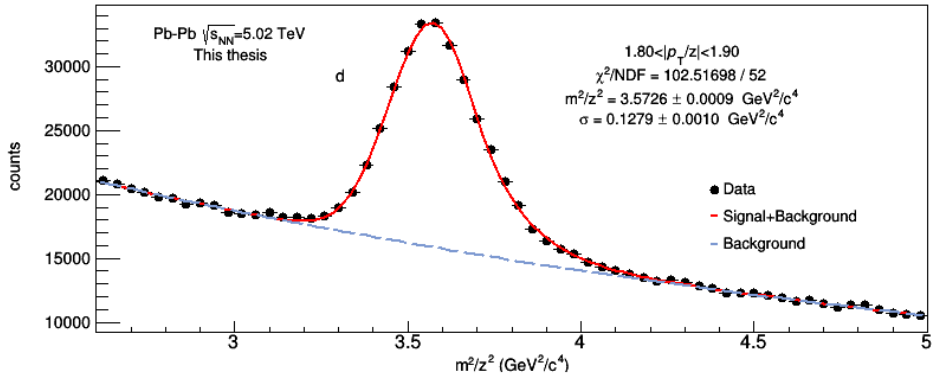
Pb-Pb $\sqrt{s_{NN}}$=5.02 TeV
This thesis
d
1.80<|p_T/z|<1.90
χ^2/NDF = 102.51698 / 52
m^2/z^2 = 3.5726 ± 0.0009 GeV^2/c^4
σ = 0.1279 ± 0.0010 GeV^2/c^4
Data
Signal+Background
Background
counts
m^2/z^2 (GeV^2/c^4)

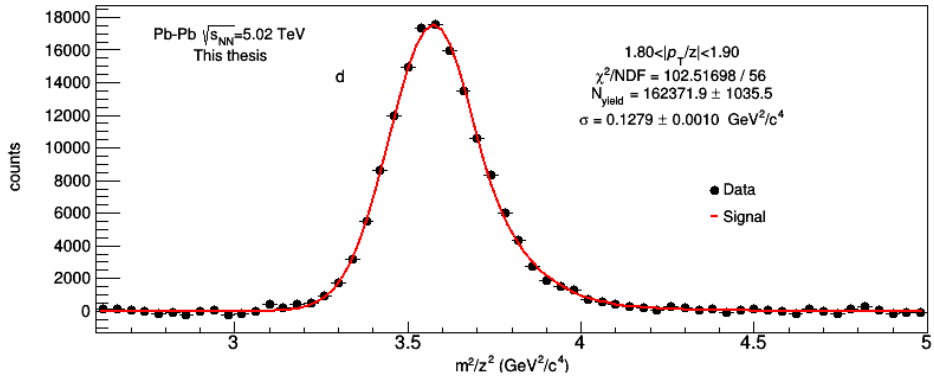
Pb-Pb $\sqrt{s_{NN}}$=5.02 TeV
This thesis
d
1.80<|p_T/z|<1.90
χ^2/NDF = 102.51698 / 56
N_{yield} = 162371.9 ± 1035.5
σ = 0.1279 ± 0.0010 GeV^2/c^4
Data
Signal
counts
m^2/z^2 (GeV^2/c^4)

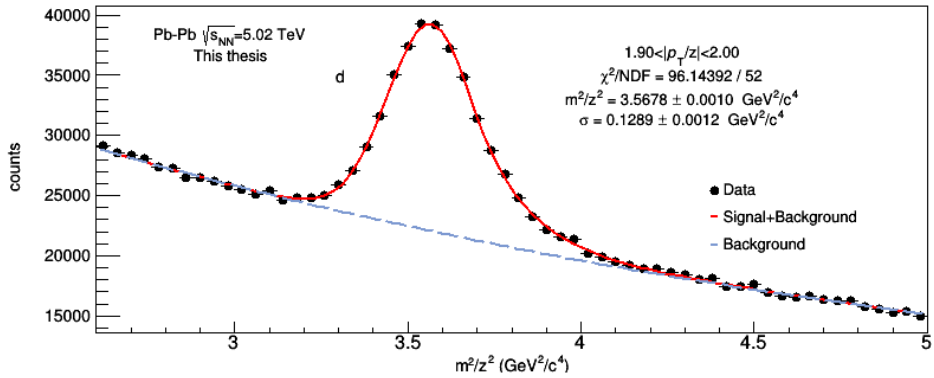
Pb-Pb $\sqrt{s_{NN}}$=5.02 TeV
This thesis
d
1.90<|p_T/z|<2.00
χ^2/NDF = 96.14392 / 52
m^2/z^2 = 3.5678 ± 0.0010 GeV^2/c^4
σ = 0.1289 ± 0.0012 GeV^2/c^4
Data
Signal+Background
Background
counts
m^2/z^2 (GeV^2/c^4)

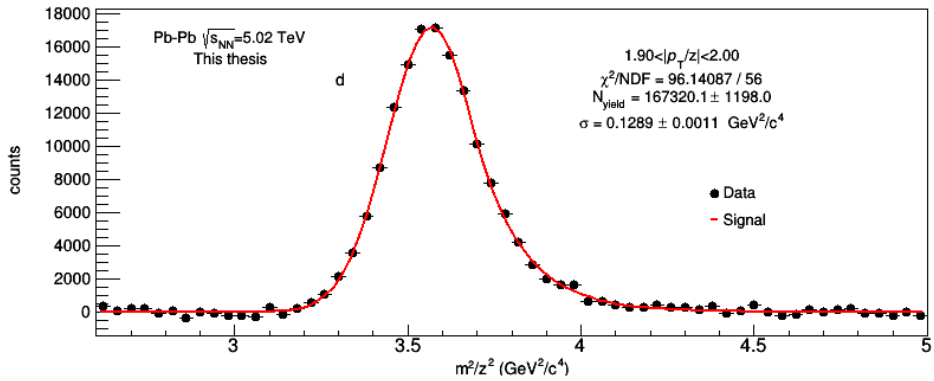
Pb-Pb $\sqrt{s_{NN}}$=5.02 TeV
This thesis
d
1.90<|p_T/z|<2.00
χ^2/NDF = 96.14087 / 56
N_{yield} = 167320.1 ± 1198.0
σ = 0.1289 ± 0.0011 GeV^2/c^4
Data
Signal
counts
m^2/z^2 (GeV^2/c^4)

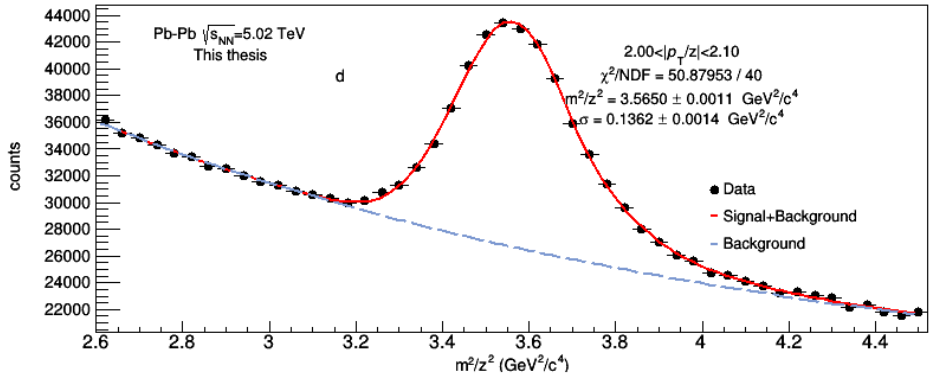
Pb-Pb $\sqrt{s_{NN}}$=5.02 TeV
This thesis
d
2.00<|p_T/z|<2.10
χ^2/NDF = 50.87953 / 40
m^2/z^2 = 3.5650 ± 0.0011 GeV^2/c^4
σ = 0.1362 ± 0.0014 GeV^2/c^4
Data
Signal+Background
Background
counts
m^2/z^2 (GeV^2/c^4)

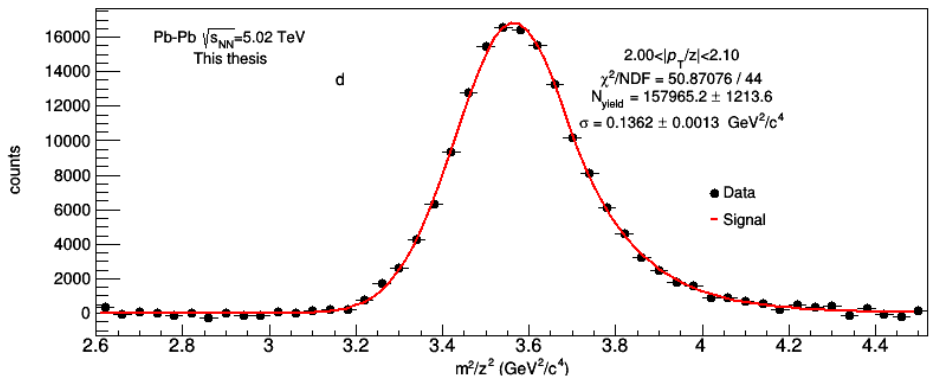
Pb-Pb $\sqrt{s_{NN}}$=5.02 TeV
This thesis
d
2.00<|p_T/z|<2.10
χ^2/NDF = 50.87076 / 44
N_{yield} = 157965.2 ± 1213.6
σ = 0.1362 ± 0.0013 GeV^2/c^4
Data
Signal
counts
m^2/z^2 (GeV^2/c^4)

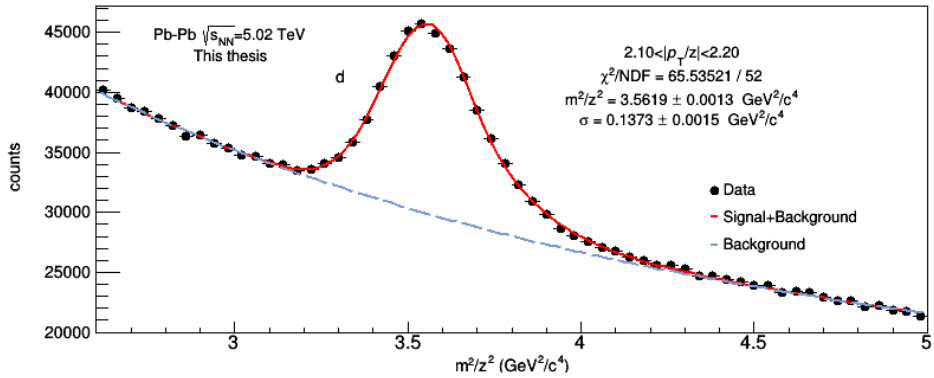
Pb-Pb $\sqrt{s_{NN}}$=5.02 TeV
This thesis
d
2.10<|p_T/z|<2.20
χ^2/NDF = 65.53521 / 52
m^2/z^2 = 3.5619 ± 0.0013 GeV^2/c^4
σ = 0.1373 ± 0.0015 GeV^2/c^4
Data
Signal+Background
Background
counts
m^2/z^2 (GeV^2/c^4)

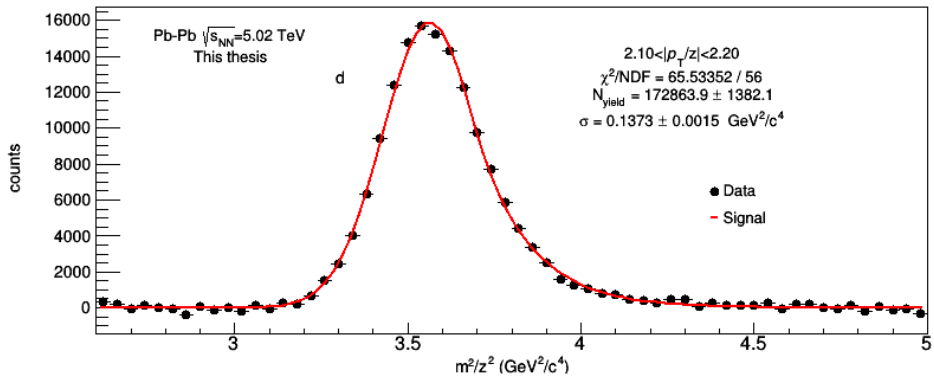
Pb-Pb $\sqrt{s_{NN}}$=5.02 TeV
This thesis
d
2.10<|p_T/z|<2.20
χ^2/NDF = 65.53352 / 56
N_{yield} = 172863.9 ± 1382.1
σ = 0.1373 ± 0.0015 GeV^2/c^4
Data
Signal
counts
m^2/z^2 (GeV^2/c^4)

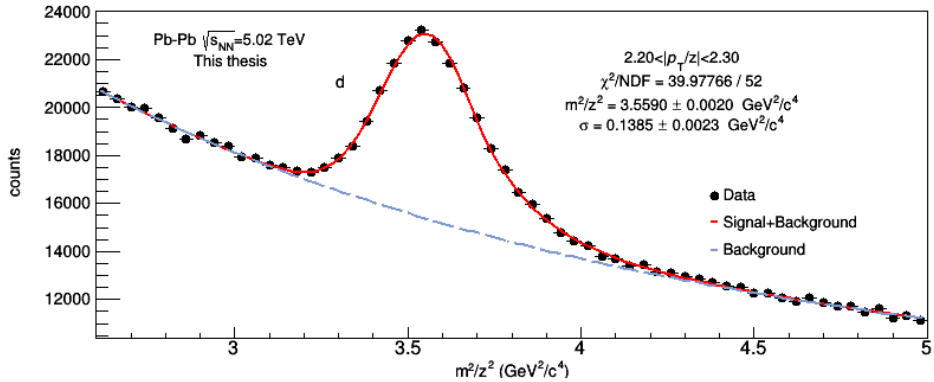
Pb-Pb $\sqrt{s_{NN}}$=5.02 TeV
This thesis
d
2.20<|p_T/z|<2.30
χ^2/NDF = 39.97766 / 52
m^2/z^2 = 3.5590 ± 0.0020 GeV^2/c^4
σ = 0.1385 ± 0.0023 GeV^2/c^4
Data
Signal+Background
Background
counts
m^2/z^2 (GeV^2/c^4)

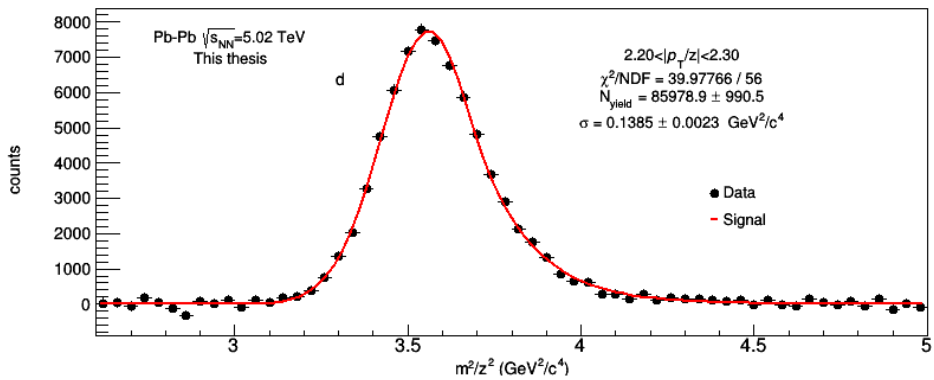
Pb-Pb $\sqrt{s_{NN}}$=5.02 TeV
This thesis
d
2.20<|p_T/z|<2.30
χ^2/NDF = 39.97766 / 56
N_{yield} = 85978.9 ± 990.5
σ = 0.1385 ± 0.0023 GeV^2/c^4
Data
Signal
counts
m^2/z^2 (GeV^2/c^4)

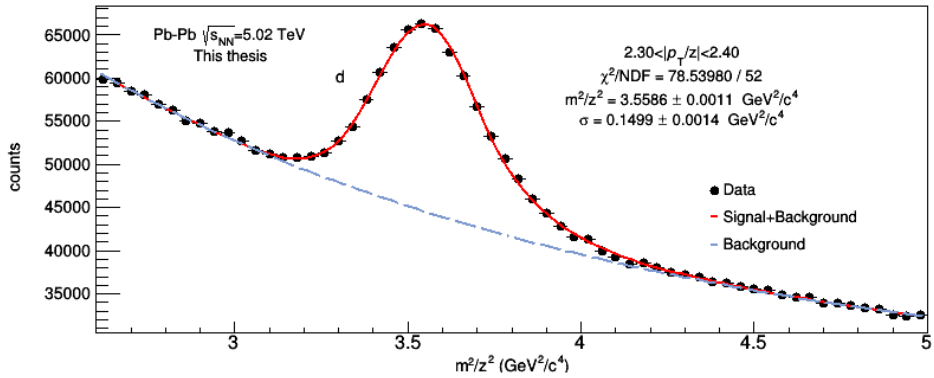
Pb-Pb $\sqrt{s_{NN}}$=5.02 TeV
This thesis
d
2.30<|p_T/z|<2.40
χ^2/NDF = 78.53980 / 52
m^2/z^2 = 3.5586 ± 0.0011 GeV^2/c^4
σ = 0.1499 ± 0.0014 GeV^2/c^4
Data
Signal+Background
Background
counts
m^2/z^2 (GeV^2/c^4)

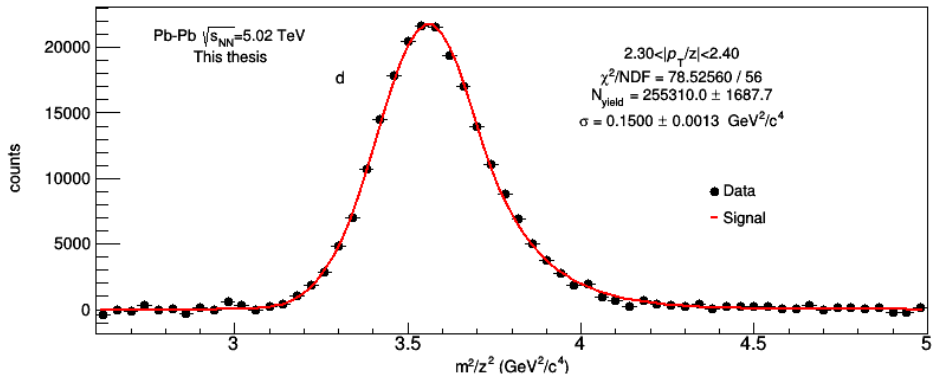
Pb-Pb $\sqrt{s_{NN}}$=5.02 TeV
This thesis
d
2.30<|p_T/z|<2.40
χ^2/NDF = 78.52560 / 56
N_{yield} = 255310.0 ± 1687.7
σ = 0.1500 ± 0.0013 GeV^2/c^4
Data
Signal
counts
m^2/z^2 (GeV^2/c^4)

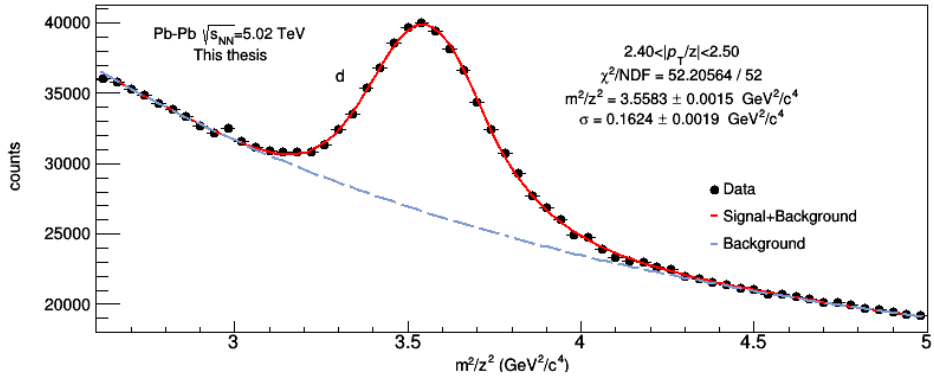
Pb-Pb $\sqrt{s_{NN}}$=5.02 TeV
This thesis
d
2.40<|p_T/z|<2.50
χ^2/NDF = 52.20564 / 52
m^2/z^2 = 3.5583 ± 0.0015 GeV^2/c^4
σ = 0.1624 ± 0.0019 GeV^2/c^4
Data
Signal+Background
Background
counts
m^2/z^2 (GeV^2/c^4)

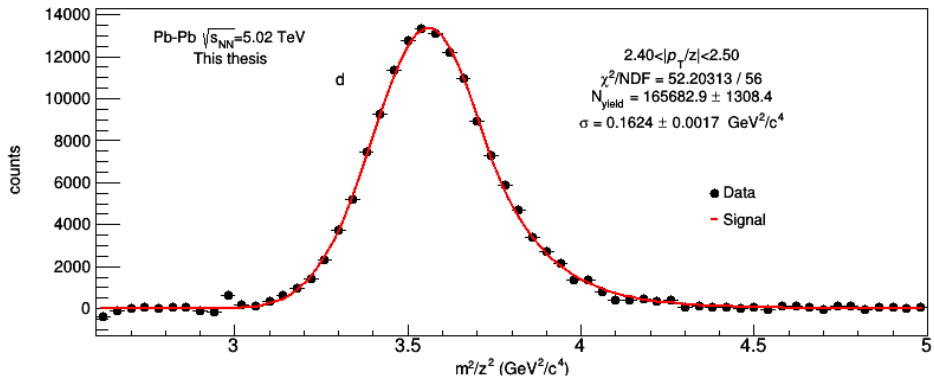
Pb-Pb $\sqrt{s_{NN}}$=5.02 TeV
This thesis
d
2.40<|p_T/z|<2.50
χ^2/NDF = 52.20313 / 56
N_{yield} = 165682.9 ± 1308.4
σ = 0.1624 ± 0.0017 GeV^2/c^4
Data
Signal
counts
m^2/z^2 (GeV^2/c^4)

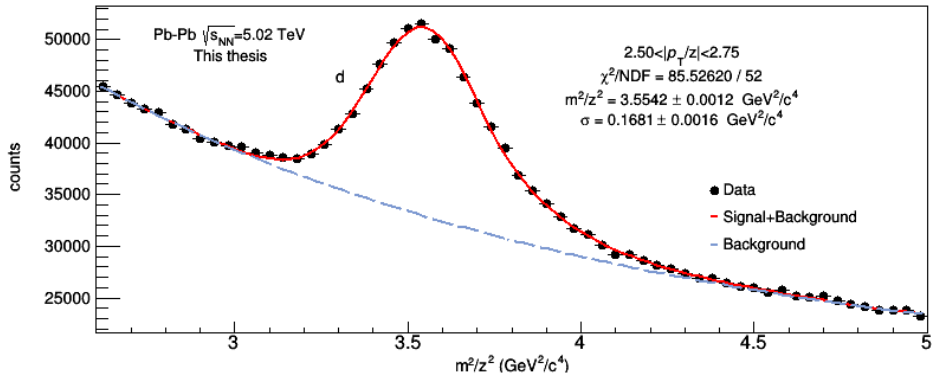
Pb-Pb $\sqrt{s_{NN}}$=5.02 TeV
This thesis
d
2.50<|p_T/z|<2.75
χ^2/NDF = 85.52620 / 52
m^2/z^2 = 3.5542 ± 0.0012 GeV^2/c^4
σ = 0.1681 ± 0.0016 GeV^2/c^4
Data
Signal+Background
Background
counts
m^2/z^2 (GeV^2/c^4)

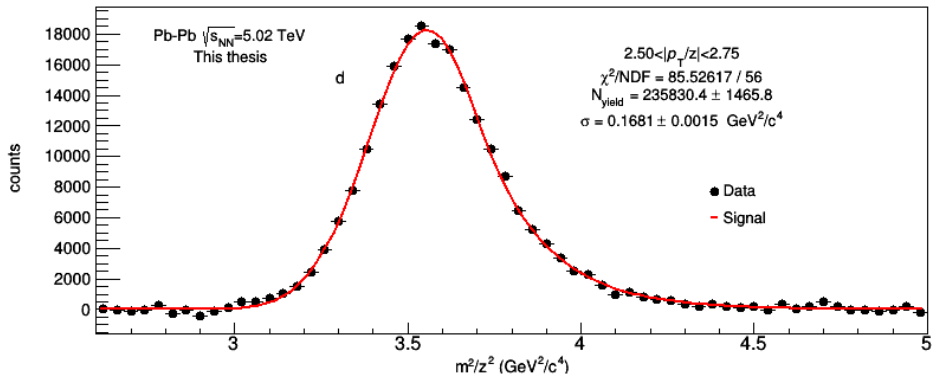
Pb-Pb $\sqrt{s_{NN}}$=5.02 TeV
This thesis
d
2.50<|p_T/z|<2.75
χ^2/NDF = 85.52617 / 56
N_{yield} = 235830.4 ± 1465.8
σ = 0.1681 ± 0.0015 GeV^2/c^4
Data
Signal
counts
m^2/z^2 (GeV^2/c^4)

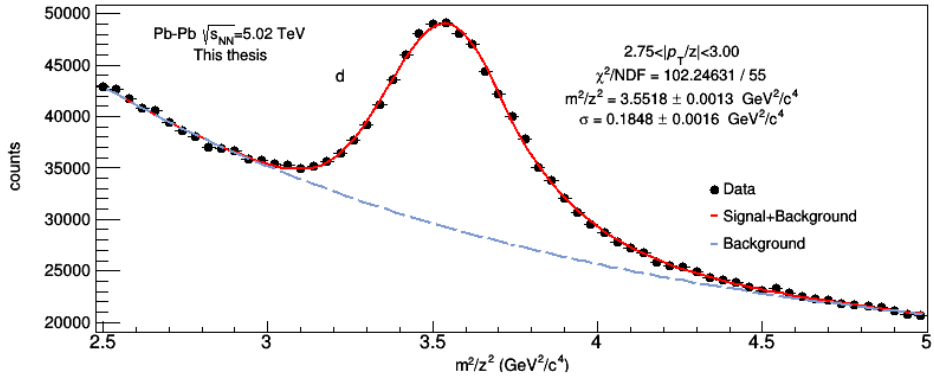
Pb-Pb $\sqrt{s_{NN}}$=5.02 TeV
This thesis
d
2.75<|p_T/z|<3.00
χ^2/NDF = 102.24631 / 55
m^2/z^2 = 3.5518 ± 0.0013 GeV^2/c^4
σ = 0.1848 ± 0.0016 GeV^2/c^4
Data
Signal+Background
Background
counts
m^2/z^2 (GeV^2/c^4)

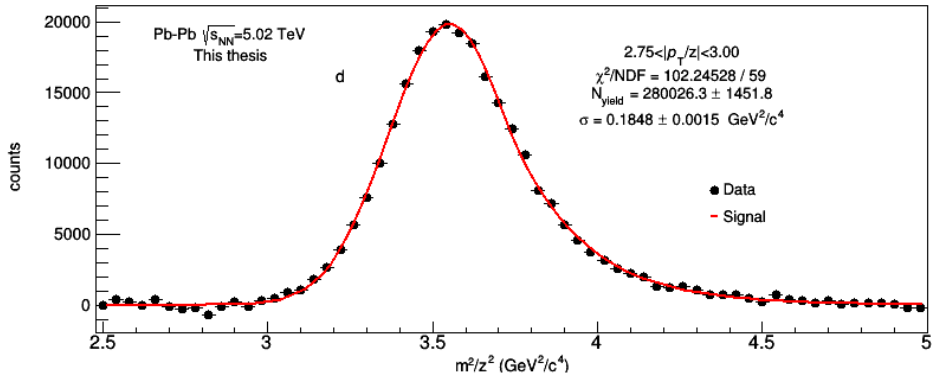
Pb-Pb $\sqrt{s_{NN}}$=5.02 TeV
This thesis
d
2.75<|p_T/z|<3.00
χ^2/NDF = 102.24528 / 59
N_{yield} = 280026.3 ± 1451.8
σ = 0.1848 ± 0.0015 GeV^2/c^4
Data
Signal
counts
m^2/z^2 (GeV^2/c^4)

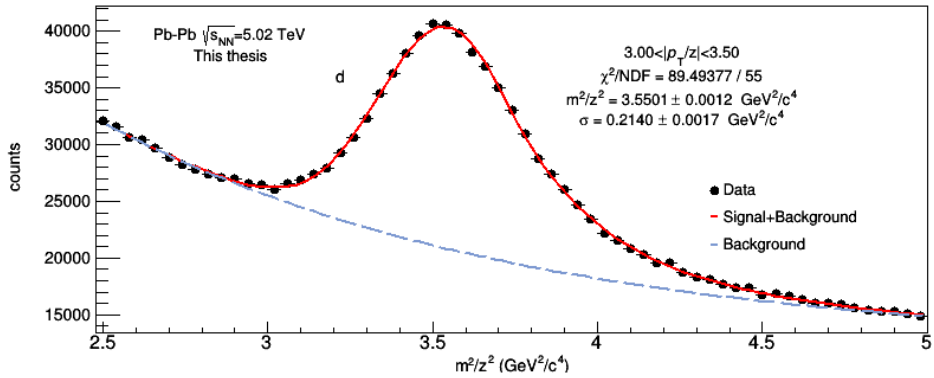
Pb-Pb $\sqrt{s_{NN}}$=5.02 TeV
This thesis
d
3.00<|p_T/z|<3.50
χ^2/NDF = 89.49377 / 55
m^2/z^2 = 3.5501 ± 0.0012 GeV^2/c^4
σ = 0.2140 ± 0.0017 GeV^2/c^4
Data
Signal+Background
Background
counts
m^2/z^2 (GeV^2/c^4)

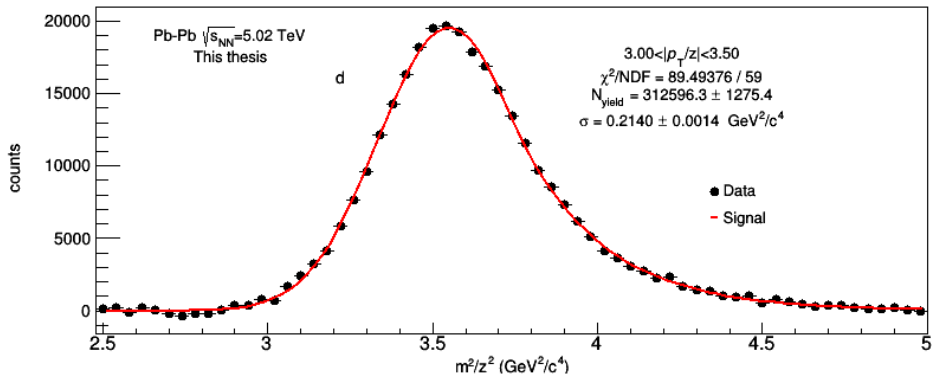
Pb-Pb $\sqrt{s_{NN}}$=5.02 TeV
This thesis
d
3.00<|p_T/z|<3.50
χ^2/NDF = 89.49376 / 59
N_{yield} = 312596.3 ± 1275.4
σ = 0.2140 ± 0.0014 GeV^2/c^4
Data
Signal
counts
m^2/z^2 (GeV^2/c^4)

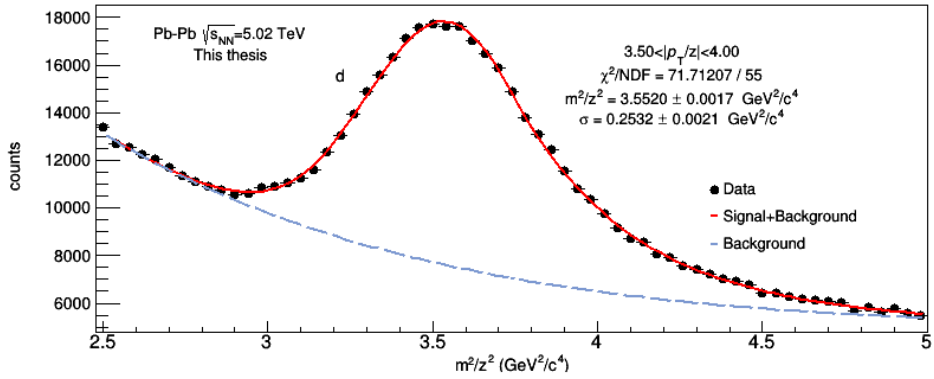
Pb-Pb $\sqrt{s_{NN}}$=5.02 TeV
This thesis
d
3.50<|p_T/z|<4.00
χ^2/NDF = 71.71207 / 55
m^2/z^2 = 3.5520 ± 0.0017 GeV^2/c^4
σ = 0.2532 ± 0.0021 GeV^2/c^4
Data
Signal+Background
Background
counts
m^2/z^2 (GeV^2/c^4)

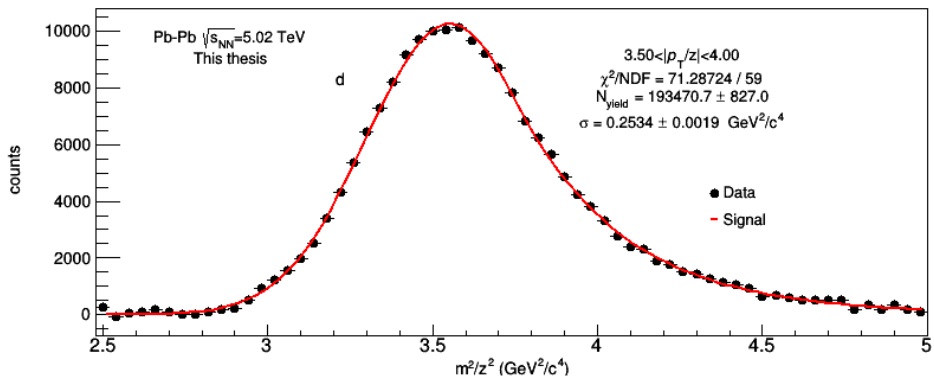
Pb-Pb $\sqrt{s_{NN}}$=5.02 TeV
This thesis
d
3.50<|p_T/z|<4.00
χ^2/NDF = 71.28724 / 59
N_{yield} = 193470.7 ± 827.0
σ = 0.2534 ± 0.0019 GeV^2/c^4
Data
Signal
counts
m^2/z^2 (GeV^2/c^4)

A.2 Anti-Deuteron fits

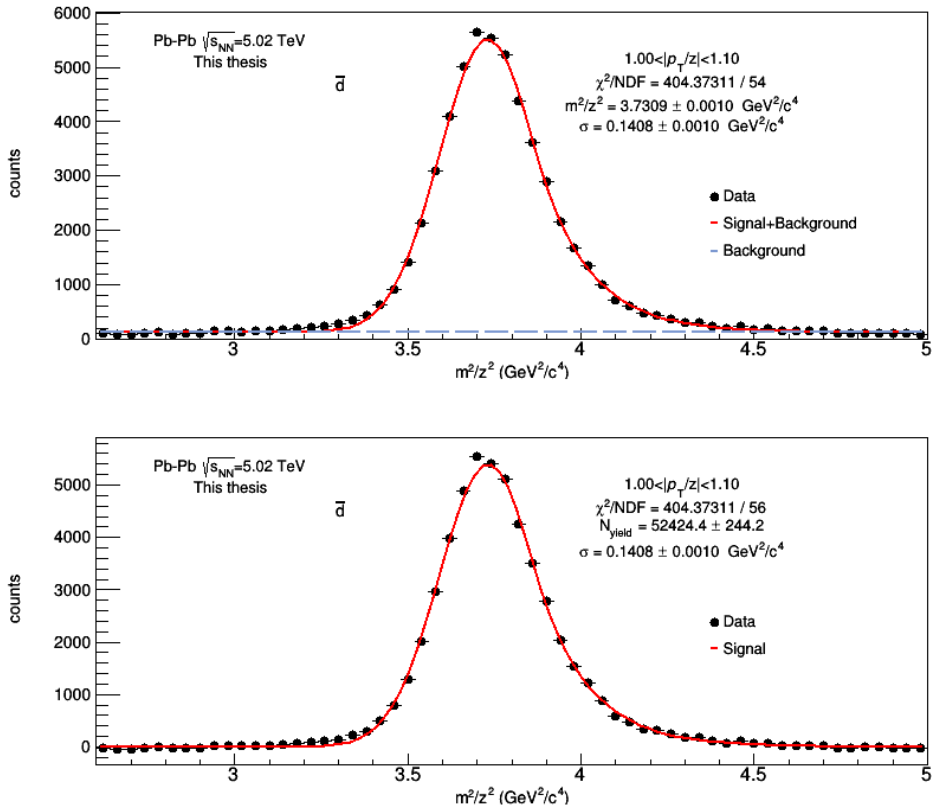

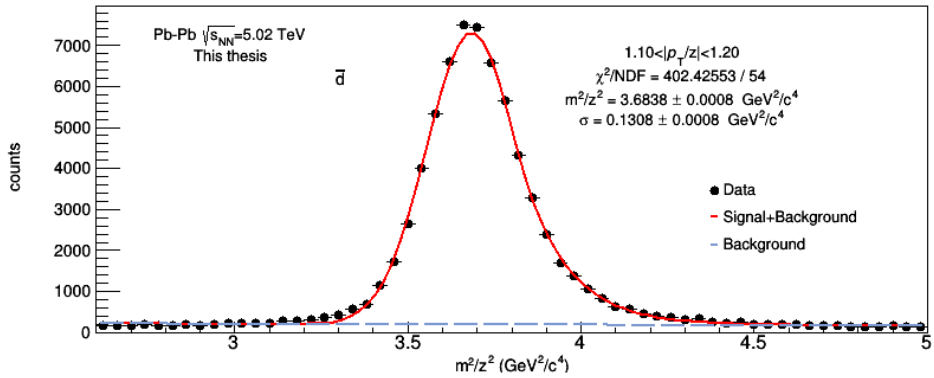
Pb-Pb $\sqrt{s_{NN}}$=5.02 TeV
This thesis
$\bar{d}$
1.10<|p_T/z|<1.20
χ^2/NDF = 402.42553 / 54
m^2/z^2 = 3.6838 ± 0.0008 GeV^2/c^4
σ = 0.1308 ± 0.0008 GeV^2/c^4
Data
Signal+Background
Background
counts
m^2/z^2 (GeV^2/c^4)

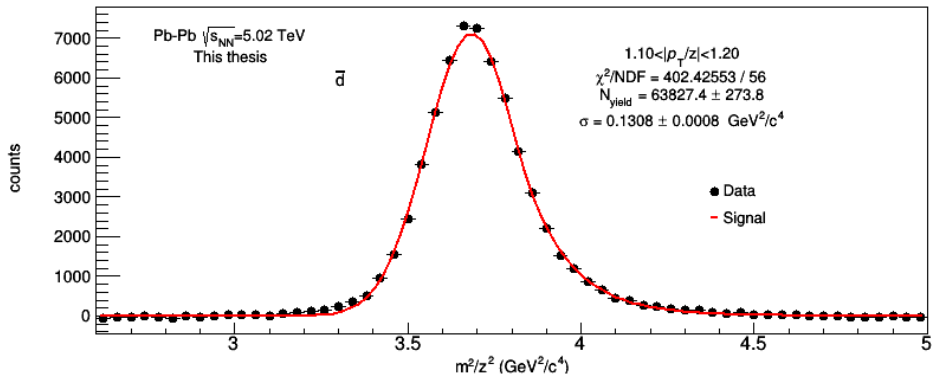
Pb-Pb $\sqrt{s_{NN}}$=5.02 TeV
This thesis
$\bar{d}$
1.10<|p_T/z|<1.20
χ^2/NDF = 402.42553 / 56
N_{yield} = 63827.4 ± 273.8
σ = 0.1308 ± 0.0008 GeV^2/c^4
Data
Signal
counts
m^2/z^2 (GeV^2/c^4)

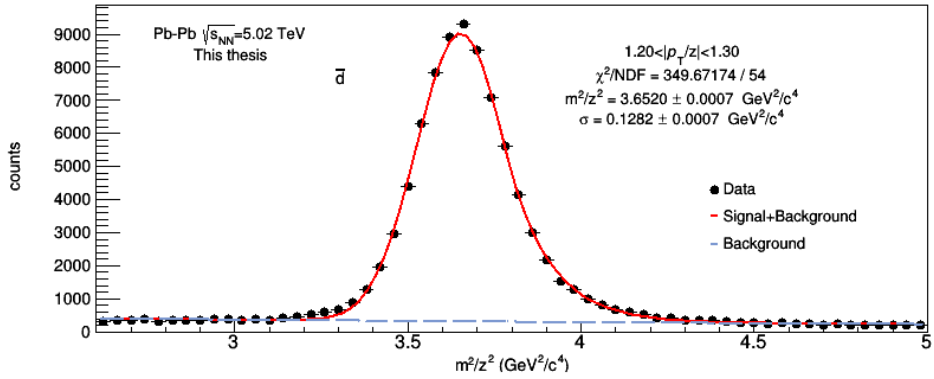
Pb-Pb $\sqrt{s_{NN}}$=5.02 TeV
This thesis
$\bar{d}$
1.20<|p_T/z|<1.30
χ^2/NDF = 349.67174 / 54
m^2/z^2 = 3.6520 ± 0.0007 GeV^2/c^4
σ = 0.1282 ± 0.0007 GeV^2/c^4
Data
Signal+Background
Background
counts
m^2/z^2 (GeV^2/c^4)

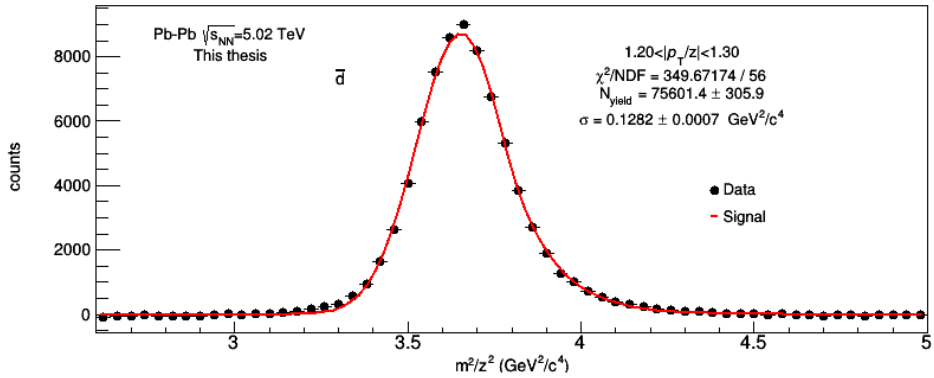
Pb-Pb $\sqrt{s_{NN}}$=5.02 TeV
This thesis
$\bar{d}$
1.20<|p_T/z|<1.30
χ^2/NDF = 349.67174 / 56
N_{yield} = 75601.4 ± 305.9
σ = 0.1282 ± 0.0007 GeV^2/c^4
Data
Signal
counts
m^2/z^2 (GeV^2/c^4)

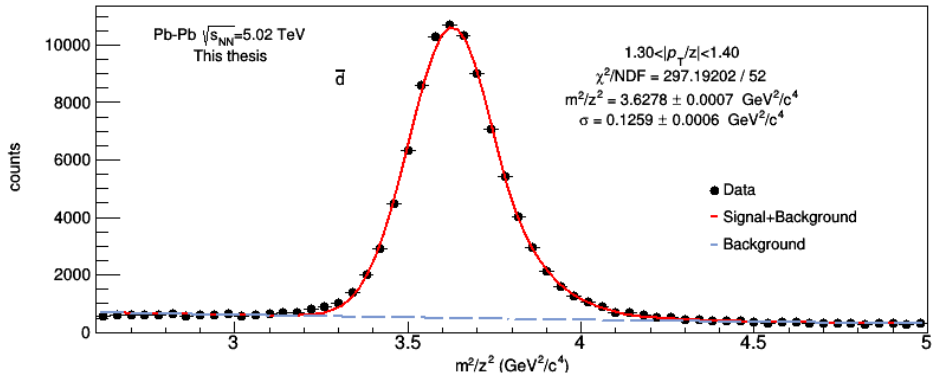
Pb-Pb $\sqrt{s_{NN}}$=5.02 TeV
This thesis
$\bar{d}$
1.30<|p_T/z|<1.40
χ^2/NDF = 297.19202 / 52
m^2/z^2 = 3.6278 ± 0.0007 GeV^2/c^4
σ = 0.1259 ± 0.0006 GeV^2/c^4
Data
Signal+Background
Background
counts
m^2/z^2 (GeV^2/c^4)

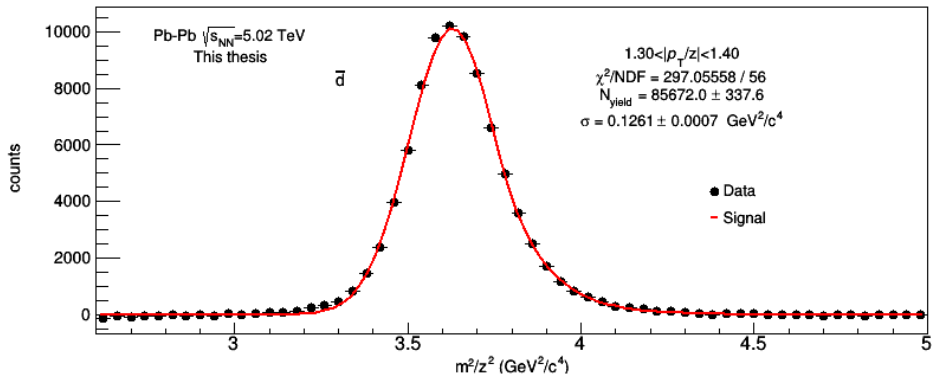
Pb-Pb $\sqrt{s_{NN}}$=5.02 TeV
This thesis
$\bar{d}$
1.30<|p_T/z|<1.40
χ^2/NDF = 297.05558 / 56
N_{yield} = 85672.0 ± 337.6
σ = 0.1261 ± 0.0007 GeV^2/c^4
Data
Signal
counts
m^2/z^2 (GeV^2/c^4)

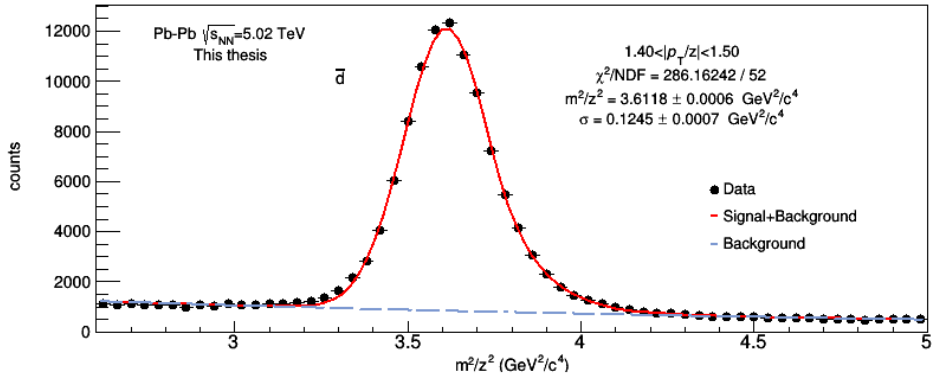
Pb-Pb $\sqrt{s_{NN}}$=5.02 TeV
This thesis
$\bar{d}$
1.40<|p_T/z|<1.50
χ^2/NDF = 286.16242 / 52
m^2/z^2 = 3.6118 ± 0.0006 GeV^2/c^4
σ = 0.1245 ± 0.0007 GeV^2/c^4
Data
Signal+Background
Background
counts
m^2/z^2 (GeV^2/c^4)

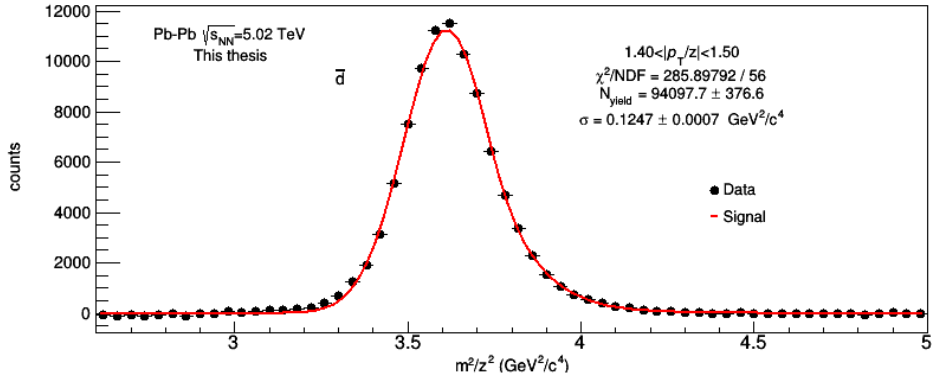
Pb-Pb $\sqrt{s_{NN}}$=5.02 TeV
This thesis
$\bar{d}$
1.40<|p_T/z|<1.50
χ^2/NDF = 285.89792 / 56
N_{yield} = 94097.7 ± 376.6
σ = 0.1247 ± 0.0007 GeV^2/c^4
Data
Signal
counts
m^2/z^2 (GeV^2/c^4)

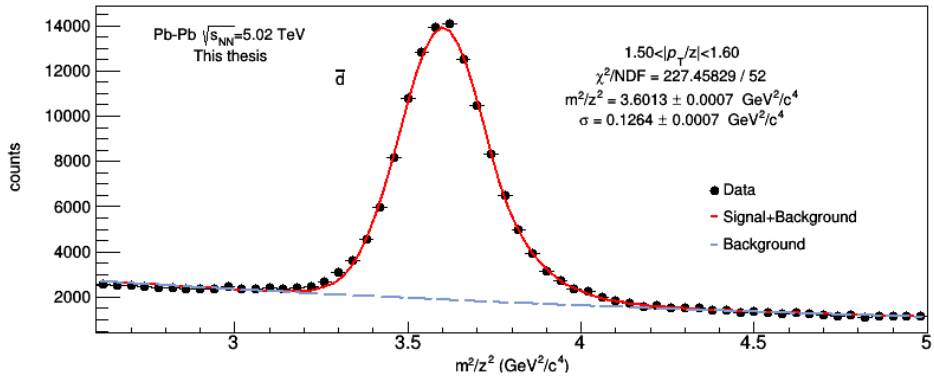
Pb-Pb $\sqrt{s_{NN}}$=5.02 TeV
This thesis
$\bar{d}$
1.50<|p_T/z|<1.60
χ^2/NDF = 227.45829 / 52
m^2/z^2 = 3.6013 ± 0.0007 GeV^2/c^4
σ = 0.1264 ± 0.0007 GeV^2/c^4
Data
Signal+Background
Background
counts
m^2/z^2 (GeV^2/c^4)

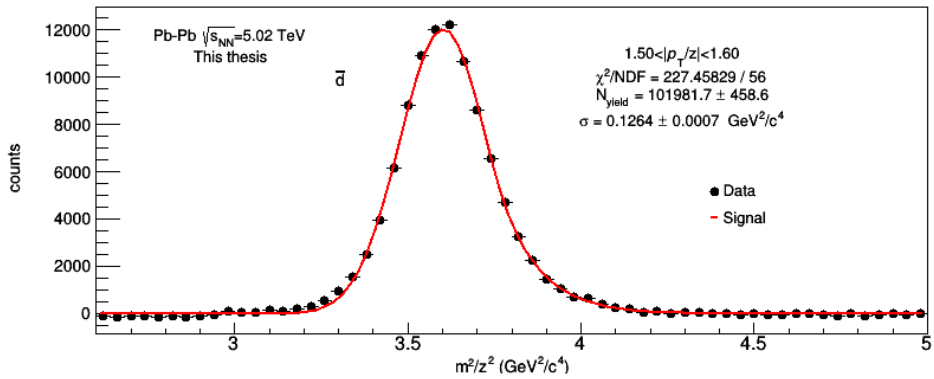
Pb-Pb $\sqrt{s_{NN}}$=5.02 TeV
This thesis
$\bar{d}$
1.50<|p_T/z|<1.60
χ^2/NDF = 227.45829 / 56
N_{yield} = 101981.7 ± 458.6
σ = 0.1264 ± 0.0007 GeV^2/c^4
Data
Signal
counts
m^2/z^2 (GeV^2/c^4)

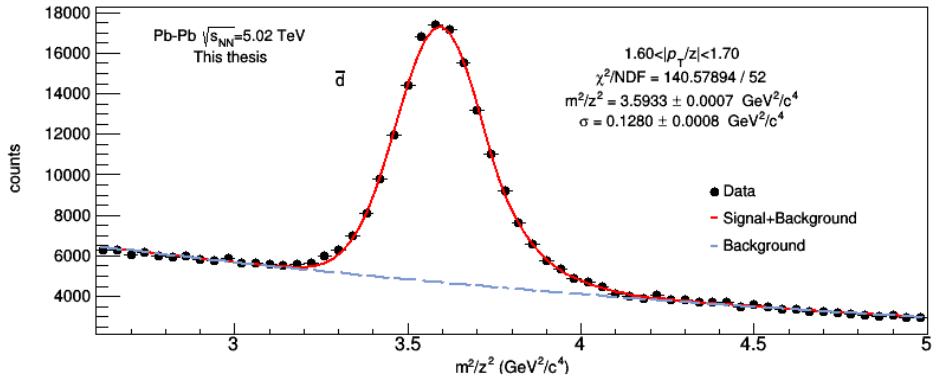
Pb-Pb $\sqrt{s_{NN}}$=5.02 TeV
This thesis
$\bar{d}$
1.60<|p_T/z|<1.70
χ^2/NDF = 140.57894 / 52
m^2/z^2 = 3.5933 ± 0.0007 GeV^2/c^4
σ = 0.1280 ± 0.0008 GeV^2/c^4
Data
Signal+Background
Background
counts
m^2/z^2 (GeV^2/c^4)

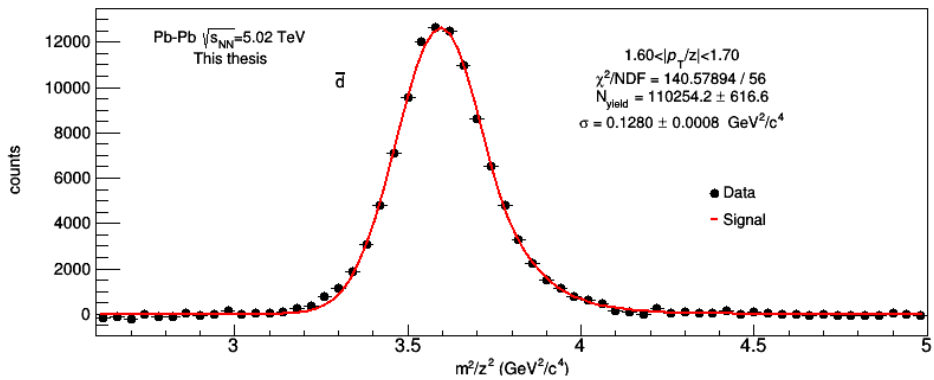
Pb-Pb $\sqrt{s_{NN}}$=5.02 TeV
This thesis
$\bar{d}$
1.60<|p_T/z|<1.70
χ^2/NDF = 140.57894 / 56
N_{yield} = 110254.2 ± 616.6
σ = 0.1280 ± 0.0008 GeV^2/c^4
Data
Signal
counts
m^2/z^2 (GeV^2/c^4)

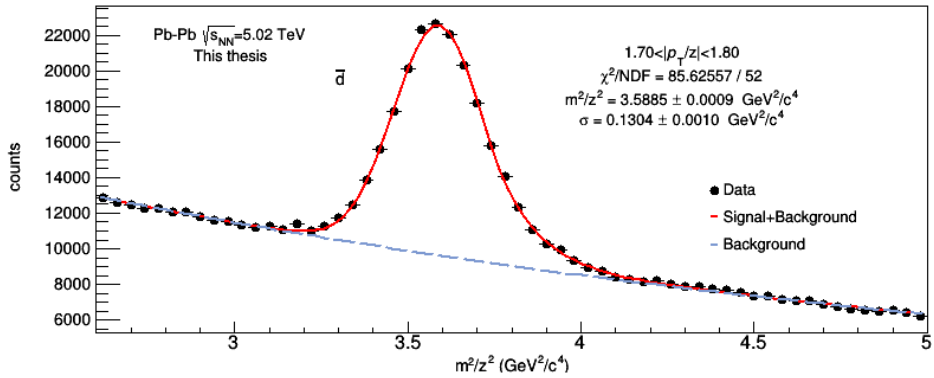
Pb-Pb $\sqrt{s_{NN}}$=5.02 TeV
This thesis
$\bar{d}$
1.70<|p_T/z|<1.80
χ^2/NDF = 85.62557 / 52
m^2/z^2 = 3.5885 ± 0.0009 GeV^2/c^4
σ = 0.1304 ± 0.0010 GeV^2/c^4
Data
Signal+Background
Background
counts
m^2/z^2 (GeV^2/c^4)

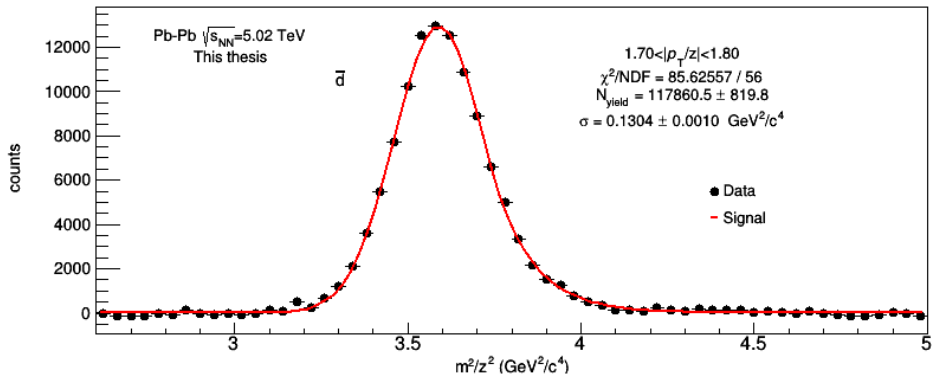
Pb-Pb $\sqrt{s_{NN}}$=5.02 TeV
This thesis
$\bar{d}$
1.70<|p_T/z|<1.80
χ^2/NDF = 85.62557 / 56
N_{yield} = 117860.5 ± 819.8
σ = 0.1304 ± 0.0010 GeV^2/c^4
Data
Signal
counts
m^2/z^2 (GeV^2/c^4)

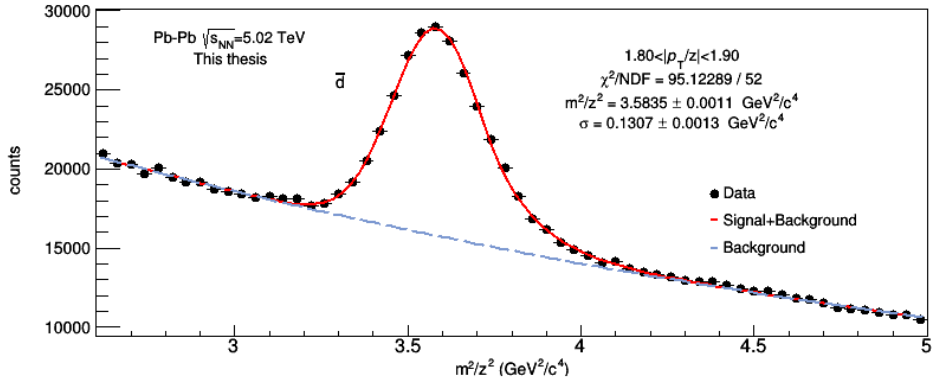
Pb-Pb $\sqrt{s_{NN}}$=5.02 TeV
This thesis
$\bar{d}$
1.80<|p_T/z|<1.90
χ^2/NDF = 95.12289 / 52
m^2/z^2 = 3.5835 ± 0.0011 GeV^2/c^4
σ = 0.1307 ± 0.0013 GeV^2/c^4
Data
Signal+Background
Background
counts
m^2/z^2 (GeV^2/c^4)

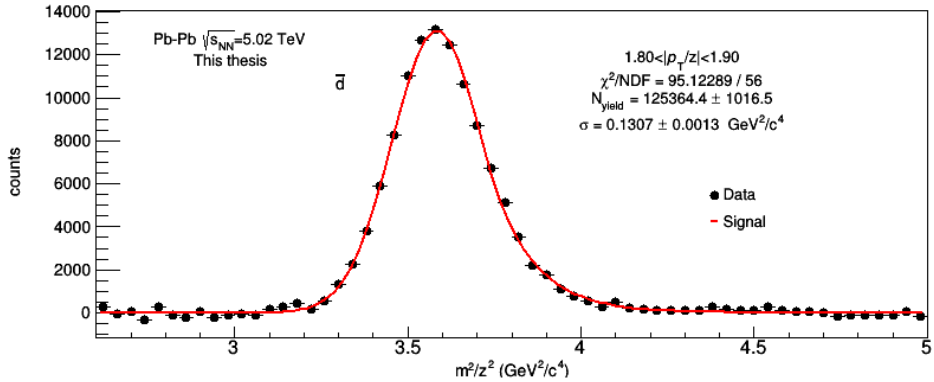
Pb-Pb $\sqrt{s_{NN}}$=5.02 TeV
This thesis
$\bar{d}$
1.80<|p_T/z|<1.90
χ^2/NDF = 95.12289 / 56
N_{yield} = 125364.4 ± 1016.5
σ = 0.1307 ± 0.0013 GeV^2/c^4
Data
Signal
counts
m^2/z^2 (GeV^2/c^4)

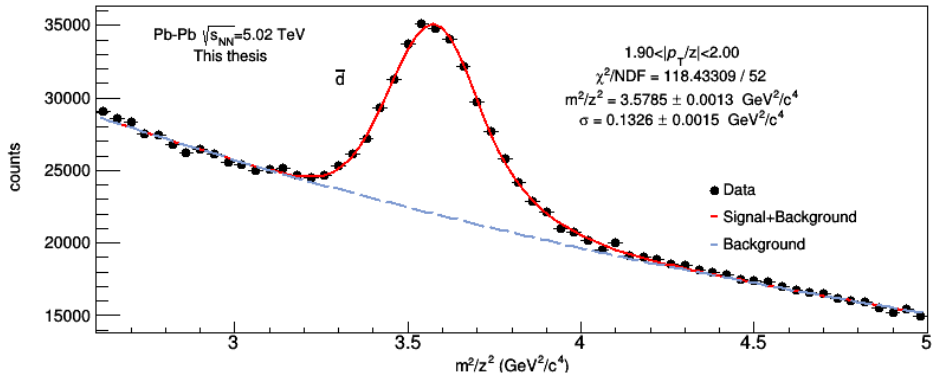
Pb-Pb $\sqrt{s_{NN}}$=5.02 TeV
This thesis
$\bar{d}$
1.90<|p_T/z|<2.00
χ^2/NDF = 118.43309 / 52
m^2/z^2 = 3.5785 ± 0.0013 GeV^2/c^4
σ = 0.1326 ± 0.0015 GeV^2/c^4
Data
Signal+Background
Background
counts
m^2/z^2 (GeV^2/c^4)

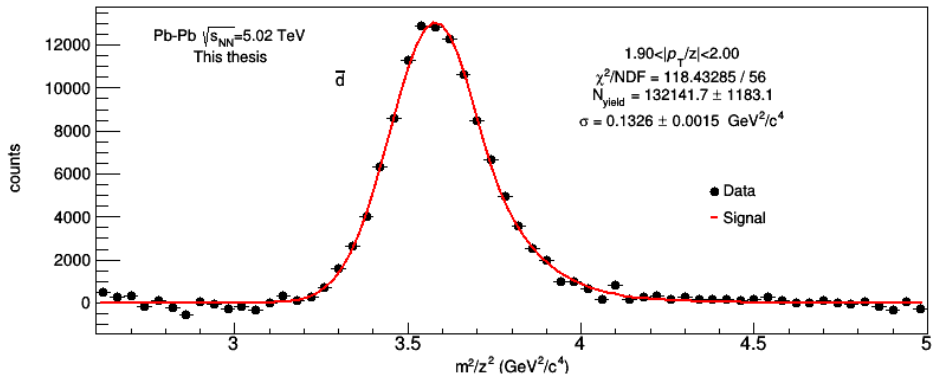
Pb-Pb $\sqrt{s_{NN}}$=5.02 TeV
This thesis
$\bar{d}$
1.90<|p_T/z|<2.00
χ^2/NDF = 118.43285 / 56
N_{yield} = 132141.7 ± 1183.1
σ = 0.1326 ± 0.0015 GeV^2/c^4
Data
Signal
counts
m^2/z^2 (GeV^2/c^4)

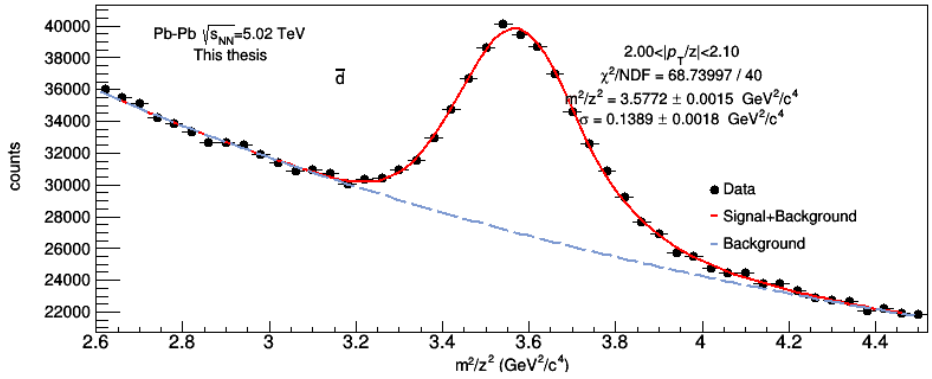
Pb-Pb $\sqrt{s_{NN}}$=5.02 TeV
This thesis
$\bar{d}$
2.00<|p_T/z|<2.10
χ^2/NDF = 68.73997 / 40
m^2/z^2 = 3.5772 ± 0.0015 GeV^2/c^4
σ = 0.1389 ± 0.0018 GeV^2/c^4
Data
Signal+Background
Background
counts
m^2/z^2 (GeV^2/c^4)

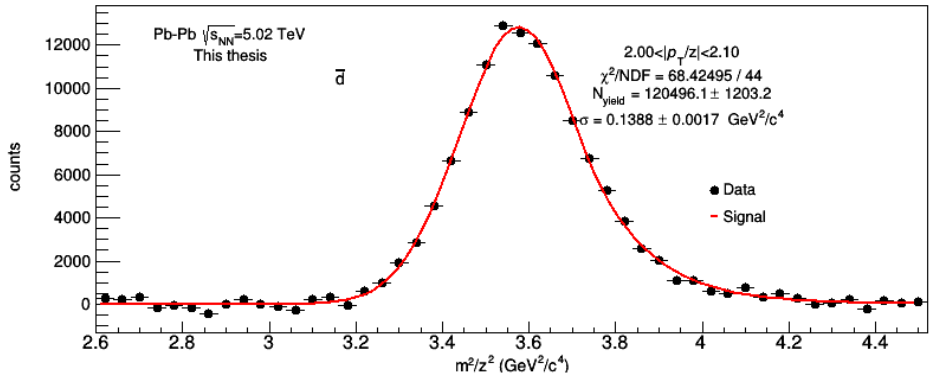
Pb-Pb $\sqrt{s_{NN}}$=5.02 TeV
This thesis
$\bar{d}$
2.00<|p_T/z|<2.10
χ^2/NDF = 68.42495 / 44
N_{yield} = 120496.1 ± 1203.2
σ = 0.1388 ± 0.0017 GeV^2/c^4
Data
Signal
counts
m^2/z^2 (GeV^2/c^4)

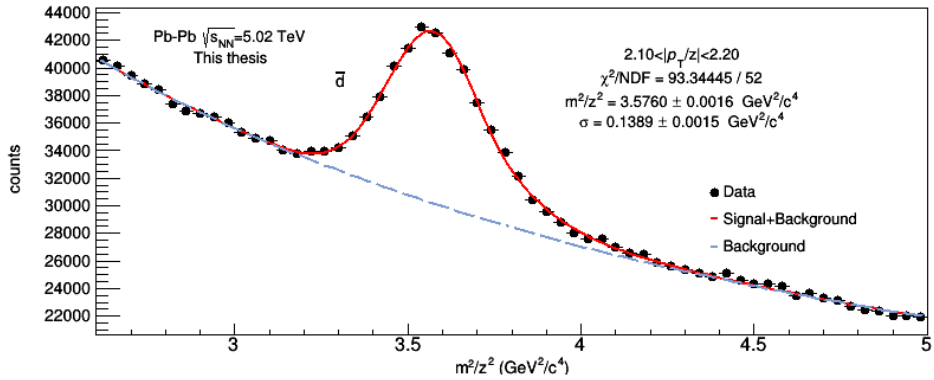
Pb-Pb $\sqrt{s_{NN}}$=5.02 TeV
This thesis
$\bar{d}$
2.10<|p_T/z|<2.20
χ^2/NDF = 93.34445 / 52
m^2/z^2 = 3.5760 ± 0.0016 GeV^2/c^4
σ = 0.1389 ± 0.0015 GeV^2/c^4
Data
Signal+Background
Background
counts
m^2/z^2 (GeV^2/c^4)

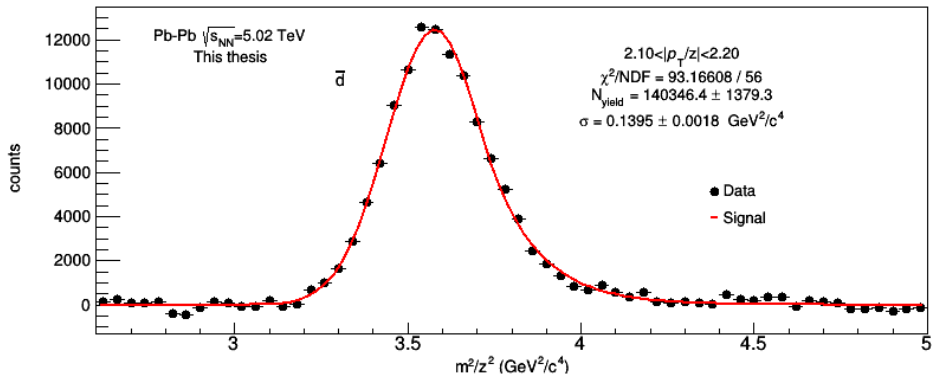
Pb-Pb $\sqrt{s_{NN}}$=5.02 TeV
This thesis
$\bar{d}$
2.10<|p_T/z|<2.20
χ^2/NDF = 93.16608 / 56
N_{yield} = 140346.4 ± 1379.3
σ = 0.1395 ± 0.0018 GeV^2/c^4
Data
Signal
counts
m^2/z^2 (GeV^2/c^4)

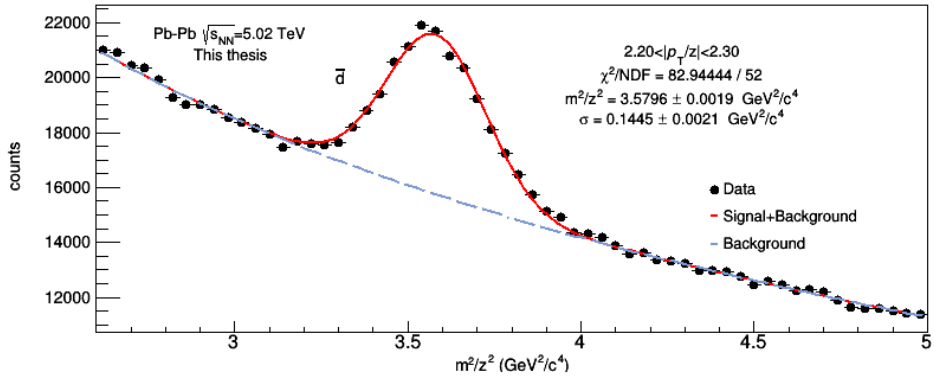
Pb-Pb $\sqrt{s_{NN}}$=5.02 TeV
This thesis
$\bar{d}$
2.20<|p_T/z|<2.30
χ^2/NDF = 82.94444 / 52
m^2/z^2 = 3.5796 ± 0.0019 GeV^2/c^4
σ = 0.1445 ± 0.0021 GeV^2/c^4
Data
Signal+Background
Background
counts
m^2/z^2 (GeV^2/c^4)

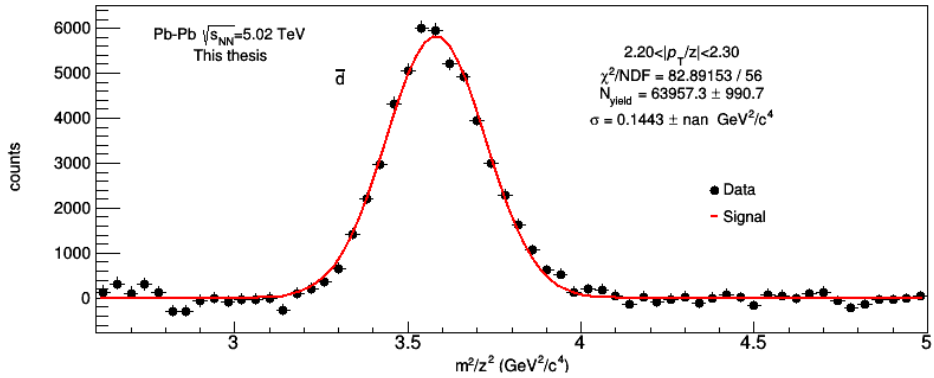
Pb-Pb $\sqrt{s_{NN}}$=5.02 TeV
This thesis
$\bar{d}$
2.20<|p_T/z|<2.30
χ^2/NDF = 82.89153 / 56
N_{yield} = 63957.3 ± 990.7
σ = 0.1443 ± nan GeV^2/c^4
Data
Signal
counts
m^2/z^2 (GeV^2/c^4)

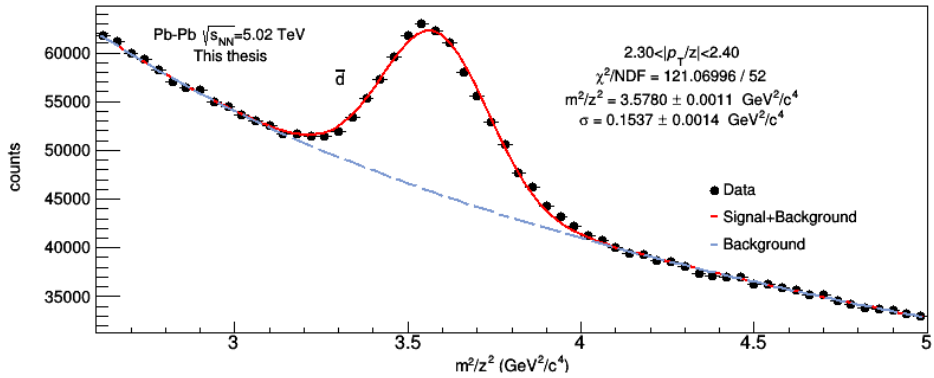
Pb-Pb $\sqrt{s_{NN}}$=5.02 TeV
This thesis
$\bar{d}$
2.30<|p_T/z|<2.40
χ^2/NDF = 121.06996 / 52
m^2/z^2 = 3.5780 ± 0.0011 GeV^2/c^4
σ = 0.1537 ± 0.0014 GeV^2/c^4
Data
Signal+Background
Background
counts
m^2/z^2 (GeV^2/c^4)

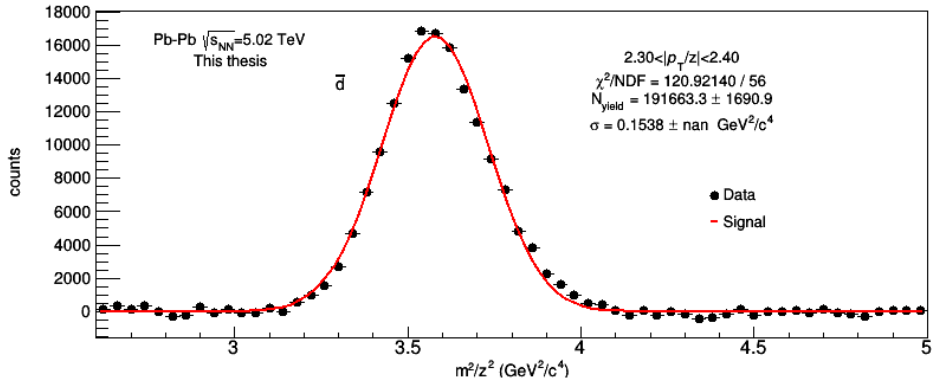
Pb-Pb $\sqrt{s_{NN}}$=5.02 TeV
This thesis
$\bar{d}$
2.30<|p_T/z|<2.40
χ^2/NDF = 120.92140 / 56
N_{yield} = 191663.3 ± 1690.9
σ = 0.1538 ± nan GeV^2/c^4
Data
Signal
counts
m^2/z^2 (GeV^2/c^4)

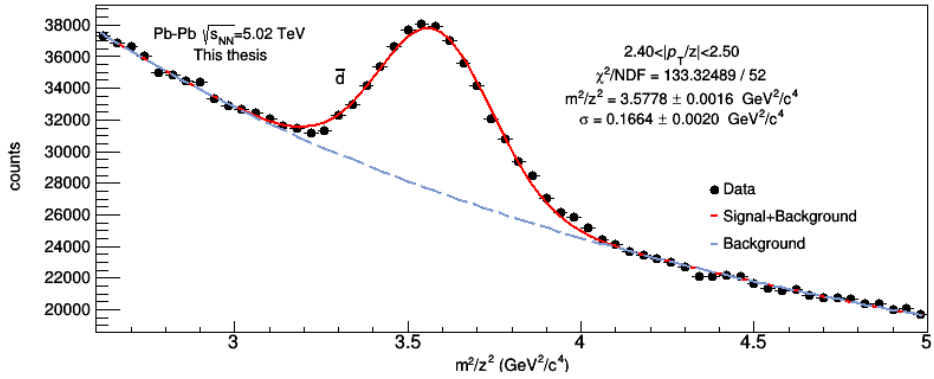
Pb-Pb $\sqrt{s_{NN}}$=5.02 TeV
This thesis
$\bar{d}$
2.40<|p_T/z|<2.50
χ^2/NDF = 133.32489 / 52
m^2/z^2 = 3.5778 ± 0.0016 GeV^2/c^4
σ = 0.1664 ± 0.0020 GeV^2/c^4
Data
Signal+Background
Background
counts
m^2/z^2 (GeV^2/c^4)

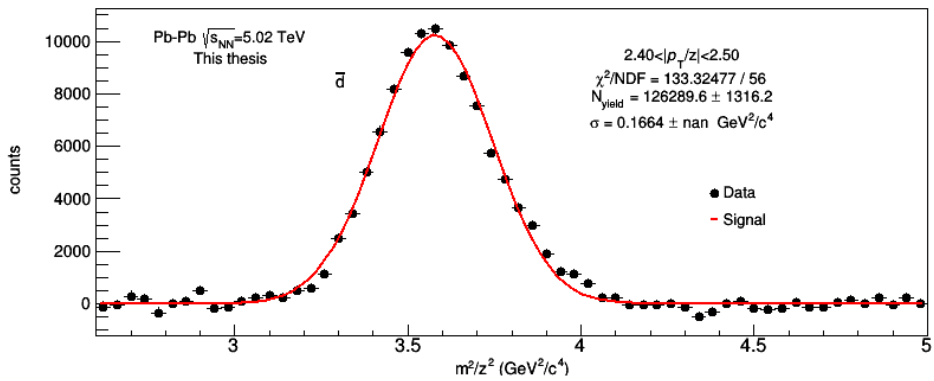
Pb-Pb $\sqrt{s_{NN}}$=5.02 TeV
This thesis
$\bar{d}$
2.40<|p_T/z|<2.50
χ^2/NDF = 133.32477 / 56
N_{yield} = 126289.6 ± 1316.2
σ = 0.1664 ± nan GeV^2/c^4
Data
Signal
counts
m^2/z^2 (GeV^2/c^4)

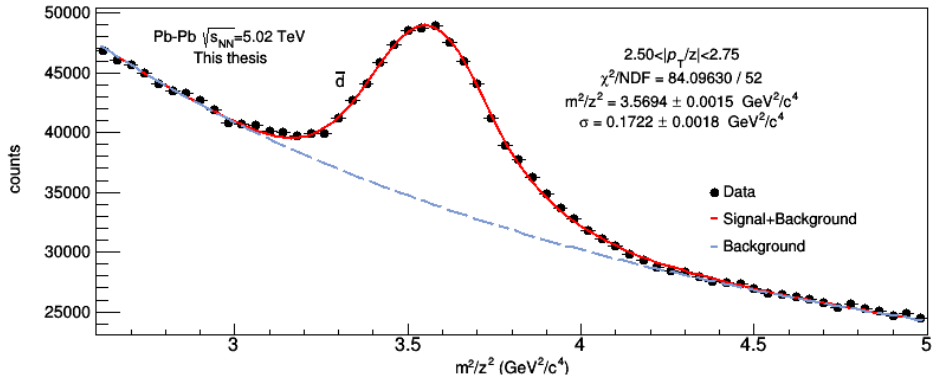
Pb-Pb $\sqrt{s_{NN}}$=5.02 TeV
This thesis
d
2.50<|p_T/z|<2.75
χ^2/NDF = 84.09630 / 52
m^2/z^2 = 3.5694 ± 0.0015 GeV^2/c^4
σ = 0.1722 ± 0.0018 GeV^2/c^4
Data
Signal+Background
Background
counts
m^2/z^2 (GeV^2/c^4)

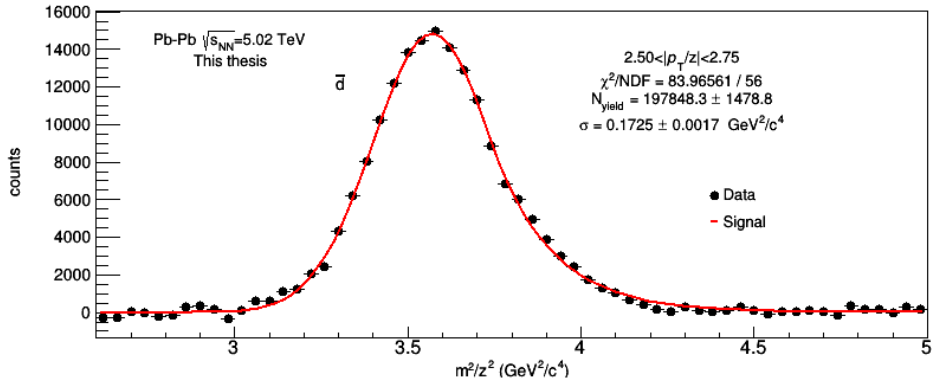
Pb-Pb $\sqrt{s_{NN}}$=5.02 TeV
This thesis
d
2.50<|p_T/z|<2.75
χ^2/NDF = 83.96561 / 56
N_{yield} = 197848.3 ± 1478.8
σ = 0.1725 ± 0.0017 GeV^2/c^4
Data
Signal
counts
m^2/z^2 (GeV^2/c^4)

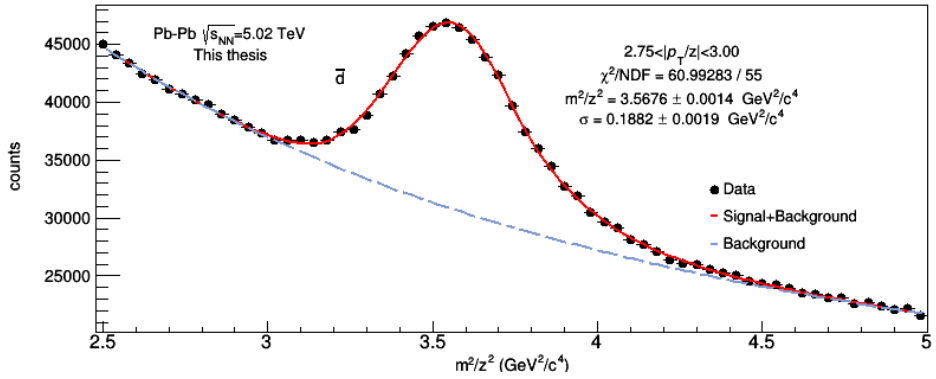
Pb-Pb $\sqrt{s_{NN}}$=5.02 TeV
This thesis
d
2.75<|p_T/z|<3.00
χ^2/NDF = 60.99283 / 55
m^2/z^2 = 3.5676 ± 0.0014 GeV^2/c^4
σ = 0.1882 ± 0.0019 GeV^2/c^4
Data
Signal+Background
Background
counts
m^2/z^2 (GeV^2/c^4)

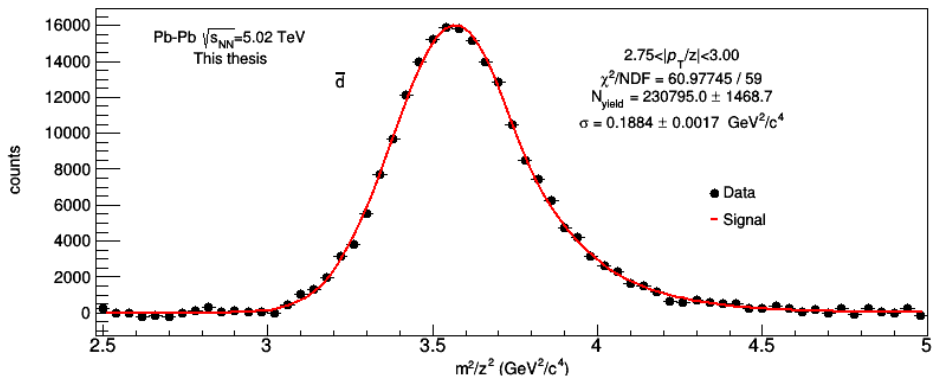
Pb-Pb $\sqrt{s_{NN}}$=5.02 TeV
This thesis
d
2.75<|p_T/z|<3.00
χ^2/NDF = 60.97745 / 59
N_{yield} = 230795.0 ± 1468.7
σ = 0.1884 ± 0.0017 GeV^2/c^4
Data
Signal
counts
m^2/z^2 (GeV^2/c^4)

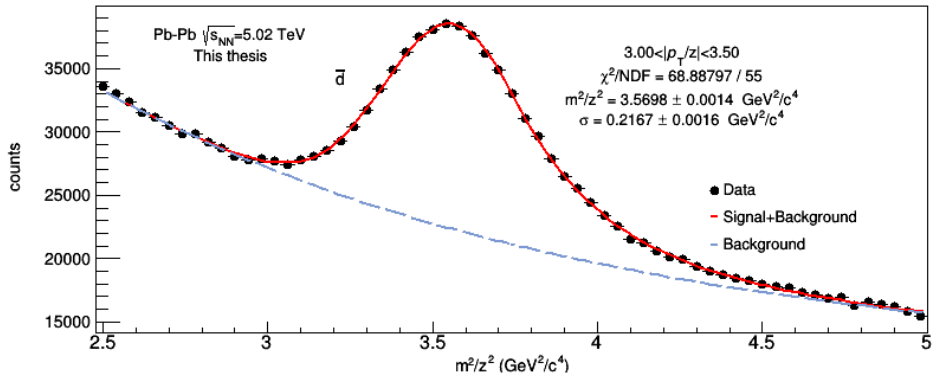
Pb-Pb $\sqrt{s_{NN}}$=5.02 TeV
This thesis
$\bar{d}$
3.00<|p_T/z|<3.50
χ^2/NDF = 68.88797 / 55
m^2/z^2 = 3.5698 ± 0.0014 GeV^2/c^4
σ = 0.2167 ± 0.0016 GeV^2/c^4
Data
Signal+Background
Background
counts
m^2/z^2 (GeV^2/c^4)

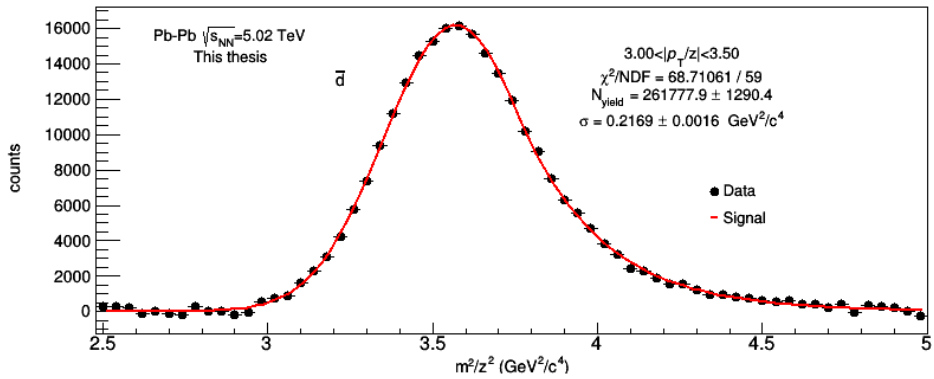
Pb-Pb $\sqrt{s_{NN}}$=5.02 TeV
This thesis
$\bar{d}$
3.00<|p_T/z|<3.50
χ^2/NDF = 68.71061 / 59
N_{yield} = 261777.9 ± 1290.4
σ = 0.2169 ± 0.0016 GeV^2/c^4
Data
Signal
counts
m^2/z^2 (GeV^2/c^4)

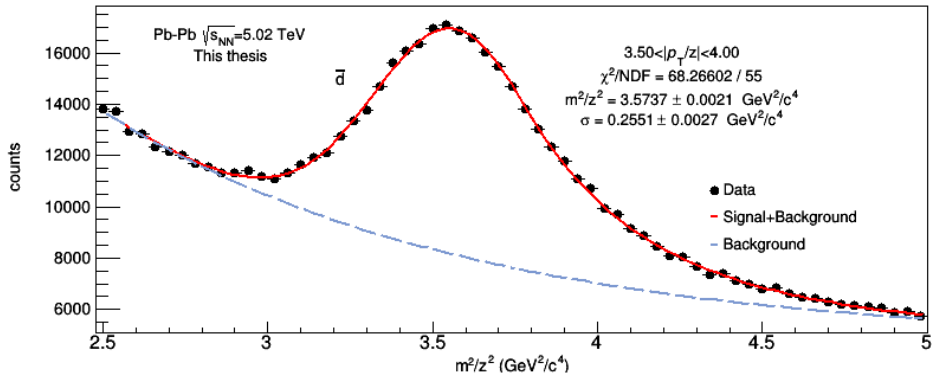
Pb-Pb $\sqrt{s_{NN}}$=5.02 TeV
This thesis
$\bar{d}$
3.50<|p_T/z|<4.00
χ^2/NDF = 68.26602 / 55
m^2/z^2 = 3.5737 ± 0.0021 GeV^2/c^4
σ = 0.2551 ± 0.0027 GeV^2/c^4
Data
Signal+Background
Background
counts
m^2/z^2 (GeV^2/c^4)

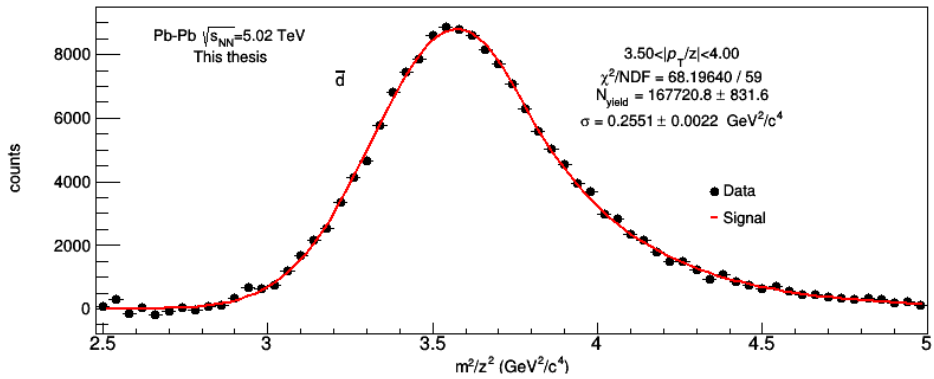
Pb-Pb $\sqrt{s_{NN}}$=5.02 TeV
This thesis
$\bar{d}$
3.50<|p_T/z|<4.00
χ^2/NDF = 68.19640 / 59
N_{yield} = 167720.8 ± 831.6
σ = 0.2551 ± 0.0022 GeV^2/c^4
Data
Signal
counts
m^2/z^2 (GeV^2/c^4)

Appendix B

(Anti-)Helium-3 plots

This section contains all the fits used for the extraction of the squared mass-to-charge ratio and the yields of the ^{3}He and $^3\overline{\text{He}}$. This has been done in a transverse momentum range $p_T = [1\,\text{GeV}, 3\,\text{GeV}]$ in steps of 500 MeV and $p_T = [3\,\text{GeV}, 4\,\text{GeV}]$.

B.1 Helium-3 fits

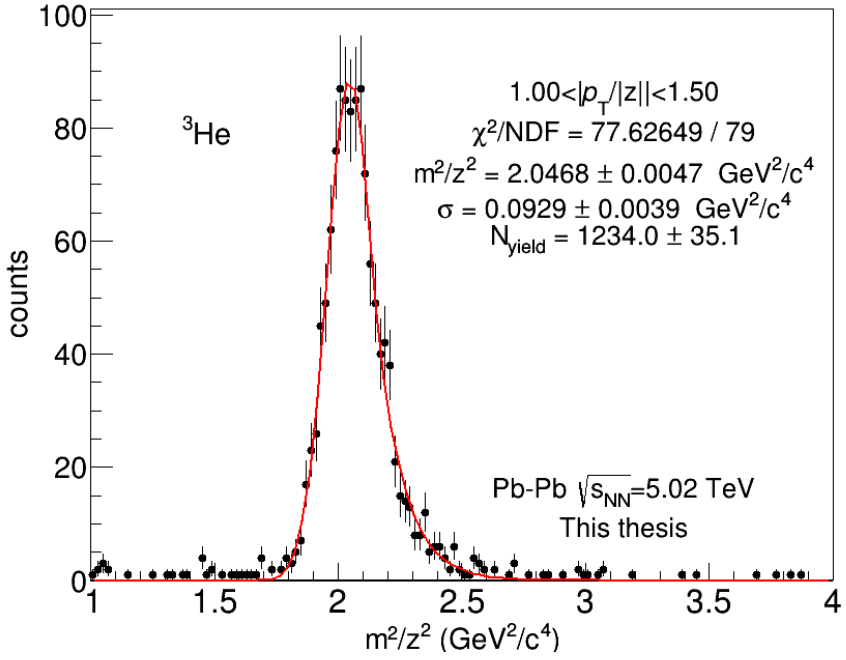

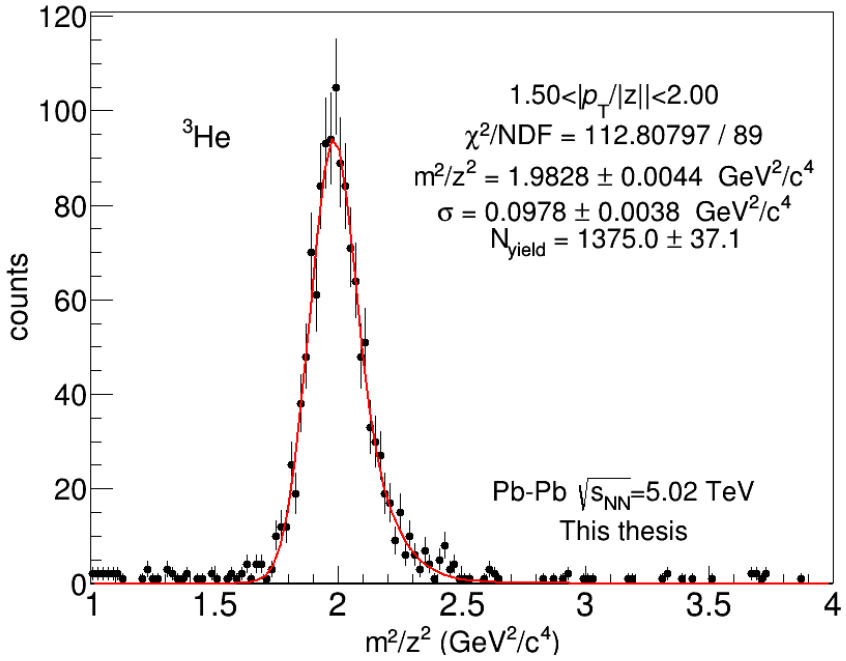
1.50<|p_T/|z||<2.00
χ²/NDF = 112.80797 / 89
m²/z² = 1.9828 ± 0.0044 GeV²/c⁴
σ = 0.0978 ± 0.0038 GeV²/c⁴
N_yield = 1375.0 ± 37.1
³He
Pb-Pb √s_NN=5.02 TeV
This thesis
counts
m²/z² (GeV²/c⁴)

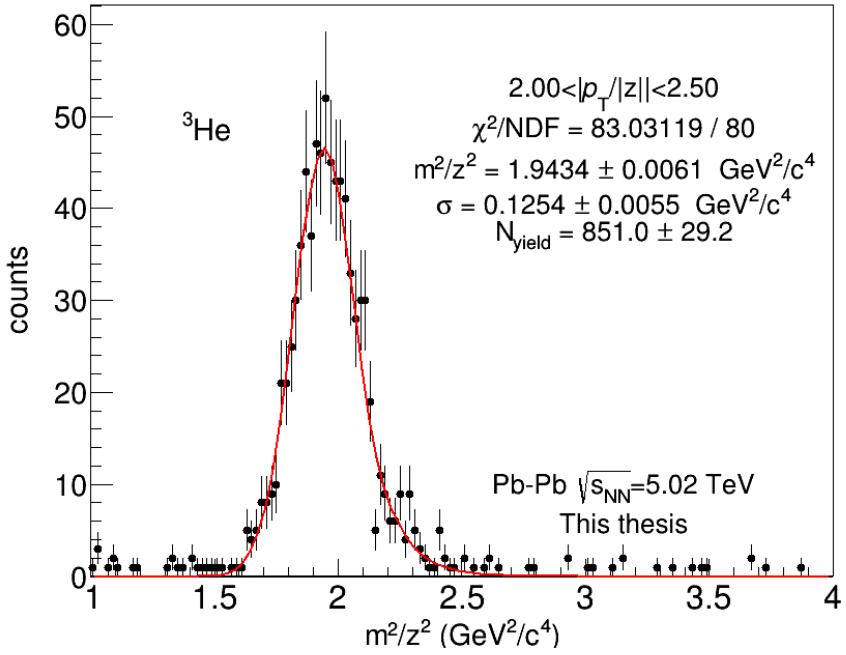
2.00<|p_T/|z||<2.50
χ²/NDF = 83.03119 / 80
m²/z² = 1.9434 ± 0.0061 GeV²/c⁴
σ = 0.1254 ± 0.0055 GeV²/c⁴
N_yield = 851.0 ± 29.2
³He
Pb-Pb √s_NN=5.02 TeV
This thesis
counts
m²/z² (GeV²/c⁴)

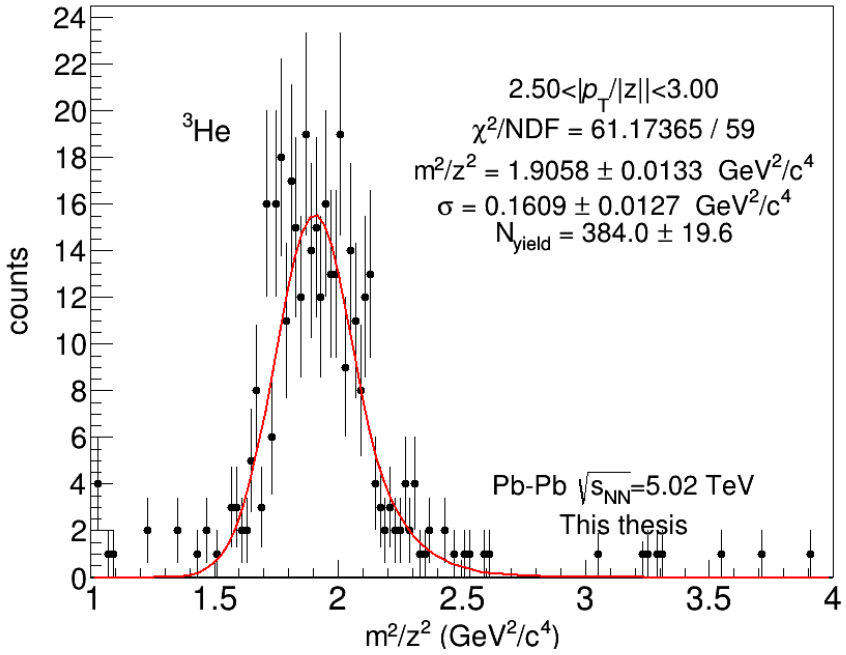

B.2 Anti-Helium-3 fits

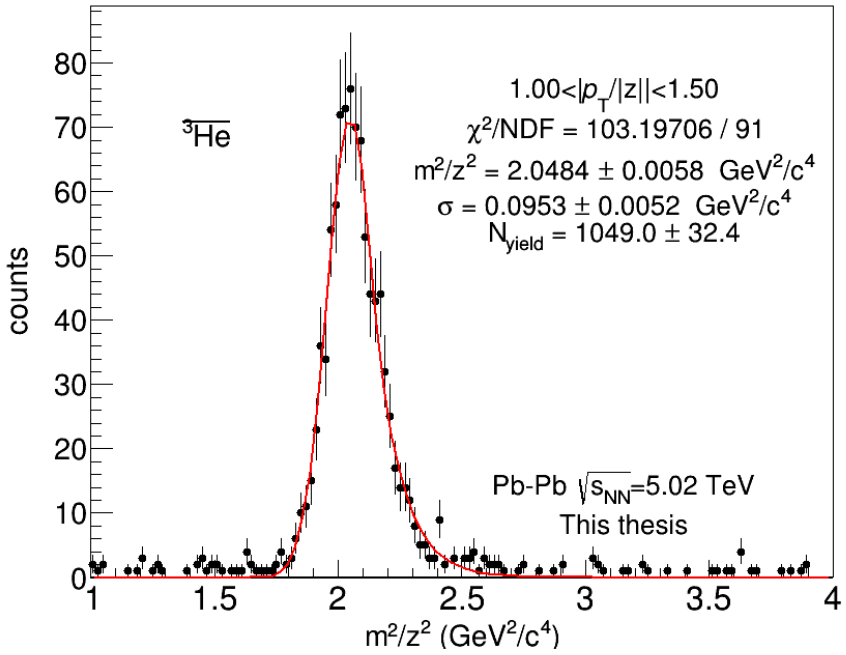

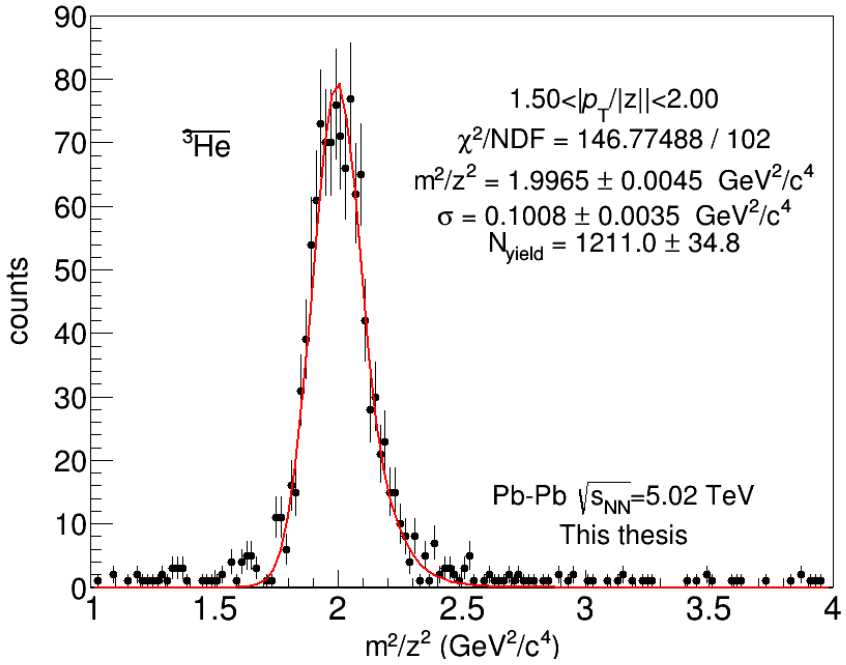
$^3\overline{\text{He}}$
1.50<|p_T/|z||<2.00
χ^2/NDF = 146.77488 / 102
m^2/z^2 = 1.9965 ± 0.0045 GeV^2/c^4
σ = 0.1008 ± 0.0035 GeV^2/c^4
N_{yield} = 1211.0 ± 34.8
Pb-Pb $\sqrt{s_{NN}}$=5.02 TeV
This thesis
counts
m^2/z^2 (GeV^2/c^4)

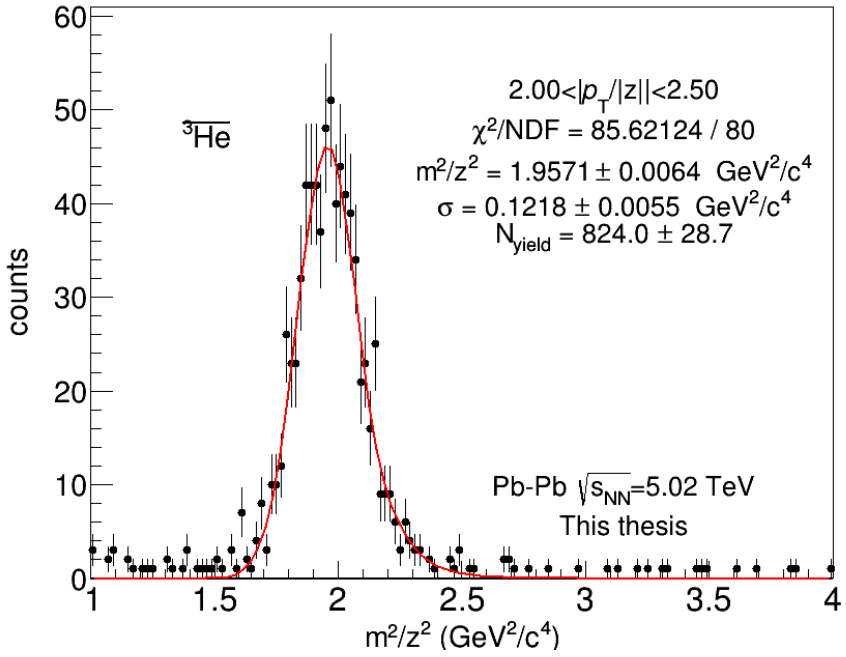
$^3\overline{\text{He}}$
2.00<|p_T/|z||<2.50
χ^2/NDF = 85.62124 / 80
m^2/z^2 = 1.9571 ± 0.0064 GeV^2/c^4
σ = 0.1218 ± 0.0055 GeV^2/c^4
N_{yield} = 824.0 ± 28.7
Pb-Pb $\sqrt{s_{NN}}$=5.02 TeV
This thesis
counts
m^2/z^2 (GeV^2/c^4)

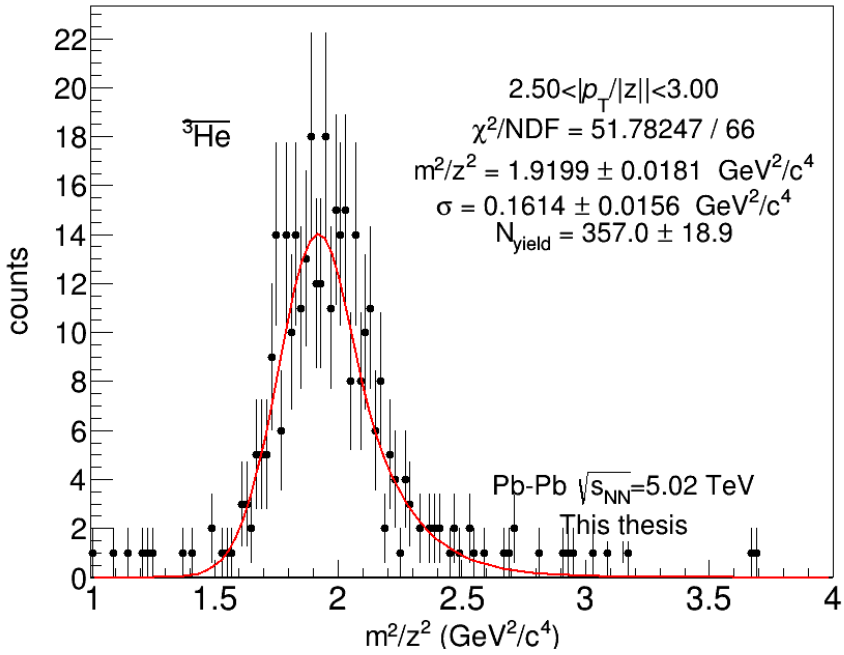
counts
m^2/z^2 (GeV^2/c^4)
$^3\overline{He}$
2.50<|p_T/|z||<3.00
χ^2/NDF = 51.78247 / 66
m^2/z^2 = 1.9199 ± 0.0181 GeV^2/c^4
σ = 0.1614 ± 0.0156 GeV^2/c^4
N_{yield} = 357.0 ± 18.9
Pb-Pb $\sqrt{s_{NN}}$=5.02 TeV
This thesis